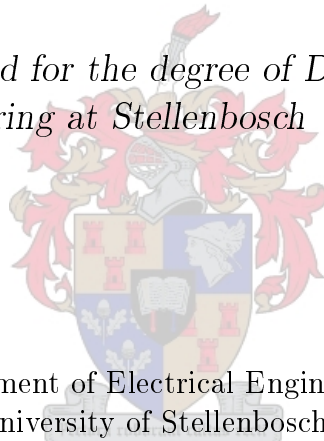


Direct Current Conductor Corona Modelling and Metrology

by

Abraham Johannes Otto

*Dissertation presented for the degree of Doctor of Philosophy
in Engineering at Stellenbosch University*



Department of Electrical Engineering
University of Stellenbosch
Private Bag X1, 7602 Matieland, South Africa

Promoter: Prof H.C. Reader
Chair of High Frequency Electronics
E&E Engineering
University of Stellenbosch

September 2009

Declaration

By submitting this dissertation electronically, I declare that the entirety of the work contained therein is my own, original work, that I am the owner of the copyright thereof (unless to the extent explicitly otherwise stated) and that I have not previously in its entirety or in part submitted it for obtaining any qualification.



Signature:

A.J. Otto

Date:

31-08-2009

.....

Copyright © 2009 Stellenbosch University
All rights reserved.

Acknowledgements

I would like to acknowledge the following people without whom this dissertation would not have been possible:

My Delita, for all her love, support and patience.

My mother, father and brother for their continuous love and support.

My study leader, Prof. Howard Reader, for his guidance throughout the research. I would like to thank him for inspiring me, whilst he was presenting an EMC course in 2006, to pursue a doctoral degree. I have never met someone so passionate and enthusiastic about his work. It was a great honour and privilege for me to interact with him at this level.

Evan Lezar for all his help with the computational aspects. I would like to thank him for enduring endless questions and long hours of technical discussion, but most of all for his friendship. It means a great deal to me.

Prof. David Davidson for his willingness to help with the understanding of the numerical code, algorithms and analytical solutions.

Riaan Roets from Kierpersol Technologies for all his efforts in assisting me with the measurements over the past 3 years. His readiness to go the extra mile for people is what makes him such a great person. I would like to thank him for allowing me to share in his years of corona measurement experience. I would also like to thank Coenie Esterhuizen and Jaco Badenhorst who assisted with the measurements. It really was a pleasure to work with this team.

From Eskom: Prof. Tony Britten for his guidance. I wish thank him for often taking time out of his busy schedule for an interesting and always useful technical discussion. I would further like to thank Roy Hubbard for allowing us to borrow his impulse generator and assisting us with measurements.

Petrus Pieterse for all his efforts in the high voltage laboratory at the University of Stellenbosch. I appreciate the help with the measurements, the interesting discussions and the conference papers. I would also like to acknowledge Wessel Kroukamp from the SED workshop at the university.

Dr. Rodney Urban for getting me started in my PhD corona work at the University of Stellenbosch. For allowing me to use his small corona cage and initial sampling card.

Paul van der Merwe for his friendship and support over the past few years, and hopefully many years to come.

Last, but definitely not least, my fellow postgraduate students in Room E212. Thank you for creating such a great working environment. All the best for your future endeavours.

This research study was funded by ESKOM.

Contents

Declaration	i
Acknowledgements	ii
Contents	iv
List of Figures	ix
List of Tables	xix
Nomenclature	xx
Abstract	1
Opsomming	3
1 Introduction	5
1.1 Operational Experience	5
1.2 Eskom's Need for HVDC Research	6
1.3 Research Objectives	8
1.4 Claims Made by This Dissertation	9
1.5 Dissertation Layout	11
2 Direct Current Corona and Gap Discharges	13
2.1 Corona Discharges	13
2.1.1 Corona Inception	13
2.2 Air as insulating medium	15
2.2.1 Classical Atomic Theory	16
2.3 The Gas Discharge Processes	17

2.3.1	Ionization	17
2.3.2	Excitation	18
2.3.3	Secondary Ionization	18
2.3.4	Attachment and Detachment	19
2.3.5	Recombination	19
2.4	Gas Discharge Coefficients	20
2.4.1	Ionization Coefficient (α)	20
2.4.2	Attachment Coefficient (η)	21
2.4.3	Photoionization Coefficient (γ)	23
2.4.4	Electron Drift Velocity	24
2.4.5	Electron Diffusion	25
2.4.6	Ion Diffusion	25
2.4.7	Ion Mobility	26
2.5	High Voltage Direct Current Conductor Corona	27
2.5.1	Corona Current: Time Domain	27
2.5.2	Corona Current: Frequency Domain	28
2.5.3	Positive DC Corona Modes	30
2.5.4	Negative DC Corona Modes	33
2.6	Corona Generated Space Charge	36
2.6.1	Space Charge Effect on Electric Field	36
2.6.2	Currents due to Space Charge Effect	37
2.7	Environmental Effects on DC Corona	38
2.7.1	Particle Deposition	38
2.7.2	Weather Conditions	38
2.7.3	Altitude, Air Pressure and Humidity	39
3	Particle-In-Cell Simulation	40
3.1	Introduction	40
3.2	Continuity Equations and Momentum Conservation	41
3.2.1	Fluid Continuity Equation	41
3.2.2	Fluid Momentum Conservation	43
3.3	PIC Simulation Model	44
3.4	Field Equations	45
3.5	Conduction and Displacement Current	46
3.6	Charge Simulation Method	47

3.7	Domain Discretization (Meshing)	49
3.8	Finite Element Method	49
3.8.1	First Order Elements	51
3.8.2	First Order Weighting	53
3.8.3	Higher Order Elements	54
3.9	Time Integration: Linear Multistep Method	55
3.10	Mathematical Model	56
3.10.1	Positive Streamer Development	56
3.10.2	Negative Streamer Development	58
3.10.3	PIC Streamer Development Flowchart	60
4	Space Charge Particle Dynamics	61
4.1	Numerical Code Validation	61
4.1.1	Parallel Plate Electrode Solution	61
4.1.2	Cylindrical Electrode Solution	64
4.1.3	Space Charge Free Solution	65
4.1.4	Space Charge Solution	65
4.1.5	Flow Vector and Time Integration Solution	70
4.2	Ion Space Charge Travel-Time Predictions	72
4.3	Avalanches and Space Charge Dynamics	74
4.3.1	Anode Corona Streamers	74
4.3.2	Cathode Corona Streamers	76
4.4	Altitude Effects	77
4.5	Electrometer-type Circuit	80
4.5.1	Circuit Design	80
4.5.2	Sensing Plate Design	81
4.5.3	Operating Principle	81
4.5.4	Calibration	83
4.6	Space Charge Measurements	85
4.6.1	Experimental Arrangement	85
4.6.2	Test Circuit	86
4.6.3	UV Intensifying Corona Camera	86
4.6.4	Wire-Plane Numerical Solution	86
4.6.5	Measurement Results	88
4.6.6	PIC Computational Results	89

4.6.7	Space Charge Timing Interpretation	92
5	DC Conductor Corona Measurement Methods	93
5.1	Corona Test Methods	94
5.1.1	Small Corona Cage	94
5.1.2	Short Test Line	96
5.1.3	Large Corona Cage	97
5.2	Background Radio Noise Characterisation	99
5.2.1	Small Corona Cage RN Coupling	99
5.2.2	Large Corona Cage RN Coupling	100
5.2.3	Short Test Line RN Coupling	101
5.3	Conducted Radio Noise Measurement Circuits	102
5.3.1	Wideband Measurement Circuit	102
5.3.2	CISPR Narrowband Measurement Circuit	103
5.4	Radio Noise Meters	106
5.5	Importance of Impedance Matching in Wideband Corona Measurements	108
5.5.1	Termination Into Characteristic Impedance	110
5.5.2	Time Domain Parameter Definitions	111
5.5.3	Unmatched System Time Domain Measurements	111
5.5.4	Matched System Time Domain Measurements	113
5.5.5	Frequency Domain Measurements	114
6	RI Performance Evaluation and Excitation Functions	117
6.1	RI Measurements Using Three Corona Test Methods	118
6.1.1	Measurement Program	118
6.1.2	Frequency Domain Measurements	119
6.1.3	Conductor Corona Test Method Comparison	122
6.1.4	Time Domain Parameter Extraction	124
6.1.5	Wideband Excitation	130
6.2	Excitation Function Theory	132
6.2.1	Demonstration by Means of the Potential Function	132
6.2.2	Excitation Function: Corona Cages	134
6.2.3	Excitation Function: Test Line	135
6.3	RI Excitation Functions and Empirical Predictions	136
6.3.1	Radiated Radio Interference	137

6.3.2	Conducted Radio Interference	137
6.4	Excitation Function Results	139
6.4.1	Possible Altitude Correction	140
7	Conclusions and Recommendations for Future Work	142
	Bibliography	146
A	Computational Mathematics	156
A.1	Partial Differentiation of Matrices and Vectors	156
A.2	Simplex Coordinate Formulas	156
B	UV Intensifying Corona Camera	158
B.1	Electrometer Measurements	158
B.2	Corona Cage Measurements	159
C	Direct Current Voltage Source	160
D	Charge Motion Between Cylindrical Electrodes	163
D.1	Analytical Solution - Anode Corona	163
D.1.1	Specific Example - Anode Corona	169
D.2	Analytical Solution - Cathode Corona	173
E	Altitude Effects on RI Measurements	178
E.1	Altitude Measurements: Zebra Conductor	179
E.2	Altitude Measurements: Kingbird Conductor	180
E.2.1	Paarl: 156m	182
E.2.2	Laingsburg: 580m	184
E.2.3	Beaufort West: 951m	185
E.2.4	De Aar: 1240m	186
E.2.5	Midrand: 1550m	187
E.2.6	Clarens: 1900m	188
E.2.7	Up and Down Readings: Kingbird	189

List of Figures

1.1	Cahora Bassa HVDC scheme with quad Zambezi pole conductor and Oden insulated shieldwire [3] (Map taken from [1])	6
1.2	South African Power Pool (SAPP) countries involved in the Westcor power project [3]	7
1.3	Flowchart for dissertation layout	12
2.1	Bohr model of the Hydrogen atom with “permitted” orbits of an electron [18]	16
2.2	Ionization data in air for electric field per pressure values of $25 \leq E/p \leq 60 \frac{V}{cm \cdot torr}$.	21
2.3	Ionization data in air for electric field per pressure values of $60 < E/p \leq 240 \frac{V}{cm \cdot torr}$	21
2.4	Attachment data in air for electric field per pressure values of $25 \leq E/p \leq 60 \frac{V}{cm \cdot torr}$	23
2.5	Photoionization data in air for $0 \leq pd \leq 600 \text{ cm} \cdot \text{torr}$	24
2.6	Electron drift velocity in air as a function of $E/p [\frac{V}{cm \cdot torr}]$	25
2.7	Electron diffusion in air as a function of $E/p [\frac{V}{cm \cdot torr}]$	26
2.8	Typical positive and negative corona pulses	28
2.9	Frequency domain data for typical positive and negative corona pulses	30
2.10	Anode avalanche generation leaving behind positive ions	31
2.11	Enhancement of E-field in electrode gap due to positive ions	31
2.12	Electron avalanche at the cathode	34
2.13	Negative ion space charge after electron avalanche	34
2.14	A schematic view of the space charge of a typical HVDC bipolar line [42]	36
3.1	Conductor above ground plane and conductor in cylinder for CSM solution	47
3.2	The assignment factor for charge and contour placement in convex and concave curvature	48
3.3	Discretization of domain Ω into smaller elements Ω^e where $e = 1, 2$	49
3.4	Meshing of conductor in centre of cage	50
3.5	Meshing of conductor offset in cage	50
3.6	Linear three node triangular finite element e	51

3.7	Quadratic six node triangular finite element e	54
3.8	Spatial-temporal developments of successive avalanche generations forming the corona pulse [39]	58
3.9	PIC streamer development flowchart	60
4.1	(a) First order domain discretization (b) Second order domain discretization	62
4.2	(a) 2D Electrostatic potential solution (b) 3D Electrostatic potential solution	62
4.3	The parallel plate electrostatic E-field vector solution	63
4.4	The parallel plate space charge potential solution	63
4.5	The parallel plate space charge E-field vector solution	64
4.6	(a) 2D PIC meshing and (b) 3D CST cylindrical geometry	65
4.7	Electrostatic E-field in $[V/m]$	66
4.8	Space charge E-field in $[V/m]$	66
4.9	Location of simulation particles next to highly stressed conductor at time $t = 0$	67
4.10	PIC (FEM) potential at time $t = 0$: Range 0 to 62V	67
4.11	PIC (FEM) electric flux density at time $t = 0$: Range 1×10^{-8} to $10 \times 10^{-8} C/m^2$	67
4.12	PIC (FEM) space charge density at time $t = 0$: Range 2.5×10^{-6} to $22.5 \times 10^{-6} C/m^3$	67
4.13	CST space charge potential at time $t = 0$: Range 0 to 58.4V	68
4.14	CST space charge electric flux density at time $t = 0$: Range 1.6×10^{-8} to $12.9 \times 10^{-8} C/m^2$	68
4.15	Quadratic and linear triangular elements used in the finite element method	69
4.16	Specific example for charge motion in cylindrical configuration	70
4.17	Electrostatic potential distribution calculated with the CSM	71
4.18	Electron movement calculated analytically and with PIC numerical code	71
4.19	Time for negative ion movement from r_c to r_i calculated analytically and with PIC numerical code	72
4.20	Total time for electron movement from r_c to r_i and negative ion movement from r_i to r_b	72
4.21	Test line and corona cage arrangements for ion space charge travel times	73
4.22	Ion space charge travels times for single corona events in various test methods	73
4.23	(a) Ionization region of $r_i = 2.44cm$ around anode conductor $r = 1.41cm$ (b) Electric field at ground level due to anode conductor-plane configuration	74
4.24	(a) The number of electrons created by electron avalanche (b) Head radius of electron avalanche	75
4.25	Current on conductor due to electron avalanche	75

4.26	Number of electrons created by electron avalanche	76
4.27	Head radius of electron avalanche as a function of lifetime	76
4.28	Cathode corona current pulse computed with Particle-In-Cell code	77
4.29	Cathode corona space charge spatial development 1ns to 30ns	78
4.30	Cathode corona space charge spatial development 1us to 5ms	79
4.31	PIC computation of ionization region around Zebra conductor for various altitudes and temperatures	80
4.32	PIC computation of ionization region around Kingbird conductor for various altitudes and temperatures	80
4.33	Electrometer circuit design schematic	81
4.34	Schematic view of Wilson plate mounted flush with ground plane [42]	82
4.35	Sensing electrode design placed flush with aluminium ground plane	82
4.36	Measured voltage on electrometer sensing plate for given applied voltage and frequency	84
4.37	Measured and predicted charge values on electrometer sensing plate for given applied voltage and frequency	84
4.38	Experimental arrangement for conductor above ground plane	85
4.39	Artificial corona source used in experimental arrangement	86
4.40	A set of onset streamer discharges captured with a UV intensifying corona camera for a conductor height $h = 64.5cm$ (vertical scale in $1cm$ increments)	87
4.41	Analytical solution to the scalar potential for a wire-plane geometry	88
4.42	Analytical solution to the vector electric field for a wire-plane geometry	88
4.43	Corona pulse (top image) and electrometer output (bottom image)	89
4.44	Electrometer output for anode and cathode corona at similar voltage and height	90
4.45	Measured and PIC simulated electrometer output	91
4.46	Measured and PIC simulated example for cathode corona space charge timings	91
5.1	Corona discharges on a twin conductor bundle in the Eskom Megawatt Park large outdoor corona cage [Photo by: <i>C. Esterhuizen</i>]	94
5.2	Schematic for Eskom Megawatt Park small corona cage measurement system	95
5.3	Eskom Megawatt Park small corona cage	95
5.4	Schematic for Eskom Megawatt Park short test line measurement system	96
5.5	Eskom Megawatt Park short test line	97
5.6	Schematic for Eskom Megawatt Park large outdoor corona cage measurement system	98
5.7	Eskom Megawatt Park large outdoor corona cage	98
5.8	EMCO current probe around small corona cage main earth	99

5.9	Radio noise levels measured on small corona cage main earth	100
5.10	Radio noise levels measured on small corona cage inner earth	100
5.11	Radio noise levels in the spectrum 0 to 30MHz measured on large corona cage main earth	101
5.12	Radio noise levels in the spectrum 0 to 30MHz measured on large corona cage inner earth	101
5.13	Time domain reflectometry measurements on large corona cage	101
5.14	Radio noise levels in the spectrum 0 to 30MHz measured on short test line main earth	102
5.15	Schematics for wideband measurement circuits connected to systems with characteristic impedance Z_0	103
5.16	Transfer function for coupling capacitor used in small corona cage measurement circuit	104
5.17	Transfer function for wideband measurement circuit used in small corona cage measurements	104
5.18	Transfer function for coupling capacitor used in large corona cage and test line measurement circuits	104
5.19	Transfer function for wideband measurement circuit used in large corona cage and test line measurements	104
5.20	Schematics for CISPR narrowband measurement circuits as applied by Eskom for RI measurements over 300Ω	105
5.21	Transfer function for the CISPR standard measurement circuit used on the small corona cage	106
5.22	Transfer function for the CISPR standard measurement circuit used on the large corona cage at Megawatt Park	106
5.23	Block diagrams for a typical radio noise meter [9]	106
5.24	Schematic of a radio noise meter with quasi-peak detector [88]	107
5.25	The indicated level versus the modulated waveforms for various detectors (P=Peak; QP=Quasi-Peak; A=Average) [89]	107
5.26	Small laboratory corona cage at the University of Stellenbosch	109
5.27	Various positive voltages applied to single artificial source on smooth aluminium conductor in small corona cage	109
5.28	Various positive voltages applied to three artificial sources on smooth aluminium conductor in small corona cage	109
5.29	Schematic of small laboratory corona cage with characteristic impedance matching circuit	110

5.30	Positive corona current pulse with rise time, fall time and pulse duration definition	112
5.31	Typical distorted positive corona current pulse measured with unmatched system and single artificial corona sources	112
5.32	Typical distorted positive corona current pulse measured with unmatched system and multiple artificial corona sources	112
5.33	Time domain data for typical positive corona current pulse captured on matched system	113
5.34	Frequency domain data for typical positive corona current pulse captured on matched system	113
5.35	Amplitude variation between single source measurements in matched and unmatched systems and empirical values	114
5.36	Amplitude variation between multiple source measurements in matched and unmatched systems and empirical values	114
5.37	Quasi-peak measurements of single artificial corona source at various surface voltage gradients for matched and unmatched systems	115
5.38	Quasi-peak measurements of multiple artificial corona sources at various surface voltage gradients for matched and unmatched systems	115
5.39	Wideband RI levels on matched and unmatched large corona cage system	115
6.1	Dissertation measurement program	118
6.2	Peak, Quasi-Peak and RMS RI levels in $dB\mu V$ for a single Zebra conductor in a wideband small corona cage system	120
6.3	Peak, Quasi-Peak and RMS RI levels in $dB\mu V$ over 300Ω for a single Kingbird conductor in a narrowband small corona cage system	120
6.4	Average wideband and CISPR narrowband measurements for Zebra conductor in small corona cage	120
6.5	Peak, Quasi-Peak and RMS RI levels in $dB\mu V$ for a single Zebra conductor in a wideband short test line system	121
6.6	Peak, Quasi-Peak and RMS RI levels in $dB\mu V$ over 300Ω for a single Kingbird conductor in a narrowband short test line system	121
6.7	Peak, Quasi-Peak and RMS RI levels in $dB\mu V$ for a single Zebra conductor in a wideband large corona cage system	122
6.8	Peak, Quasi-Peak and RMS RI levels in $dB\mu V$ over 300Ω for a single Kingbird conductor in a narrowband large corona cage system	122

6.9	Peak RI levels in $dB\mu V$ using the three corona measurement methods to evaluate Zebra conductor	123
6.10	Peak RI levels in $dB\mu V$ over 300Ω using the three corona measurement methods to evaluate Kingbird conductor	123
6.11	Quasi-Peak RI levels in $dB\mu V$ using the three corona measurement methods to evaluate Zebra conductor	123
6.12	Quasi-Peak RI levels in $dB\mu V$ over 300Ω using the three corona measurement methods to evaluate Kingbird conductor	123
6.13	RMS RI levels in $dB\mu V$ using the three corona measurement methods to evaluate Zebra conductor	124
6.14	RMS RI levels in $dB\mu V$ over 300Ω using the three corona measurement methods to evaluate Kingbird conductor	124
6.15	Time pulse trains recorded on large corona cage with surface voltage gradient $36kV/cm$	124
6.16	Time pulse trains recorded on short test line with surface voltage gradient $36kV/cm$	124
6.17	Time pulse trains recorded on small corona cage with surface voltage gradient $36kV/cm$	125
6.18	The average number of pulses per second measured in the time domain on the three systems evaluating the Zebra conductor (+DC)	126
6.19	The average number of pulses per second measured in the time domain on the three systems evaluating the Kingbird conductor (+DC)	126
6.20	The measured peak voltage in the time domain on the three systems evaluating the Zebra conductor (+DC)	126
6.21	The measured peak voltage in the time domain on the three systems evaluating the Kingbird conductor (+DC)	126
6.22	Statistical analysis of amplitude distribution for large corona cage with surface voltage gradient $E = 36.86kV/cm$	127
6.23	Statistical analysis of pulse repetition rate distribution for large corona cage with surface voltage gradient $E = 36.86kV/cm$	127
6.24	Statistical analysis of amplitude distribution for large corona cage with surface voltage gradient $E = 38.33kV/cm$	127
6.25	Statistical analysis of pulse repetition rate distribution for large corona cage with surface voltage gradient $E = 38.33kV/cm$	127
6.26	Statistical analysis of amplitude distribution for short test line with surface voltage gradient $E = 36.86kV/cm$	128

6.27	Statistical analysis of pulse repetition rate distribution for short test line with surface voltage gradient $E = 36.86kV/cm$	128
6.28	Statistical analysis of amplitude distribution for short test line with surface voltage gradient $E = 38.33kV/cm$	128
6.29	Statistical analysis of pulse repetition rate distribution for short test line with surface voltage gradient $E = 38.33kV/cm$	128
6.30	Statistical analysis of amplitude distribution for small corona cage with surface voltage gradient $E = 36.41kV/cm$	129
6.31	Statistical analysis of pulse repetition rate distribution for small corona cage with surface voltage gradient $E = 36.41kV/cm$	129
6.32	Statistical analysis of amplitude distribution for small corona cage with surface voltage gradient $E = 38.44kV/cm$	129
6.33	Statistical analysis of pulse repetition rate distribution for small corona cage with surface voltage gradient $E = 38.44kV/cm$	129
6.34	Lumped corona pulse train generator element and QP detector circuit	131
6.35	Wideband RI excitation compared to CISPR narrowband excitation	131
6.36	A coaxial element with space charge density q_0 at radius ρ	133
6.37	Zebra excitation functions of three corona test methods compared to empirical predictions	140
6.38	Kingbird excitation functions of three corona test methods compared to empirical predictions	140
6.39	Zebra excitation functions of three corona test methods compared to empirical predictions with altitude correction factor	141
6.40	Kingbird excitation functions of three corona test methods compared to empirical predictions with altitude correction factor	141
B.1	A set of onset streamer discharges captured with a UV intensifying corona camera for a conductor height $h = 70.5cm$ (vertical scale in $1cm$ increments)	158
B.2	A set of onset streamer discharges captured with a UV intensifying corona camera for a conductor height $h = 79.5cm$ (vertical scale in $1cm$ increments)	159
B.3	Positive burst corona on smooth aluminium conductor in small corona cage	159
C.1	BAUR PGK 260 HB voltage source [107]	160
C.2	DC Source with blocking filter attached	161
C.3	Load diagram for DC voltage source [107]	161

C.4	Characterisation of DC source at Eskom's Megawatt Park test facility	162
D.1	Cylindrical electrodes: anode corona analytical study	165
D.2	Anode corona analytical solution to the total charge on the electrodes	170
D.3	Anode corona analytical solution to the charge on the inner electrode	171
D.4	Anode corona analytical solution to the charge on the outer electrode	171
D.5	Anode corona analytical solution for the positive ion position	171
D.6	Anode corona analytical solution for the electron position	171
D.7	Anode corona analytical solution for the current in a millisecond scale	172
D.8	Anode corona analytical solution for the current in a nanosecond scale	172
D.9	Anode corona analytical solution for current (log-log scale)	173
D.10	Anode corona analytical solution for charge (log-log scale)	173
D.11	Cylindrical electrodes: cathode corona analytical study	173
E.1	Corona inception levels for Zebra conductor at various air pressures	179
E.2	RI magnitude levels for various surface voltage gradients at different heights above sea level	180
E.3	Corona inception levels for Kingbird conductor at various air pressures	181
E.4	RI magnitude levels for various surface voltage gradients at different heights above sea level	181
E.5	Insects attracted to the positive DC conductors, fittings and and generator feed . .	182
E.6	Positive DC wideband measurements with EMI receiver tuned to $500kHz$	183
E.7	Positive DC CISPR narrowband measurements with EMI receiver tuned to $500kHz$	183
E.8	Negative DC wideband measurements with EMI receiver tuned to $500kHz$	183
E.9	Negative DC CISPR narrowband measurements with EMI receiver tuned to $500kHz$	183
E.10	Positive DC wideband measurements with EMI receiver tuned to $500kHz$	184
E.11	Positive DC CISPR narrowband measurements with EMI receiver tuned to $500kHz$	184
E.12	Negative DC wideband measurements with EMI receiver tuned to $500kHz$	184
E.13	Negative DC CISPR narrowband measurements with EMI receiver tuned to $500kHz$	184
E.14	Positive DC wideband measurements with EMI receiver tuned to $500kHz$	185
E.15	Positive DC CISPR narrowband measurements with EMI receiver tuned to $500kHz$	185
E.16	Negative DC wideband measurements with EMI receiver tuned to $500kHz$	185
E.17	Negative DC CISPR narrowband measurements with EMI receiver tuned to $500kHz$	185
E.18	Positive DC wideband measurements with EMI receiver tuned to $500kHz$	186
E.19	Positive DC CISPR narrowband measurements with EMI receiver tuned to $500kHz$	186

E.20 Negative DC wideband measurements with EMI receiver tuned to $500kHz$	186
E.21 Negative DC CISPR narrowband measurements with EMI receiver tuned to $500kHz$	186
E.22 Positive DC wideband measurements with EMI receiver tuned to $500kHz$	187
E.23 Positive DC CISPR narrowband measurements with EMI receiver tuned to $500kHz$	187
E.24 Negative DC wideband measurements with EMI receiver tuned to $500kHz$	187
E.25 Negative DC CISPR narrowband measurements with EMI receiver tuned to $500kHz$	187
E.26 Positive DC wideband measurements with EMI receiver tuned to $500kHz$	188
E.27 Positive DC CISPR narrowband measurements with EMI receiver tuned to $500kHz$	188
E.28 Negative DC wideband measurements with EMI receiver tuned to $500kHz$	188
E.29 Negative DC CISPR narrowband measurements with EMI receiver tuned to $500kHz$	188
E.30 Positive DC quasi-peak results for wideband measurements moving up and down in voltage (Paarl)	189
E.31 Positive DC quasi-keak results for CISPR narrowband measurements moving up and down in voltage (Paarl)	189
E.32 Negative DC quasi-peak results for wideband measurements moving up and down in voltage (Paarl)	189
E.33 Negative DC quasi-peak results for CISPR narrowband measurements moving up and down in voltage (Paarl)	189
E.34 Positive DC quasi-peak results for wideband measurements moving up and down in voltage (Laingsburg)	190
E.35 Positive DC quasi-keak results for CISPR narrowband measurements moving up and down in voltage (Laingsburg)	190
E.36 Negative DC quasi-peak results for wideband measurements moving up and down in voltage (Laingsburg)	190
E.37 Negative DC quasi-peak results for CISPR narrowband measurements moving up and down in voltage (Laingsburg)	190
E.38 Positive DC quasi-peak results for wideband measurements moving up and down in voltage (De Aar)	191
E.39 Positive DC quasi-keak results for CISPR narrowband measurements moving up and down in voltage (De Aar)	191
E.40 Negative DC quasi-peak results for wideband measurements moving up and down in voltage (De Aar)	191
E.41 Negative DC quasi-peak results for CISPR narrowband measurements moving up and down in voltage (De Aar)	191

E.42 Positive DC quasi-peak results for wideband measurements moving up and down in voltage (Midrand) 192

E.43 Positive DC quasi-peak results for CISPR narrowband measurements moving up and down in voltage (Midrand) 192

E.44 Negative DC quasi-peak results for wideband measurements moving up and down in voltage (Midrand) 192

E.45 Negative DC quasi-peak results for CISPR narrowband measurements moving up and down in voltage (Midrand) 192

E.46 Positive DC quasi-peak results for wideband measurements moving up and down in voltage (Clarens) 193

E.47 Positive DC quasi-peak results for CISPR narrowband measurements moving up and down in voltage (Clarens) 193

E.48 Negative DC quasi-peak results for wideband measurements moving up and down in voltage (Clarens) 193

E.49 Negative DC quasi-peak results for CISPR narrowband measurements moving up and down in voltage (Clarens) 193

List of Tables

2.1	Empirical constants for corona onset gradients [13]	14
2.2	Pulse parameters for corona discharge currents	27
2.3	The critical frequencies for different pulse shapes	29
3.1	Set of equations defining computational field solution problem	45
4.1	Results for electron motion in cylindrical configuration	71
4.2	Measured voltage data from electrometer parallel plate calibration	84
4.3	Measured charge data from electrometer parallel plate calibration	84
5.1	Eskom Megawatt Park small corona cage parameters	95
5.2	Eskom Megawatt Park short test line parameters	97
5.3	Eskom Megawatt Park large outdoor corona cage parameters	97
6.1	Capacitances and inductances for conductors in various corona test methods	119
6.2	Characteristic impedances for conductors in various corona test methods	119
6.3	Corona cage excitation functions	135
6.4	Corona cage excitation functions	136
6.5	Parameters defining the IREQ bipolar empirical formula [11]	138
6.6	Parameters defining the IREQ monopolar empirical formula [85]	139
6.7	Altitude correction factors assumed for various prediction formulas	140
E.1	Zebra altitude RI measurement sites and atmospheric conditions	179
E.2	Kingbird altitude RI measurement sites and atmospheric conditions	181

Nomenclature

Abbreviations:

AC	Alternating Current
ACSR	Aluminium Conductor Steel Reinforced
AN	Audible Noise
ANSI	American National Standards Institute
AVG	Average
BPA	Bonneville Power Association
CL	Corona Loss
CISPR	International Special Committee on Radio Interference
CSM	Charge Simulation Method
CST	Computer Simulation Technology TM Electromagnetic Simulation Software
dB	Decibels
DC	Direct Current
DFT	Discrete Fourier Transform
DRC	Democratic Republic of Congo
EM	Electromagnetic
EMC	Electromagnetic Compatibility
EMI	Electromagnetic Interference
EPRI	Electric Power Research Institute
FD	Frequency Domain
FDM	Finite Difference Method
FDTD	Finite Difference Time Domain
FEM	Finite Element Method

FFT	Fast Fourier Transform
HVAC	High Voltage Alternating Current
HVDC	High Voltage Direct Current
IEC	International Electrotechnical Commission
IF	Intermediate Frequency
IREQ	Hydro-Quebec Institute of Research
kV	kilo-Volt
LMM	Linear Multistep Method
mA	milli-Ampere
MW	Megawatt
NB	Narrowband
PD	Partial Discharge
PIC	Particle-In-Cell
PK	Peak
PLC	Power Line Carrier
pdf	Probability Density Function
QP	Quasi-Peak
RAD	Relative Air Density
RBW	Resolution Bandwidth
RF	Radio Frequency
RH	Relative Humidity
RI	Radio Interference
RN	Radio Noise
RMS	Root Mean Square
TD	Time Domain
TVI	Television Interference
SNR	Signal-to-Noise Ratio
STP	Standard Temperature and Pressure
UV	Ultra-violet
VBW	Video Bandwidth

WB	Wideband
WESTCOR	Western Power Corridor

Symbols:

α	Ionization Coefficient
A	Area
A	Neutral Atom
A^*	Excited Atom
A^+	Positive Ion
A^-	Negative Ion
C	Capacitance
δ	Atmospheric Pressure and Temperature Values
D	Diffusion Coefficient
D_e	Electron Diffusion
d	Distance
η	Attachment Coefficient
ϵ_0	Permittivity of Free Space
\vec{E}	Electric Field (Voltage Gradient)
E_c	Corona Inception Gradient
$f(t)$	Time Domain Function
$F(\omega)$	Frequency Domain Function
F_{ph}	Photoionization Coefficient
Γ	Excitation Function
γ	Secondary Ionization Coefficient
$H(s)$	Transfer Function
H	Height Above Sea Level
h	Height
$i(t)$	Current
\vec{J}	Conduction Current
k	Boltzmann's Constant

λ	Line Charge Density
λ	Wavelength
μ_0	Permeability of Free Space
μ_p	Positive Ion Mobility
μ_n	Negative Ion Mobility
m	Particle Mass
∇	Gradient or Directional Derivative
N	Number of Particles
n	Number Density
ϕ	Potential
p	Air Pressure
Q	Charge
q_e	Electron Charge
q_p	Positive Ion Charge
q_n	Negative Ion Charge
r_h	Avalanche Head Radius
r	Radius
S	Surface Area
t	Time
T	Temperature
V	Volume
V	Voltage or Potential
\vec{v}	Velocity
v_c	Collision Frequency
v_e	Electron Drift Velocity
Z_0	Characteristic Impedance
Z_m	Townsend Energy Factor

Abstract

Direct Current Conductor Corona Modelling and Metrology

A.J. Otto

Department of Electrical Engineering

University of Stellenbosch

Private Bag X1, 7602 Matieland, South Africa

Dissertation: PhD (Electrical Engineering)

September 2009

Prospects of up-rating existing high voltage direct current (HVDC) transmission schemes, as well as the conversion of existing alternating current (AC) to direct current (DC) lines and the development of new HVDC schemes in sub-Saharan Africa, have led to renewed interest in DC research. The radio interference (RI), audible noise (AN) and corona loss (CL) performance of HVDC transmission lines are critical factors when assessing the reliability of the line design. The RI performance is especially important when considering the successful transmission of the carrier signal of the power line carrier (PLC) system. The PLC system is the main form of communication between teleprotection devices on the Cahora Bassa HVDC scheme.

The aim of the dissertation is to devise modelling as well as metrological techniques to characterise DC conductor corona. A particle-in-cell (PIC) computational code is developed to gain a better understanding of the physical processes that occur during corona events. The numerical code makes use of the charge simulation method (CSM) and finite element method (FEM) to solve for the Laplace and Poisson field equations. Higher-order basis functions are implemented to obtain a more accurate solution to the Poisson equation. The computational tool yields insight into the mathematical models for the various ionization, attachment and electron avalanche processes that give rise to corona currents. Together with a designed and developed electrometer-type circuit, the numerical code assists the visualisation of the space

charge particle dynamics that form in the electrode gap during corona events.

The metrological techniques consider the wideband time domain (TD) as well as the frequency domain (FD) information of the measured corona pulses in the presence of noise. These are then compared to the narrowband CISPR standard measurements centred around 500kHz. The importance of impedance matching when attempting to derive a wideband excitation function is investigated. The TD measurements are quite distinct from the well-published FD measurements, and consider the pulse shape, pulse spectrum and pulse repetition rates. The use of three possible conductor corona test methods to study direct current conductor RI performance under both positive and negative polarities is investigated at high altitude in this dissertation. These include a small corona cage, a short test line and the Eskom Megawatt Park large outdoor corona cage. Derived wideband and narrowband monopolar DC RI excitation functions at 500kHz are consolidated with existing radio noise (RN) measurement protocols and prediction methods.

The use of a corona cage to derive excitation functions for monopolar RI predictions is explored and it is shown that a small corona cage, due to the build-up of space charge in the small distance between the electrodes, cannot be used to predict the RI levels on HVDC transmission lines accurately. As a consequence of the physics, computational modelling and both frequency and time domain measurements, it is now possible to explain why a small cage system prevents the accurate RI prediction on transmission lines. The large outdoor corona cage and short test line RI performance predictions agree with existing empirical prediction formulas.

Opsomming

Gelykstroomgeleier Koronamodellering en Meettegnieke

A.J. Otto

Departement Elektroniese Ingenieurswese

Universiteit van Stellenbosch

Privaatsak X1, 7602 Matieland, Suid Afrika

Proefskrif: PhD (Elektriese Ingenieurswese)

September 2009

Vooruitsigte van die opgradering van bestaande hoogspanningsgelykstroom transmissielyn skemas, asook die omkering van bestaande wisselstroom na gelykstroom lyne en die ontwikkeling van nuwe hoogspanningsgelykstroom skemas in sub-Sahara Afrika, het gelei to hernude belangstelling in gelykstroombnavorsing. Die korona-werkverrigting van hoogspanningsgelykstroom oorshoofselyne in terme van radiosteuring, hoorbare-geraas en koronaverliese is kritiese faktore om in aanmerking te neem wanneer die betroubaarheid van die lynontwerp geëvalueer word. Die radiosteuring-werkverrigting is veral van belang tot die suksesvolle oordrag van die kraglyn-dragolf draersein wat die hoof kommunikasievorm tussen beskermingstoerusting op die Cahora Bassa transmissielyn skema is.

Die doel van hierdie proefskrif is om modellering- sowel as meettegnieke te ontwerp om gelykstroomgeleierkorona te karakteriseer. 'n Partikel-in-sel numeriese kode is ontwikkel om 'n beter begrip te verkry van die fisiese prosesse gedurende koronagebeure. Die numeriese kode maak gebruik van die lading-simulasiemetode, sowel as die eindige element metode om die Laplace en Poisson veldvergelykings op te los. Hoër-orde basisfunksies is geimplimenteer om 'n meer akkurate oplossing vir die Poisson vergelyking te verkry. Die numeriese kode bied insig tot die wiskundige modelle vir die verskeie ionisasie-, aanhegtings- en lawineprosesse wat lei tot koronastrome in die area om die hoogspanningsgeleier. Die numeriese kode, saam met 'n elektro-

meter wat ontwerp en ontwikkel is, dra by tot die begrip van die ruimtelading partikeldinamika wat ontstaan in die elektrodegaping gedurende koronagebeure.

Die meettegnieke neem die wyeband tydgebied- en frekwensiegebiedinformatie van die koronapulse in ag in die teenwoordigheid van geraas. Dit word dan vergelyk met die nouband CISPR meetstandaard vir 'n frekwensie van 500kHz. Die belangrikheid van impedansie-aanpassing vir wyeband metings met die doel om opwekkingsfunksies af te lei, word ondersoek. Die tydgebiedmetings verskil van die algemene frekwensiegebiedmetings, en ondersoek die pulsvorm, -spektrum en -herhalingskoers. Die gebruik van drie moontlike koronageleier-toetsmetodes om gelykstroom radiosteuring-werkverrigting vir positiewe en negatiewe polariteite te bestudeer by hoë vlakke bo seespieël word ondersoek in die proefskrif. Dit sluit in 'n klein koronakou, 'n kort toetslyn en die Eskom Megawatt Park groot buitelug-koronakou. Afgeleide wye- en nouband monopolêre gelykstroom radiosteuring opwekkingsfunksies by 500kHz word gekonsolideer met bestaande radioruis metingsprotokolle en voorspellingsmetodes.

Die gebruik van 'n koronakou om opwekkingsfunksies af te lei vir monopolêre radiosteuringvoorspellings is ondersoek en daar is gevind dat 'n klein koronakou nie gebruik kan word om radiosteuringvlakke op hoogspanningsgelykstroom transmissielyste akkuraat te voorspel nie. Dit is as gevolg van die opbou van ruimtelading in die klein elektrodegaping. Met behulp van die fisika, numeriese modellering en beide die frekwensie- en tydgebiedmetings, is dit nou moontlik om te verklaar waarom die klein koronakou die akkurate radiosteuringvoorspellings op transmissielyste onmoontlik maak. Die groot buitelug-koronakou en kort toetslyn radiosteuringvoorspellings stem ooreen met bestaande empiriese voorspellings formules.

Chapter 1

Introduction

1.1 Operational Experience

Eskom has been the sole power utility of South Africa since 1923. The only operational experience with high voltage direct current (HVDC) transmission that Eskom has had to date is that of the Cahora Bassa scheme. This HVDC transmission scheme was commissioned in three stages starting in March 1977, with full operation achieved in June 1979.

The bipolar scheme, rated at $\pm 533\text{kV}$, can transfer roughly 1800 megawatt (MW) of power generated by the hydro-electric scheme in Songo (Mozambique) over a distance of about 1400km to the Apollo converter station in Tshwane (South Africa). The distance between the two pole-conductors is roughly 1 to 2km, effectively transforming the scheme into two monopolar transmission lines of positive and negative polarity. The pole conductor consists of a quad-Zambezi configuration, while an Oden aluminium conductor with steel reinforcement (ACSR) is used as an insulated shieldwire (earth return wire) [1]. The Cahora Bassa transmission line is shown in figure 1.1. The scheme furthermore uses power line carrier (PLC) as the main form of communication between protection devices. It is therefore important to ensure the successful transfer of this carrier signal. The Oden shieldwire, situated with an offset above the pole conductor, is used as an earth return path for the carrier signal. Further detail about this HVDC transmission line can be found in [2].

Noise and ionic coupling onto the insulated shieldwire due to corona on the pole conductor can decrease the signal-to-noise ratio (SNR) substantially. High electric field coupling to the shieldwire can result in corona inception on this conductor, also reducing the SNR. The posi-

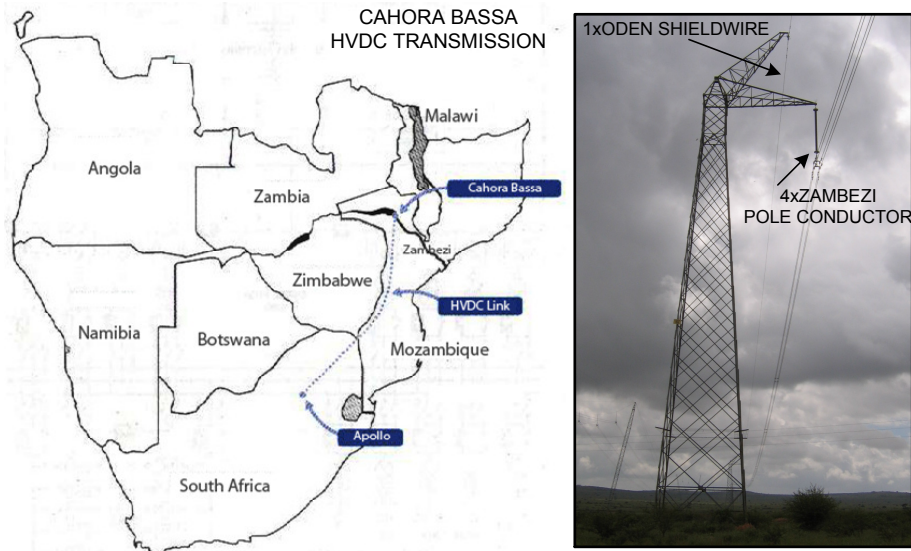


Figure 1.1: Cahora Bassa HVDC scheme with quad Zambezi pole conductor and Oden insulated shieldwire [3] (Map taken from [1])

tive pole conductor inducing a negative charge on the insulated shieldwire, and vice versa, were investigated in [4]. Characterising corona excitation functions and corona effects like radio interference (RI), audible noise (AN) and corona loss (CL) for communication system and line design are therefore important.

1.2 Eskom's Need for HVDC Research

High voltage alternating current (HVAC) transmission lines have one major disadvantage. The inductive and capacitive elements, as well as quarter wavelength effects of overhead HVAC lines limit the transmission capacity and transmission distance. In fact, any line length approaching a quarter wavelength is impractical without some means of compensation [5]. With no charging current and extra losses as in HVAC systems, these are problems that have been overcome successfully by using HVDC transmission schemes. Innovations in the field of HVDC transmission systems over the years have indeed made this a reliable technology with economic benefits for users all over the world.

Due to the ever increasing demands on Eskom to deliver large amounts of power over long distances, while always having a comfortable surplus margin, several HVDC projects are being considered. As discussed in section 1.1, the Cahora Bassa hydro-electric scheme is the only

operational experience with HVDC transmission that Eskom has to date. The up-rating of the existing Cahora Bassa scheme of $\pm 533\text{kV}$ to $\pm 600\text{kV}$ is being considered in order to keep up with the power demands. Other projects in the not so distant future may include the WESTCOR (Western Power Corridor) and Waterberg Power Corridor projects [6].

The WESTCOR project will deliver power generated from the hydro-electric scheme in the Democratic Republic of Congo (DRC) all the way through to South Africa. This is a distance of nearly 3000km and spans from the DRC through Angola, Namibia, Botswana and South Africa. These countries all form part of the South African Power Pool (SAPP) as shown in figure 1.2. The planned rating for this HVDC transmission scheme is $\pm 800\text{kV}$ [7]. Also in the planning stages is the Waterberg Power Corridor project. Both HVAC and HVDC transmission schemes are being considered for power transfer. Again a direct current (DC) rating of $\pm 800\text{kV}$ is proposed, with initial operating voltage of $\pm 600\text{kV}$. The HVAC scheme is to be rated at 765kV [6].

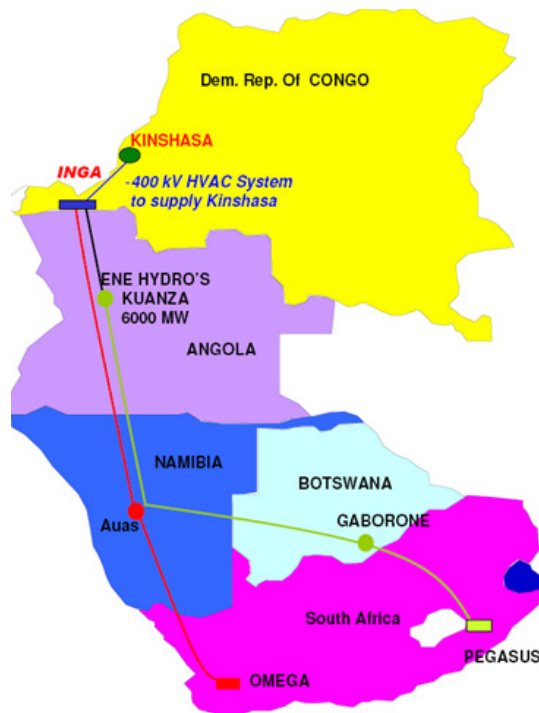


Figure 1.2: South African Power Pool (SAPP) countries involved in the Westcor power project [3]

It is understandable from all the prospects of new HVDC transmission schemes in sub-Saharan

Africa why there is a renewed interest in HVDC research. It is also clear that it is important for Eskom to be able to predict the corona levels when doing line design for these new projects.

1.3 Research Objectives

The research in this dissertation investigates aspects of HVDC conductor corona, particularly the modelling and the metrological techniques necessary for its analysis and prediction. The time domain (TD) as well as the frequency domain (FD) information of the DC corona pulses are of interest in the characterisation of the conducted RI levels. One of the main objectives is to devise metrological techniques to characterise corona in the presence of noise. This is done to derive the necessary excitation functions for corona performance predictions that are required for line design. Considering the aforementioned objectives, a better understanding is needed of the particle dynamics and physical processes that give rise to corona events in measurement systems.

Various conductor corona test methods exist for evaluating the corona performance of conductors used on high voltage alternating current (HVAC) transmission schemes. The main difference, however, between high voltage direct current (HVDC) and HVAC transmission schemes is the continuous formation and build-up of space charge due to the electrostatic field of the former. The space charge plays a critical role in the formation and suppression processes of DC corona, and it is uncertain whether the same conductor test methods can be used to evaluate and predict the corona performance of HVDC conductors. Useful experimental data, gathered from test methods that are readily available to Eskom, are important to the power utility for predicting corona performance of conductors in HVDC line design. DC conductor corona test methods proposed in this dissertation are characterised, and the possibility of using a corona cage for RI predictions is investigated.

The derivation of excitation functions using wideband time domain techniques is considered. This is different from the well-published and commonly used methods employing only frequency domain techniques. An attempt is made to isolate corona events beyond inception using time domain and signal processing techniques. The time domain approach investigates the shape, spectrum and repetition rate of the pulses. The importance of correct impedance matching for wideband measurements is explored. Detailed attention is given to the characterisation of the measurement systems, especially the wideband and narrowband decoupling networks required

to measure the conducted RI. Both wideband and narrowband excitation functions are derived and compared to empirical prediction formulas. Characteristics of corona noise levels at both polarities and at various surface voltage gradients with regards to the conditions of the conductor are investigated. Initial tests considering the effect of altitude on the inception of the corona processes, as well as the RI levels, are examined using a portable corona cage. Collectively, the research claims in this dissertation should lead to better line design methodologies for new schemes proposed for sub-Saharan Africa.

1.4 Claims Made by This Dissertation

This dissertation presents an extensive physics overview that encapsulates the major processes that give rise to corona discharges. A particle-in-cell (PIC) computational code, using the charge simulation method (CSM) and finite element method (FEM) for the solution of the Laplace and Poisson field equations, is developed. Higher-order basis functions are successfully implemented in the FEM to obtain a more accurate electric field solution for Poisson's equation. The computational tool facilitates the visualisation of the various ionization, attachment and electron avalanche processes. Together with a designed and developed electrometer-type circuit, this enhances understanding of the space charge particle dynamics that form in the electrode gap during corona events. The PIC numerical code and electrometer-type circuit provide a spatial-temporal view of the ion space charge created during a single corona event reaching the measurement system's earth electrode. At the ground electrode, the space charge will take a certain time to be cleared out of the measurement system due to the time constants defined by the capacitance, resistance and inductance. This implies that if the space charge is not cleared fast enough between corona events, the accumulated space charge from a preceding corona event could repel approaching ions from a following event. This will cause space charge to build up inside the electrode gap, resulting in a distortion of the electric field. The conductor surface voltage gradient and inception levels will also be affected. The computational tool, electrometer-type circuit and understanding of the physics assisted in the characterisation and evaluation of the various corona performance test methods investigated in the dissertation.

Three possible conductor corona test methods, including a small corona cage, a short test line and the Eskom Megawatt Park large outdoor corona cage to study DC conductor RI performance are explored. A critical evaluation of the measurement systems and surrounding environment is made. The transfer functions and earthing structures of the various systems

are investigated using a current probe and spectrum analyser. The background environment in terms of radio noise (RN) coupling to the measurement systems is characterised. It is shown that the outer structure of the large outdoor corona cage at the Eskom Megawatt Park corona test facility provides excellent shielding against background RN coupling. It is found using time domain reflectometry (TDR) techniques that a large percentage of a known fast rising pulse injected at the one end of the conductor is reflected back as soon as it reaches the opening of the large corona cage. This is due to the change in effective characteristic impedance experienced by the pulse at the 4m length of conductor above ground going into the 3.5m radius coaxial structure. This is the first time that the large corona cage and decoupling networks at these local high voltage test facilities are investigated in such detail.

Various metrological techniques are applied to characterise DC corona in the presence of noise. These include wideband, narrowband, time domain as well as frequency domain techniques. The results obtained by applying the various techniques correlate. A high-speed data-acquisition sampling card was used to measure high resolution time domain pulse trains to study the shape, repetition rate and spectrum of the pulses. The wideband time domain techniques for DC RI performance prediction applied in this study are distinct from generally used frequency domain techniques. The importance of correct impedance matching is shown for wideband measurements. Both positive and negative polarity measurements are done at high altitude. Derived wideband and narrowband monopolar RI excitation functions at 500kHz are consolidated with existing RN measurement protocols and prediction methods. The ability to derive the excitation functions from wideband measurements is important as it implies that it can be derived for frequencies other than the 500kHz relevant to the power line carrier (PLC) systems. Due to the quasi-peak detectors in CISPR and ANSI EMI receivers being centred around 500kHz and 1MHz respectively, and only frequency domain methods usually applied to RI measurements, this derivation was not possible previously. As a result, the variation of the RN with frequency can also be investigated.

In this dissertation it is concluded that a small corona cage cannot be used to predict the RI levels on HVDC transmission lines accurately. This is due to the build-up of space charge in the small distance between the electrodes. As a consequence of the physics, computational modelling and both frequency and time domain measurements, it is now possible to explain why a small cage system prevents the accurate RI prediction on transmission lines. The large outdoor corona cage and short test line RI performance predictions correlate and agree with

existing empirical prediction formulas.

1.5 Dissertation Layout

A flowchart of the layout of the dissertation is presented in figure 1.3. To accurately predict corona noise on a transmission line, it is important to understand the physical processes involved that give rise to corona current. Chapter 2 provides an overview of these processes and the effect of the space charge created during corona events on electric field and ionic currents.

The PIC computational model developed to facilitate the visualisation of the physical processes and how they give rise to corona currents is presented in Chapter 3. The processes include the ionization, attachment and the formation of space charge during the electron avalanches in highly stressed areas surrounding conductors, as well as the drift and diffusion of these particles due to the force vectors of the electric field.

The design and development of an electrometer-type circuit used to measure the space charge created during corona events are discussed in Chapter 4. The electrometer-type circuit, together with the computational model described in Chapter 3, give insight into the particle dynamics in the electrode gap during corona events. Simulation results and electrical measurement environment predictions are discussed in this chapter.

Chapter 5 considers the characterisation of the corona test methods. This includes the importance of impedance matching and characterisation of the corona cage and test line configurations when doing time and frequency domain wideband and narrowband measurements.

A comparative study using a large outdoor corona cage, a small corona cage and a short test line at high altitude (1550m above sea level) to evaluate DC conductor RI performance is done in Chapter 6. Excitation functions are derived and compared to various empirical RI prediction formulas.

The dissertation concludes in Chapter 7. Recommendations for future work and research are made.

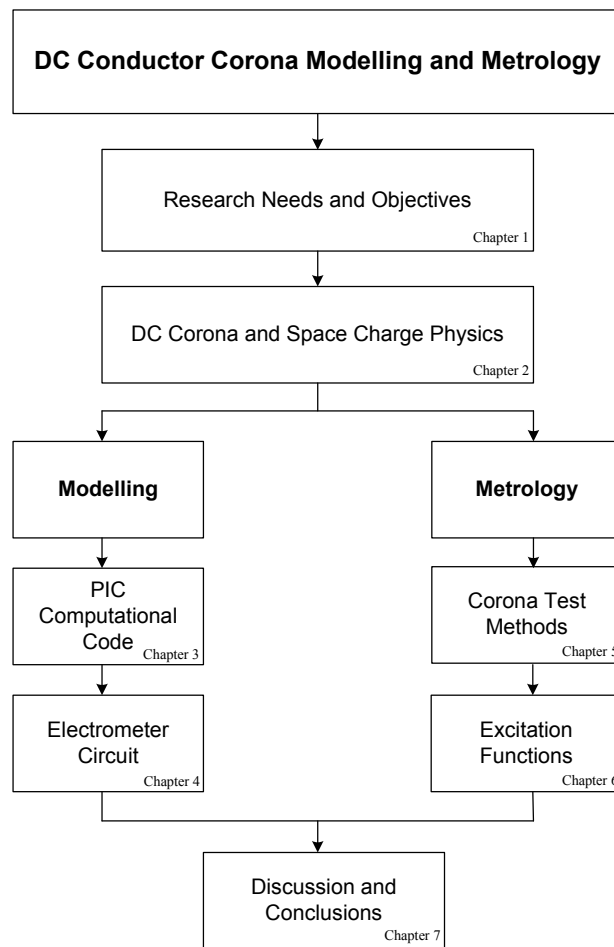


Figure 1.3: Flowchart for dissertation layout

Chapter 2

Direct Current Corona and Gap Discharges

This chapter provides an overview on the physical processes leading to corona and gap discharges, especially in high voltage direct current (HVDC) transmission schemes. It further investigates the effects of the space charge formation and build-up on the electrical environment as a result of the electrostatic field of a highly stressed DC conductor.

2.1 Corona Discharges

Corona can be defined as a self-sustained, partial electrical discharge in which the field-intensified ionization is localized over only a portion of the distance between the electrodes. This partial discharge precedes total gas breakdown. The type of discharge resulting in a spark or breakdown of a gap depends on the gas pressure, the gap length and shape, as well as the nature of the applied voltage [8]. Corona as a partial discharge can therefore be caused by a non-uniform electric field as between electrodes in a coaxial geometry [9]. When the applied voltage is above a certain critical voltage, free electrons will be accelerated in the highly stressed area surrounding the conductor and cause excitation and ionization of the neutral air molecules. This results in the self-sustained discharge which produce significant macroscopic events.

2.1.1 Corona Inception

This critical voltage or conductor surface gradient is often referred to as the *corona inception voltage* or *corona onset gradient* [10]. The corona onset gradient, given in [11] by equation

2.1.1, is a function of the conductor diameter, ambient pressure, humidity and temperature [12].

$$E_c = mE_0\delta\left(1 + \frac{K}{\sqrt{\delta r_c}}\right) \quad (2.1.1)$$

In 2.1.1, E_0 and K are empirical constants depending on the nature of the applied voltage, δ is the relative air density, r_c is the conductor radius in cm and m is the conductor surface roughness factor. The empirical values according to [13] are given in table 2.1, while δ is given by equation 2.1.2.

$$\delta = \frac{273 + t_0}{273 + t} \cdot \frac{p}{p_0} \quad (2.1.2)$$

In equation 2.1.2, t is the temperature and p is the pressure of ambient air, while $t_0 = 25^\circ C$ and $p_0 = 760 \text{ torr}$ are standard temperature and pressure (STP) reference values. The dielectric strength of air at STP is given in [14] as 3kV/mm or 30kV/cm.

Corona Onset Gradient Empirical Constants		
	E_0	K
+DC	33.7	0.24
-DC	31.0	0.308

Table 2.1: Empirical constants for corona onset gradients [13]

A similar form for the corona inception voltage gradient is also given by [15] as

$$E_c = 3m\delta\left(1 + \frac{0.301}{\sqrt{\delta r_c}}\right) \quad (2.1.3)$$

where E_c is the onset in kV/mm. The conductor surface condition factor, m in equation 2.1.3, is said to be between 0.8 and 0.9 for a dry aged conductor, and 0.5 and 0.7 for a conductor under foul weather conditions. The air density factor is given by [15] as

$$\delta = \frac{0.392b}{273 + t} \quad (2.1.4)$$

where b is the barometric air pressure in mmHg. It is noted in [11] that the empirical formulas

were often derived from laboratory experiments using a smooth conductor with diameters much smaller than those used on practical transmission lines. These formulas, when extrapolated to actual conductor sizes used on transmission lines, have been found to be higher than when measured. To understand the physical gas discharge processes that lead to corona, one first has to understand air as the main insulating medium around high voltage conductors.

2.2 Air as insulating medium

More often than not, atmospheric or ambient air is the main insulating medium between the high voltage conductors and the ground plane in a power transmission scheme. It is therefore important to understand the physical and electrical characteristics of ambient air that allow it to maintain or disrupt insulation. For ordinary air at room temperature the number density of neutral atoms (n_n), measured in *number per cm³*, can be taken as $n_n \approx 3 \times 10^{19}$ [16]. As discussed before, the discharge phenomena known as corona is a result of sufficiently high levels of conductor surface electric fields that cause excitation and ionization to take place in the air surrounding the high voltage conductor. An understanding of the basic processes of corona physics is important to evaluate the corona performance of transmission lines in terms of radio interference (RI), audible noise (AN) and corona loss (CL).

Atmospheric air consists of a number of gases as well as water vapour. The volume percentage of the latter depends on the ambient temperature that is at its highest at the equator and decreases toward the poles of the earth. The volume percentage of the gaseous content of dry air however does not vary significantly from one region to another. These gaseous components are typically 78.09% Nitrogen, 20.95% Oxygen, 0.93% Argon and traces of Carbon Dioxide, Neon, Krypton etc. [11]. The gaseous and water vapour molecules are electrically neutral under normal conditions with no added or removed electrons. There are however naturally occurring phenomena that will ionize the gas molecules causing free electrons and positive ions. These free electrons will very quickly combine with oxygen molecules to form negative ions. Ambient air at sea level usually has around 1000 positive ions and 1000 negative ions per cubic centimetre [11]. This means that although there is a very low concentration of charged particles, air is slightly conductive and not a perfect insulation medium. This implies that under the appropriate electric field conditions air will be susceptible to electrical discharge phenomena such as breakdown and corona.

2.2.1 Classical Atomic Theory

The *classical atom theory* is based on Bohr's classical model of the Hydrogen atom. In this theory an atom consists of a *nucleus*, composed of *neutrons* and *protons*, surrounded by *electrons* in orbital motion [17] shown in figure 2.1. The nucleus is very much smaller than the overall size of the atom, and the particles therein are held together by a strong nuclear interaction. The number of electrons is different for each element and is the same as the number of protons in the nucleus of a *neutrally* charged atom [18].

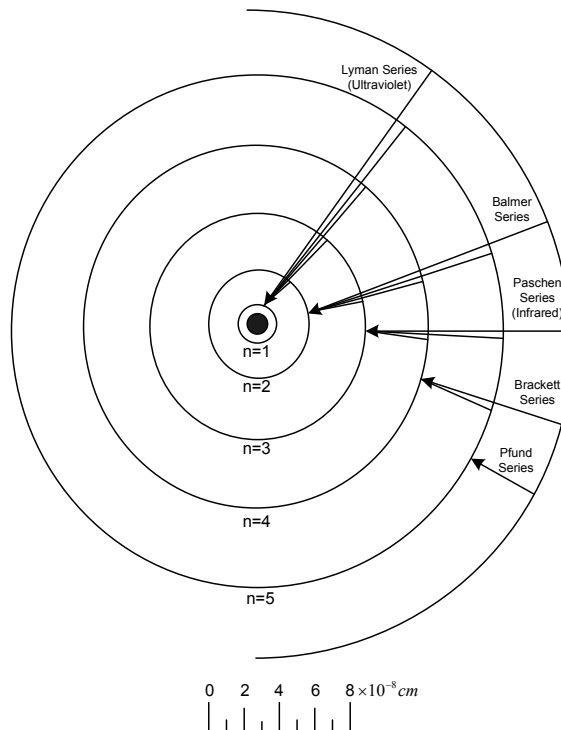


Figure 2.1: Bohr model of the Hydrogen atom with “permitted” orbits of an electron [18]

The electrons occupy orbits around the nucleus which are characterised by different permissible energy states. These possible states are numbered in figure 2.1 by values of integer n referred to as the *quantum number*. The electron in the orbit with the lowest energy ($n=1$ or *ground state*) is closest to the nucleus while the electron in the orbit with the highest permissible energy state is the furthest away from the nucleus. Atoms may temporarily acquire enough energy, as a result of colliding electrons, to raise the electron to a higher energy state. The atom is then said to be in the *excited state*. This state is, however, unstable and the electron will eventually fall back to its original state. According to Bohr an atom radiates and emits a photon when

an electron makes a transition from one permissible orbit to another [18]. The atomic mass of the atom is determined by the number of neutrons or protons. The charge of an electron has the same magnitude as that of a proton ($|q| = 1.602 \times 10^{-19}C$), while the mass of the proton ($m_p = 1.673 \times 10^{-27}kg$) and neutron ($m_n = 1.675 \times 10^{-27}kg$) are nearly equal and much heavier than that of the electron ($m_e = 9.110 \times 10^{-31}kg$). Under normal conditions the negative charge of the electrons is balanced out by the positive charge of the protons in the nucleus, and the atom is said to be *electrically neutral*. Ionization is when one or more of the electrons are gained or lost by the atom [19]. The various excitation and ionization processes are discussed in section 2.3.

2.3 The Gas Discharge Processes

When a free electron is accelerated in the region close to a highly stressed electrode, collisions with neutral air molecules cause excitation and ionization of these uncharged particles and develop successive electron avalanches [20]. These collisions between the free electrons and neutral air molecules usually occur along the mean free path in the direction of the electric field. The effectiveness of ionization depends upon the energy that charged particles gain as they accelerate under the influence of electric stress [21]. If energy imparted during the collision is large enough to dislodge an orbiting electron far away from the atom, the atom is said to be ionized. The mixture of ionized and neutral particles is what is then called a *plasma* or ionized gas [22]. It is noted in [11] that the energy imparted on the atom mostly affects the electron in the outermost orbit.

2.3.1 Ionization

An atom (A) is said to be *ionized* (A^+) if the energy imparted is large enough to dislodge an orbiting electron sufficiently far away from the atom such that it will not return to its original state. This is shown in equation 2.3.1.



The removal of the electron will result in an electrically positive atom or a *positive ion* (A^+), as well as a free electron (e) [22]. There are several physical processes by which an atom can absorb energy. These include *electron collisions*, *ion collisions*, *photoionization* and *excitation*

and *thermionic ionization and excitation* [17].

2.3.2 Excitation

Colliding particles with energy less than ionization energy may, on collision, excite the gas atoms to higher states [21]. An atom (A) is said to be *excited* (A^*) when sufficient energy is given to the atom to allow the electron in the outermost orbit to jump to the next permissible higher energy level, as shown in equation 2.3.2. The electron in this state becomes more loosely attached to the atom [17]. The electron very quickly relaxes to its original state and the excess energy is radiated as a photon having energy $h\nu$, where ν is the frequency of radiation and h is Planck's constant [11],[23].



The atom can only absorb finite and discrete amounts of energy corresponding to the difference in energy between the two allowed states. An atom recovers from an excited state within 10^{-7} to 10^{-10} seconds during which time the excess energy is radiated as a *photon*. The photon can again lead to secondary ionization processes as discussed in section 2.3.3. It is furthermore important to note from [11] that the size of a colliding particle also plays a role in the ionization process. A scenario of a colliding particle (electron) with a mass very small compared to that of the neutral atom is presented. In this case almost all of the electron's kinetic energy might be transferred to increase the internal energy of the atom, consequently exciting rather than ionizing the atom.

2.3.3 Secondary Ionization

The released energy from an excitation process may ionize another atom whose ionization energy is equal to or less than the photon energy. This process is referred to as photoionization, which in [21] is defined as secondary ionization. The photoionization process is shown in equation 2.3.3.



Various other ionization methods in air, including *thermal ionization, nuclear emission* and

electric field ionization are discussed in [14]. Another type of ionization can be in the form *electron emission*, which is the process of liberating an electron from a solid, especially boundary surfaces (electrodes). Ionization due to *cathode collision* is also a secondary mechanism. This contributes greatly to the increase in the number of charged particles and thus higher plasma conductivity [22].

2.3.4 Attachment and Detachment

Atoms or molecules that lack one or two electrons in their outer orbits tend to capture free electrons, resulting in the formation of negative ions (A^-). The types of gases with atoms of this tendency are called *electronegative gases*. The process whereby negative ions are formed is referred to as electron *attachment*. The energy required for *detachment* (to remove an electron from a negative ion and restore neutrality), is called the electron affinity of the atom [24]. The attachment process is shown by equation 2.3.4.



2.3.5 Recombination

In the case where positive and negatively charged particles coexist in a gas, the process of *recombination* can occur. The recombination process is shown in [11] to be such that



In equation 2.3.5 B^- can be an electron or negatively charged ion. Radiative recombination is in certain aspects the reversal of photoionization and occurs only with electrons. The recombination process of positively and negatively charged ions is quite complex and consists of two phases. During the first phase the two ions execute elliptical or hyperbolic orbits through the action of Coulomb forces about their common centre of mass. The second phase is the charge transfer that takes place during the orbital encounter. This leads to neutralization. The neutralized particles then move away from each other, following their trajectories while increasing their kinetic energy by the difference between the ionization energy of the positive ion, and the electron affinity of the negative ion [11].

2.4 Gas Discharge Coefficients

The theoretical analysis to determine the ionization, attachment and diffusion coefficients, as well as the mobility for electrons and ions, is very complex. These values are often determined through experimental methods and empirical formulas [6]. This section investigates the different gas discharge coefficients as discussed in [25]. These empirical values are furthermore used in the numerical particle-in-cell (PIC) simulation discussed in chapter 3. Each discharge coefficient is calculated and displayed for two temperatures values, namely $T = 20^\circ C$ and $T = 50^\circ C$.

2.4.1 Ionization Coefficient (α)

In order to obtain an estimate of the process of *ionization* the electron energy distribution in a gas discharge has to be taken into account. An ionization coefficient α was defined by Townsend [26] as the number of electron-ion pairs produced in the gas by a single electron moving through a unit distance in the direction of the field. The number of electrons produced by $n(x)$ electrons advancing a distance dx in the direction of the field is given by equation 2.4.1 [11].

$$dn = n(x)\alpha dx \quad (2.4.1)$$

Assuming at $x = 0$ that $n = n_0$, then

$$\ln\left(\frac{n}{n_0}\right) = \int_0^x \alpha dx \quad (2.4.2)$$

In an *uniform* field the number of electrons is given by equation 2.4.3

$$n = n_0 e^{\alpha x} \quad (2.4.3)$$

This means, physically, that if diffusion and recombination is neglected, one electron will form $e^{\alpha x}$ electrons when traversing a distance x from the cathode to the anode [8]. In the case of a *non-uniform* field where α varies as a function of the electric field, the number of electrons is given by

$$n = n_0 e^{\int_0^x \alpha dx} \quad (2.4.4)$$

The dependence of the quantity α on the electric field E and pressure p can be written in the form of equation 2.4.5.

$$\frac{\alpha}{p} = f\left(\frac{E}{p}\right) \quad (2.4.5)$$

The empirical expression used in [12] is adapted for temperature dependency in [25], and is given by equation 2.4.6. The ionization coefficient values for air temperature values of $T = 20^\circ\text{C}$ and $T = 50^\circ\text{C}$ are shown in figures 2.2 and 2.3 for values of $25 \leq \frac{E}{p} < 60$ and $60 \leq \frac{E}{p} \leq 240 \frac{\text{V}}{\text{cm}\cdot\text{torr}}$ respectively.

$$\frac{\alpha(p, T)}{p} = \begin{cases} 4.778 \frac{293}{T} \exp\left(-\frac{221}{\frac{E}{p} \frac{T}{293}}\right) & \text{for } 25 \leq \frac{E}{p} < 60 \frac{\text{V}}{\text{cm}\cdot\text{torr}} \\ 9.682 \frac{293}{T} \exp\left(-\frac{264.2}{\frac{E}{p} \frac{T}{293}}\right) & \text{for } 60 \leq \frac{E}{p} \leq 240 \frac{\text{V}}{\text{cm}\cdot\text{torr}} \end{cases} \quad (2.4.6)$$

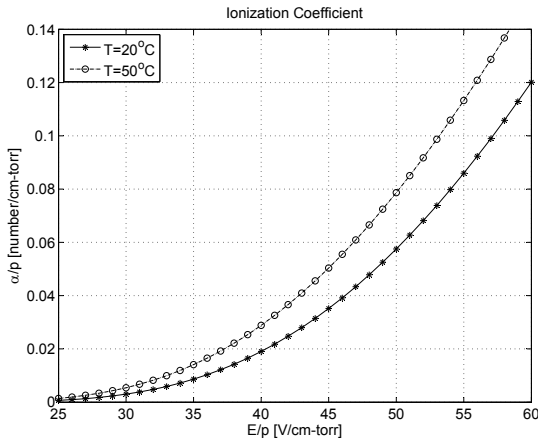


Figure 2.2: Ionization data in air for electric field per pressure values of $25 \leq E/p \leq 60 \frac{\text{V}}{\text{cm}\cdot\text{torr}}$

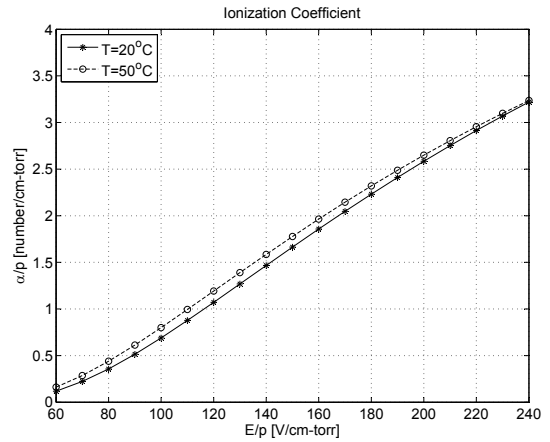


Figure 2.3: Ionization data in air for electric field per pressure values of $60 < E/p \leq 240 \frac{\text{V}}{\text{cm}\cdot\text{torr}}$

2.4.2 Attachment Coefficient (η)

Electronegative gases lacking one or two electrons in their outer orbits have the tendency to accept free electrons and become *negative ions*. The energy that is necessary to remove an electron from a negative ion, thereby returning it to a neutral atom, is called the *electron affinity* of the atom.

The *attachment coefficient* η is the number of *negative ions* created as a single electron moves a unit distance through the gas in the direction of the applied field [11]. The number of electrons *lost* due to the attachment from $n(x)$ electrons moving a distance dx in the direction of the field is given by

$$dn = -n(x)\eta dx \quad (2.4.7)$$

Again assuming for a *uniform field* at $x = 0$ that $n = n_0$, then

$$n = n_0 e^{-\eta x} \quad (2.4.8)$$

In the case of a *non-uniform field*, the number of electrons lost is given by equation 2.4.9.

$$n = n_0 e^{\int_0^x -\eta dx} \quad (2.4.9)$$

Since *ionization* and *attachment* usually takes place at the same time, the effects can be combined to obtain for a *uniform field* as per equation 2.4.10.

$$n = n_0 e^{(\alpha-\eta)x} \quad (2.4.10)$$

While for a *non-uniform field* as per equation 2.4.11.

$$n = n_0 e^{\int_0^x (\alpha-\eta) dx} \quad (2.4.11)$$

The dependence of the quantity η on the electric field E and pressure p can be written in the form of equation 2.4.12.

$$\frac{\eta}{p} = f\left(\frac{E}{p}\right) \quad (2.4.12)$$

The empirical expression adapted for temperature dependency in [25] is given by equation 2.4.13. The attachment coefficient values for air temperature values of $T = 20^\circ C$ and $T = 50^\circ C$

are shown in figure 2.4.

$$\begin{aligned} \frac{\eta(p, T)}{p} = & \left(\frac{293}{T}\right) \left[0.01298 - 0.541 \times 10^{-3} \left(\frac{E}{p} \frac{T}{293}\right) \right. \\ & \left. + 0.87 \times 10^{-5} \left(\frac{E}{p} \frac{T}{293}\right)^2 \right] \end{aligned} \quad (2.4.13)$$

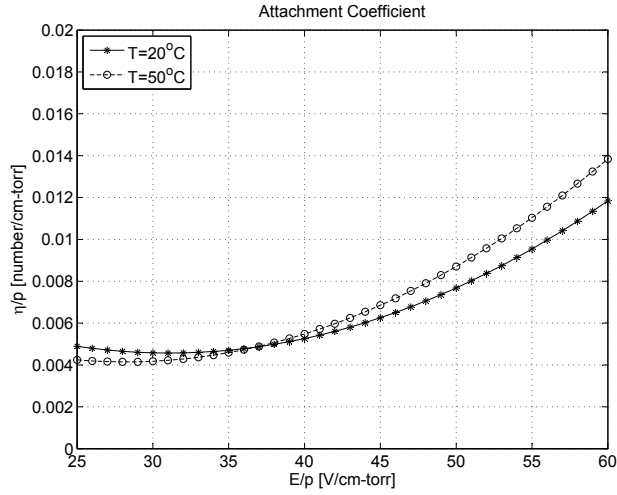


Figure 2.4: Attachment data in air for electric field per pressure values of $25 \leq E/p \leq 60 \frac{V}{cm \cdot torr}$

2.4.3 Photoionization Coefficient (γ)

The secondary ionization mechanism known as *photoionization* was discussed in section 2.3.3. This process is essential in some corona discharge as it initiates the secondary and tertiary avalanche and ionization processes. Photoionization data in air with $\frac{E}{p}$ ranging from 50 to 200V/cm · torr was measured by [27] in Germany and [28] in the U.S.A. with $\frac{E}{p} = 3500V/cm \cdot torr$. The empirical expression for the photoionization coefficient as a function of pressure and temperature is given by $F_{ph}(p, T)$ in equation 2.4.14, and is shown for air temperature values of $T = 20^\circ C$ and $T = 50^\circ C$ in figure 2.5.

$$\begin{aligned} F_{ph}(p, T) = & 10^{-6} \left[7.5 \exp\left(-5.72 \times 10^{-3} p d \frac{293}{T}\right) \right. \\ & + 52 \exp\left(-1.94 \times 10^{-2} p d \frac{293}{T}\right) \\ & \left. + 116.5 \exp\left(-6.4 \times 10^{-2} p d \frac{293}{T}\right) \right] \end{aligned} \quad (2.4.14)$$

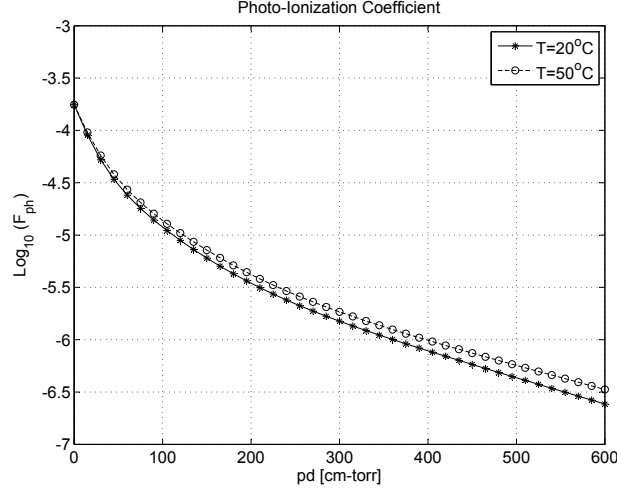


Figure 2.5: Photoionization data in air for $0 \leq pd \leq 600 \text{ cm} \cdot \text{torr}$

It was discussed in [12] that the secondary ionization coefficients depend physically on the conductor material, the surface contamination, composition of the air surrounding the conductor as well as the wavelengths of the photons emitted.

2.4.4 Electron Drift Velocity

Due to its much smaller mass, electrons behave differently to ions when subjected to an electric field. An electron will only lose a small amount of its original kinetic energy after each collision, and the applied field will cause electrons to gain energies much higher than their mean thermal energies. During inelastic collisions, the cross-section due to electron impact still remains a strongly varying function of electron kinetic energy [22], [25]. Several people have measured the electron drift velocity (v_e) as a function of $\frac{E}{p}$, and the empirical data is available in [29], [30], [31], [32] and [33]. The empirical expression adapted for temperature dependency by [25] is given by equation 2.4.15, and is once more shown for air temperature values of $T = 20^\circ\text{C}$ and $T = 50^\circ\text{C}$ in figure 2.6.

$$\frac{v_e(p, T)}{p} = \begin{cases} 1.0 \times 10^6 \left(\frac{E}{p} \frac{T}{293}\right)^{0.715} & \text{for } \frac{E}{p} \leq 100 \frac{\text{V}}{\text{cm}\cdot\text{torr}} \\ 1.55 \times 10^6 \left(\frac{E}{p} \frac{T}{293}\right)^{0.62} & \text{for } \frac{E}{p} > 100 \frac{\text{V}}{\text{cm}\cdot\text{torr}} \end{cases} \quad (2.4.15)$$

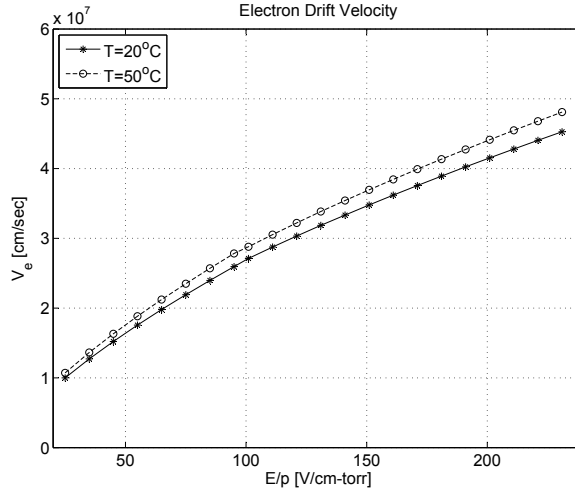


Figure 2.6: Electron drift velocity in air as a function of E/p [$\frac{V}{cm \cdot torr}$]

2.4.5 Electron Diffusion

As seen in section 2.4.4, electrons can gain very high energies because of their small mass. The relationship between the electron drift velocity and electron diffusion is given in equation 2.4.16.

$$D_e = v_e Z_m \frac{kT}{e} \frac{1}{E} \quad (2.4.16)$$

where Z_m is known as the Townsend energy factor, v_e is the electron drift velocity, k is Boltzmann's constant, T is air temperature and e is electron charge. The Townsend energy factor is the ratio of the mean agitation energy of the electrons and the mean molecular energy [22], and is given in [32] as

$$Z_m = 21.0 \left(\frac{E}{p} \right)^{0.49} \quad (2.4.17)$$

The electron diffusion as a function of E/p is shown in figure 2.7.

2.4.6 Ion Diffusion

Diffusion is the movement of molecules from a high to a low concentration, until the concentration in both areas are equal. An approximation for the diffusion coefficient is given in [22] as

$$D = \frac{1}{6} \lambda \bar{v} \quad (2.4.18)$$

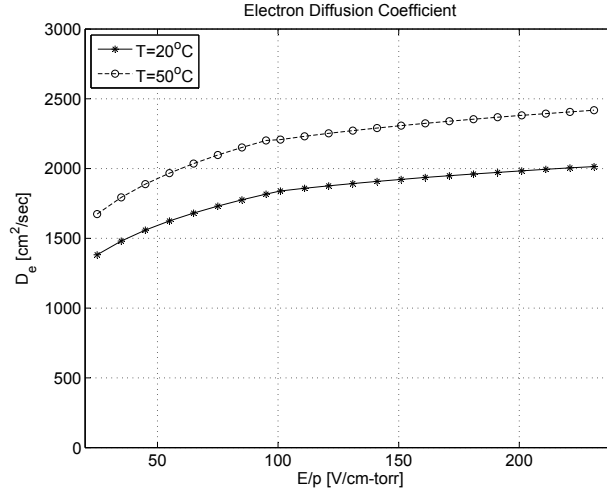


Figure 2.7: Electron diffusion in air as a function of E/p [$\frac{V}{cm \cdot torr}$]

where λ is the mean free path. A free path, λ , is the distance a particle traverses between two successive collisions. It depends on the concentration of the atoms or the density of the gas [22]. The velocity for ions due to diffusion is described in [31] by the diffusivity, D , such that

$$D = 1.29 \times 10^{-2} [cm^2 s^{-1}] \quad (2.4.19)$$

2.4.7 Ion Mobility

From [25] it is seen that the mobility of ions in the drift zone is independent of the field strength when the velocity due to the field is considerably less than the average thermal velocity of air. Extensive work regarding the measurement of the mobility of positive and negative ions in dry air are be found in [30], [31] and [34]. The average mobility value for small ions in dry air at room temperature and atmospheric pressure is taken from [25] as

$$\mu_p = 1.37 [cm^2 V^{-1} s^{-1}] \quad (2.4.20)$$

$$\mu_n = -1.70 [cm^2 V^{-1} s^{-1}]$$

Note that μ_n has a negative sign to indicate that the negative ions drift in the $-\vec{E}$ direction.

2.5 High Voltage Direct Current Conductor Corona

There are different *modes* of corona depending on the polarity, magnitude and type of voltage applied to the conductor. These various corona modes are more observable, and thus better defined, under DC voltage conditions. This is due to the inception conditions remaining constant and the space charge being moved in a constant direction away from the ionization region [9].

2.5.1 Corona Current: Time Domain

In the time domain typical corona current pulses, for time $t \geq 0$, can be written in the form of equation 2.5.1 [35].

$$i(t) = i_p \cdot K \cdot (e^{-\alpha t} - e^{-\beta t}) \quad (2.5.1)$$

In 2.5.1 i_p is the current amplitude in mA and K , α and β are empirical constants. The typical parameters defining corona current pulses are given in [11] and shown in table 2.2.

Corona Discharge Pulse Parameters				
Pulse Type	Amplitude	Rise Time	Duration	Repetition Rate
Positive Corona	10 – 50mA	50ns	250ns	$10^3 - 5 \cdot 10^3$
Negative Corona	1 – 10mA	10ns	100ns	$10^4 - 10^5$

Table 2.2: Pulse parameters for corona discharge currents

A typical *positive corona* pulse can therefore be written as

$$i(t) = i_p \cdot 2.335 \cdot (e^{-0.01t} - e^{-0.0345t}) \quad (2.5.2)$$

while a *negative corona* pulse can be written as

$$i(t) = i_p \cdot 1.3 \cdot (e^{-0.019t} - e^{-0.285t}) \quad (2.5.3)$$

These pulses are shown in figure 2.8 for amplitudes of 20mA and 5mA for positive and negative corona respectively.

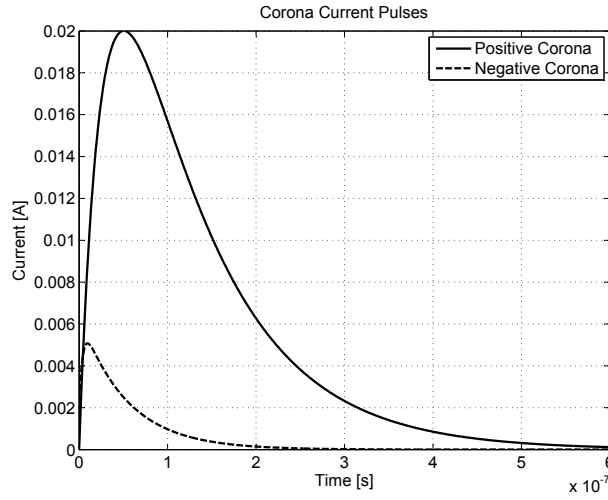


Figure 2.8: Typical positive and negative corona pulses

It is suggested in [36] that when a conductor is positive with respect to ground, electron avalanches move rapidly toward the conductor leaving behind positive ions that drift away. It is due to the rapid movement of the electrons and slower movement of the positive ions that result in the fast rising edge of the positive corona pulse. When the conductor is negative with respect to ground, electron avalanches move away from the conductor and the heavy positive ions move toward the conductor. These ions are now moving in a very high electric field, and their movements are much faster than before. This results in the even faster rising edge of the negative corona pulse.

2.5.2 Corona Current: Frequency Domain

The time domain pulse $f(t)$ and its frequency domain representation $F(\omega)$ are related through the *Fourier transform* in [37] such that

$$F(\omega) = \int_{-\infty}^{+\infty} f(t)e^{-j\omega t} dt \quad (2.5.4)$$

$$f(t) = \frac{1}{2\pi} \int_{-\infty}^{+\infty} F(\omega)e^{j\omega t} d\omega \quad (2.5.5)$$

where $\omega = 2\pi f$ is the angular frequency, f is the frequency, t is time and $j = \sqrt{-1}$. This would imply that, for a corona pulse as defined in 2.5.1, the frequency domain representation is given

by

$$F(\omega) = \int_{-\infty}^{+\infty} i_p \cdot K \cdot [(e^{-\alpha t} - e^{-\beta t})] e^{-j\omega t} dt \quad (2.5.6)$$

The frequency domain representation of the time domain corona current pulses in figure 2.8 is shown in figure 2.9. The amplitude of the frequency spectrum is then determined as

$$|F(\omega)| = i_p \cdot K \cdot \frac{\beta - \alpha}{\sqrt{(\alpha^2 + \omega^2) \cdot (\beta^2 + \omega^2)}} \quad (2.5.7)$$

The highest value of the frequency spectrum is at $\omega = 0$ and is a function of both the amplitude and the pulse duration. Different regions in the frequency domain for $|F(\omega)|$ may be considered as per equations 2.5.8 to 2.5.11 [11].

$$|F(\omega)| = i_p \cdot K \cdot \frac{\beta - \alpha}{\alpha\beta}, \omega \ll \alpha, \beta \quad (2.5.8)$$

$$|F(\omega)| = i_p \cdot K \cdot \frac{\beta - \alpha}{\sqrt{2}\beta\omega}, \omega = \alpha, \omega \ll \beta \quad (2.5.9)$$

$$|F(\omega)| = i_p \cdot K \cdot \frac{\beta - \alpha}{\sqrt{2}\omega^2}, \omega \gg \alpha, \omega = \beta \quad (2.5.10)$$

$$|F(\omega)| = i_p \cdot K \cdot \frac{\beta - \alpha}{\omega^2}, \omega \gg \alpha, \beta \quad (2.5.11)$$

It is observed that the critical frequencies are when ω approaches α and β , thus when $f_\alpha = \frac{\alpha}{2\pi}$ and $f_\beta = \frac{\beta}{2\pi}$. These values for f_α and f_β are shown in table 2.3.

Positive Corona	$f_\alpha = 1.59MHz$	$f_\beta = 5.49MHz$
Negative Corona	$f_\alpha = 3.02MHz$	$f_\beta = 45.36MHz$

Table 2.3: The critical frequencies for different pulse shapes

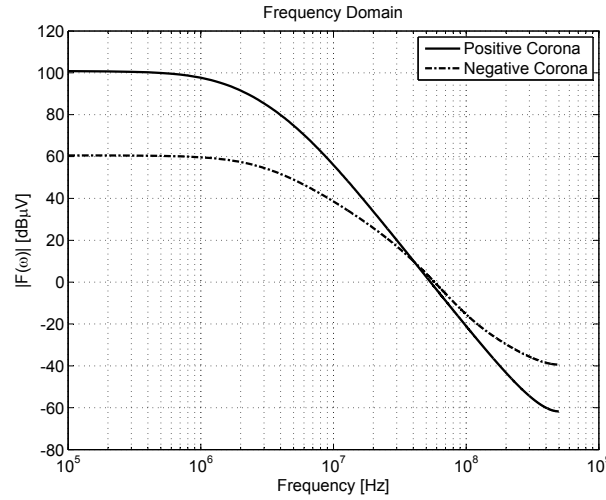


Figure 2.9: Frequency domain data for typical positive and negative corona pulses

It was furthermore identified in [38] that the only measurable radio noise (RN) for alternating current corona in the frequency spectrum of 150kHz to 30MHz is due to onset streamer, positive streamer and negative streamer corona modes.

2.5.3 Positive DC Corona Modes

When a positive polarity is applied to an electrode and the voltage is above the inception level [39], there is an electron avalanche initiated at a point on the boundary surface S_0 which develops towards the anode in a continuously increasing field. This boundary surface S_0 , as shown in figure 2.10, is where $\alpha = \eta$, and is referred to as the *ionization* region (radius r_i). Electrons are accelerated toward the high voltage conductor in this region, and will ionize the neutral air molecules. The increase in charge with the progress of the electrons toward the high voltage conductor in a non-uniform field is given as per equation 2.4.11. During the primary electron avalanche, molecules that are excited release photons that will give rise to secondary avalanche processes [39]. The highest ionization occurs in the close vicinity of the anode conductor (r_c).

Due to lower mobility of ions, positive space charge is left behind along the path of the avalanche development. The majority of the free electrons are absorbed by the anode due to the fact that the electron attachment is less effective than in negative corona because of the high field intensity near the anode [17]. Negative ions are therefore formed mainly in the low field region away from the anode. The positive space charge left behind in the vicinity of the anode will cause an increase of the electric field in the gap [11] as shown in figure 2.11.

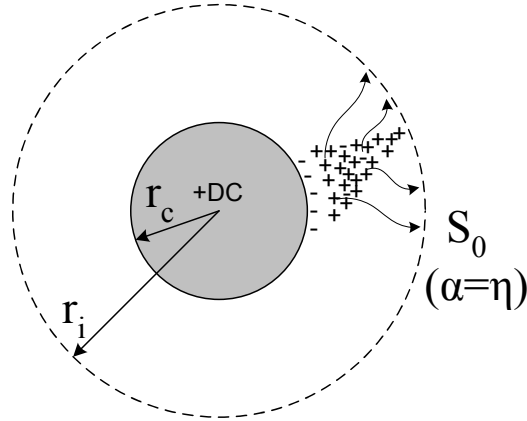


Figure 2.10: Anode avalanche generation leaving behind positive ions

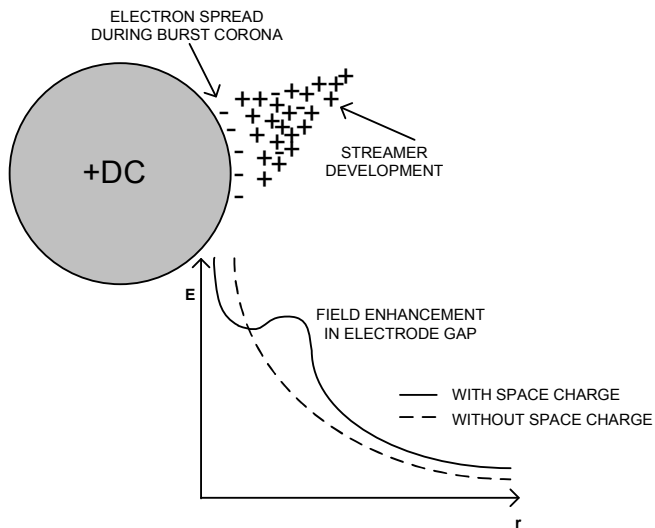


Figure 2.11: Enhancement of E-field in electrode gap due to positive ions

In [17] certain characteristic space charge behaviour was observed. The highly energetic incoming electrons could not immediately be absorbed into the anode. Instead, they tend to first spread out over the anode surface before losing their energy through ionization of the gas particles. It was further noticed that the concentration of positive ions in close proximity to

the anode caused a field enhancement in the electrode gap. Finally, it was noticed that the ionization activity took place well into the low field region outside the normal ionization region. This has been explained by the intense ionization activity in a small volume of gas, referred to as a *corona globule*, that propagates into the low field region due to its own electric field generated by its own positive space charge. It was found in [29] and [40] that the corona globule can contain 10^8 positive ions with a spherical volume of $3 \times 10^{-3} \text{cm}$ in radius, thereby attracting sufficient new electron avalanches a short distance away from it.

It is clear that the space charge development surrounding the anode greatly affects the localised field distribution and thus the development of corona discharge. The corona modes that can be observed as the field intensity is increased are given in [11], [17] and [41] as follows:

2.5.3.1 Burst Corona

The first observable corona discharge mode results from ionization activities at the anode surface. This allows the incoming electrons to lose their energy before they are absorbed by the anode. Positive ions build up cumulatively close to the anode during this process and form positive space charge that suppresses the discharge. The spread of free electrons then move to another part of the anode. The discharge current is small positive pulses that each correspond to the spread of ionization over a small area of the anode. Its suppression is due to the positive space charge produced.

2.5.3.2 Onset Streamer Discharge

The next mode of corona discharge results from the radial development of the discharge. This is a discharge of large amplitude and fairly low repetition. The build up of positive ion space charge enhances the field immediately adjacent to the anode and hence attracts electron avalanches. A radially directed streamer channel develops that results in the onset streamer discharge.

During the development of the onset streamer discharge, a considerable amount of space charge is created in the low field region. The effect of the successive electron avalanches and absorption of the free electrons at the anode results in the formation of residual space charge in front of the anode. The discharges are then suppressed by the electric field close to the anode dropping below the critical value necessary for ionization. There is thus a *dead time* that is necessary for the applied field to remove the residual space charge and restore the conditions for the following streamer formation.

2.5.3.3 Hermstein's Glow: Positive Glow Discharge

In this next mode of positive DC corona, there is a thin luminous layer that forms immediately adjacent to the anode surface where intense ionization activity takes place. The discharge current in this mode is the superposition of, essentially, a direct current with a small pulsating current component (high repetition rate in the hundreds of kHz range).

The positive glow discharge is the result from a particular combination of rate of removal and creation of space charge. The field is of a nature that positive space charge forms quickly and, hence, promotes surface ionization activities, but is low enough not to allow radial streamer or discharge development.

2.5.3.4 Positive Streamer Discharge

The last mode of anode DC corona is such that further increases in applied field causes streamers to form again and leads to a complete breakdown of the gap. The streamer current in this case is much more intense and may have a high repetition rate. The development of the breakdown streamer is directly related to the removal of the space charge by the high field intensity.

2.5.4 Negative DC Corona Modes

A high negative polarity direct voltage is applied to the conductor, thereby forming a non-uniform electric field in the air gap with respect to the plane at ground potential. A boundary S_0 forms two regions in the air gap, where the electric field outside the boundary is not sufficient to maintain effective ionization. The electron avalanches are initiated at the cathode and develop in a continuously decreasing field toward the anode. Referring to figure 2.12, there exists a boundary S_0 where the electron avalanche will stop. The faster moving free electrons in the applied field will concentrate at the tip of the avalanche. This implies that a concentration of positive ions form in the gap between the cathode and boundary S_0 , while the free electrons still move across the gap where they attach themselves to oxygen molecules to form negative ions. These negative ions accumulate in the gap beyond the boundary S_0 because of their low drift velocity, clearly leaving two space charge types in the gap as shown in figure 2.13 [11].

The ion space charge produce a slight increase in the electric field distribution near the cathode and a corresponding decrease near the anode. This implies that the following electron avalanche will develop in a region with a slightly higher field intensity, but extending over a shorter distance

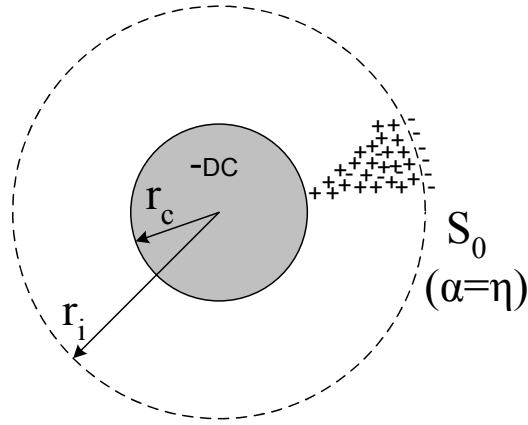


Figure 2.12: Electron avalanche at the cathode

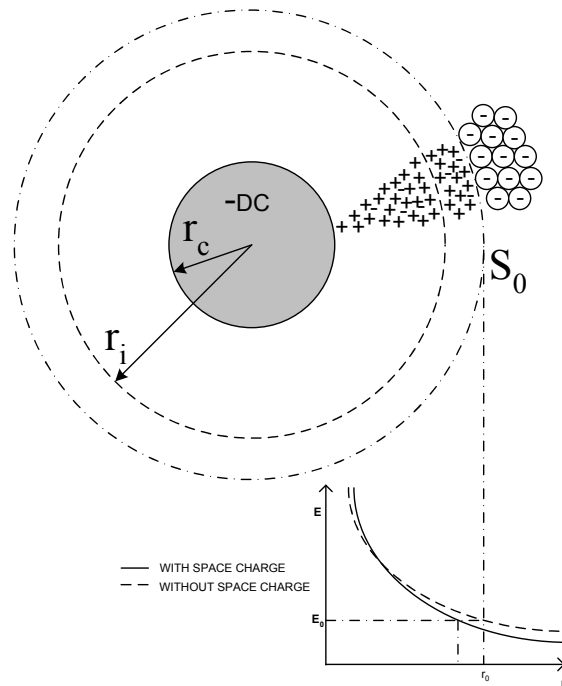


Figure 2.13: Negative ion space charge after electron avalanche

than the previous avalanche. The influence of the space charge is such that it conditions the development of the discharges. This results in three negative corona discharge modes with distinct visual, physical and electrical characteristics discussed in [11] and [17]:

2.5.4.1 Trichel Streamer Discharge

These are the first corona current pulses that can be observed. A streamer is initiated, it develops and then it is suppressed. After a short dead time the cycle is repeated. The duration of an individual streamer is a few hundred nanoseconds, while the dead time varies from a few microseconds to a few milliseconds or longer.

The *pulsative* nature of the discharge is based on the active attachment process to suppress the ionization activity in a short period of time. The repetition rate is a function of the applied field and will increase linearly with the applied voltage. The pulse repetition rate is reduced at high electric fields, however, due to the establishment of a short duration stable discharge regime [11].

2.5.4.2 Negative Pulseless Glow Discharge

With a further increase in the applied voltage the Trichel pulses will, after reaching a critical frequency, change over into the next corona mode called the pulseless glow. In this mode of corona the wandering of the discharge on the cathode surface ceases and it becomes fixed at one point. One can distinguish between a bright spherical glow and a luminous conical positive column stretching outward from the point. The steady corona current produced increases continuously with voltage, until close to breakdown, it changes once again to negative streamers [11].

2.5.4.3 Negative Streamer Discharge

Negative streamers will appear if the applied voltage is increased further still. The glow discharge of the cathode implies that it depends on electron emission from the cathode by ionic bombardment. The streamer is characterised by intensive ionization and shows more effective space charge removal by the applied field [11].

2.6 Corona Generated Space Charge

It is evident from section 2.5 that corona discharges occurring on HVDC transmission lines generate ionic space charge in the gap between the conductors and the ground plane. The polarity of the space charge formed by unipolar lines are the same as that of the conductor, while there is a mixture of positive and negative space charge in the region between bipolar lines [24] as shown in figure 2.14.

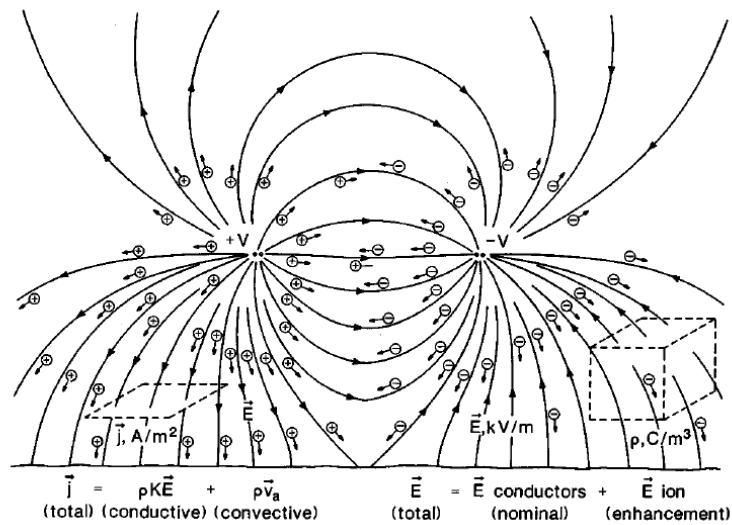


Figure 2.14: A schematic view of the space charge of a typical HVDC bipolar line [42]

It is discussed in [12] that direct current corona can either be pulsating or steady state in nature. Both of these states give rise to corona power loss, but only the pulsating nature gives rise to *radio interference* (RI). The losses on the DC lines result from the continuous average drift of the ion space charge from the conductor in corona, to the earth electrode.

2.6.1 Space Charge Effect on Electric Field

The electric field is not only dependent on the geometry of the electrodes, but also on the space charge build-up in the vicinity of the high voltage conductors. It was found in [43] that large densities of ion space charge were measured and observed up to hundreds of meters away from the HVDC transmission line. Variable and high level measurements were made downwind from the conductor, while relatively stable measurements were made upwind. From [25] and [44] the total electric field (\vec{E}_{tot}) at any point in the electrode gap with a high enough surface voltage

gradient to initiate corona activity, is the superposition of the space charge free (\vec{E}_{sf}) and space charge fields (\vec{E}_{sc}) at that point, as in equation 2.6.1.

$$\vec{E}_{tot} = \vec{E}_{sf} + \vec{E}_{sc} \quad (2.6.1)$$

This is similar to the applied and space charge components discussed in [45]. The ions will drift away from the conductor due to the electric field force vectors. This *drifting* effect (characterised by *ion mobility*) of the space charge will have an *induction* effect on objects. Corona events are the main source of induction when considering steady DC voltages, as the capacitive coupling is negligible. This is contrary to AC voltages where induction is predominantly due to capacitive coupling, and induction due to corona effects are negligible [46].

The ions of opposite polarity of the conductor will be drawn toward and neutralised on the conductor. This implies that a positive conductor will be a source of positive ions, while a negative conductor will be a source of negative ions. The space charge created during corona processes, as seen in equation 2.6.1, also changes the electric field distribution itself. The ions in air are due to *oxygen* and *nitrogen* molecules, which may combine with water molecules in air to form heavier clusters with a lower mobility. *Aerosols* (airborne solid particles) in the atmosphere may also be charged in this ionized field produced by the corona and will have mobilities of two or three orders of magnitude smaller than those of ions. The *heavy ions*, or *charged aerosols*, will significantly influence characteristics of the ionized DC field.

2.6.2 Currents due to Space Charge Effect

The total current due to space charge created during corona processes will have *displacement* and *conduction* current components. The displacement current component is due to the induction effect and change in electric field due to the ions drifting away from the conductor, and is given by equation 2.6.2.

$$\frac{d\vec{D}}{dt} = \epsilon_0 \frac{d\vec{E}}{dt} \quad (2.6.2)$$

The conduction current component is due to space charge neutralising on the conductor, and is given by

$$\vec{J}(t) = |e|n\mu\vec{E}(t) \quad (2.6.3)$$

where e is the electron charge, n is the number density, μ is the mobility and \vec{E} is the electric field vector. The total current, integrated over some surface area S , is therefore given as per equation 2.6.4.

$$i_{tot} = \int_S [J(t) + \epsilon_0 \frac{dE(t)}{dt}] \cdot dS \quad (2.6.4)$$

2.7 Environmental Effects on DC Corona

Factors that influence a highly stressed conductor's susceptibility to the generation of corona does not only include the conductor's surface condition, age and number in a conductor bundle, but also environmental effects like temperature, wind speed and direction, humidity and air pressure [47]. It was also found in [24] that corona generation processes and ionized fields are greatly influenced by atmospheric and weather conditions, especially wind speed and direction that influences the movement of ions. Although the majority of these effects were investigated in [2], some additional environmental effects are discussed here.

2.7.1 Particle Deposition

The deposition of airborne particles and other pollutants will occur when they are in close proximity to, and in high concentration around, a conductor. This will increase the conductor surface irregularity, and hence decrease the roughness factor in equation 2.1.1. This in turn will increase the conductor surface voltage gradient, and hence increase the conductor's susceptibility to corona generation [47]. Depositions not only include dust particles and pollutants, but, especially in the case of positive pole DC conductors, also include insects that are drawn to the conductor to form small corona sources. This observation was made in [48] and [49].

2.7.2 Weather Conditions

For the case of AC corona, there can be an increase in radio interference (RI) level of up to $25dB$ between dry and heavy rain conditions. The RI generated by DC conductor corona, on the other hand, reduces under rain conditions [50]. Under DC fields the water droplets adopt

a shape that causes stable glow corona modes, such that the worst case corona performance is not related to foul weather conditions [15]. This, however, is not the case for the DC corona loss (CL) which is higher under rain conditions [51].

2.7.3 Altitude, Air Pressure and Humidity

It is well known that temperature and humidity can affect the breakdown threshold of air. These effects on AC corona were discussed in [52], while the effects on AC and DC corona inception voltages were discussed in [53]. It was noted that the corona inception voltage for positive DC at a high relative humidity and low air pressure increased, while the AC inception voltage for these conditions decreased. At high levels of humidity water condenses and forms small drops on the conductor surface. Under high humidity conditions, molecular ions also tend to form clusters with water molecules in the air, thereby giving rise to heavy ions with low mobilities. Heavy ions and charged particles around high voltage conductors have a significant influence on the space charge field surrounding these conductors [47]. It was also found in [54] that the net effect of the presence of water vapour would be to raise the value of E/p at which the attachment equals the ionization.

When considering the corona performance of a line, it is suggested in [55] that an altitude correction factor for both altitude and frequency related to the relative air density, should be added to the generation function. The altitude correction factor, RI_{cf} , is given by

$$RI_{cf} = H/300dB \quad (2.7.1)$$

where H is the height above sea level in m. This is similar to the altitude correction factor for AC RI levels given in [11] and [56].

Another altitude correction factor, RI_{cf} , was presented in [57] and is given by equation 2.7.2

$$RI_{cf} = k(H/1000 - 1) \quad (2.7.2)$$

where k is a constant between $k = 3.3$ and $k = 6.5$, and H is the height above sea level in m for $H \geq 1000m$.

Chapter 3

Particle-In-Cell Simulation

3.1 Introduction

The complex nature of problems encountered in plasma physics has been the driving force behind the development of various computer simulation techniques and numerical codes. These codes primarily focus on the areas of kinetics and fluid description. Particle simulation computes the motion of a collection of particles interacting with each other, as well as with externally applied fields [58]. It was shown in [25] that high voltage direct current (HVDC) corona can be described by a system of generic interpenetrating fluids which include electrons, positive and negative ions, as well as neutrals such as air molecules. For simplicity, only typical fluids of positive and negative ions are considered. The observation of the changes in fluid properties as time progresses is known as the *Eulerian* approach. The particle-in-cell model discussed in the dissertation, however, will focus the attention on the given simulation particles as they move through the flow. This method is called the *Lagrangian* viewpoint of fluid mechanics, which is a natural extension of particle mechanics.

Particle-in-cell (PIC) is defined in [58] and [59] as using a particle as a point charge that is assigned by linear interpolation to the nearest grid points. This chapter will investigate the use of a two-dimensional particle-in-cell (2D PIC) simulation to study the monopolar HVDC corona problem for various geometries. The simulation particles in this 2D PIC model are assumed to be linear charge densities. Techniques described in this chapter should be compared to the work done in [25], [60] and [61] by Bai-Lin Qin *et al.* This chapter will furthermore investigate not only the use of linear interpolation functions, but also the use of higher order interpolation functions for assignments to grid points in the PIC simulation. This will lead to

a more accurate solution of the Poisson space charge field equation.

Some of the other numerical studies of corona current behavior in cylindrical arrangements include the use of the *flux corrected transport* (FCT) method in [62] and [63], as well as the *particle-mesh* method used in [64]. The application of the *finite element method* (FEM) for monopolar corona on bundle conductors is discussed in [65].

3.2 Continuity Equations and Momentum Conservation

3.2.1 Fluid Continuity Equation

The conservation of matter requires that the total number of particles N in a volume V can only change if there is a net flux of particles across the surface S bounding the volume [16]. Considering the particle flux density as $n\vec{v}$, we then have by Stokes' theorem that

$$\frac{\partial N}{\partial t} = \int_V \frac{\partial n}{\partial t} dV = - \oint n\vec{v} \cdot dS = - \int_V \nabla \cdot (n\vec{v}) dV \quad (3.2.1)$$

Seeing that this must hold for any volume V , the integrands must be equal such that

$$\frac{\partial n}{\partial t} + \nabla \cdot (n\vec{v}) = 0 \quad (3.2.2)$$

In equations 3.2.1 and 3.2.2, \vec{v} is the particle velocity and n is the number density in *number per cm³*. There is one such *equation of continuity* for each of the particle species (electrons, positive ions, negative ions). The sources and sinks of these particles are to be added to the right-hand side of these equations. The *fluid equation of motion* for any species including collisions is given in [16] by

$$mn \frac{d\vec{v}}{dt} = mn \left[\frac{\partial \vec{v}}{\partial t} + (\vec{v} \cdot \nabla) \vec{v} \right] = \pm en \vec{E} - \nabla p - mn v_c \vec{v} \quad (3.2.3)$$

with v_c being the collision frequency, which, according to [16] must be assumed a constant in order for this equation to be useful. The \pm sign indicates the sign of the charge, e , while m is the particle mass and p is the pressure.

The collision frequency is given by

$$v_c = N\sigma_c\bar{v} \quad (3.2.4)$$

where N is the volume density of the background medium (neutral atoms per cm^3) and σ_c is the effective collision cross-sectional area of the particle with velocity \bar{v} . A steady state in which $\frac{\partial\bar{v}}{\partial t} = 0$ is considered. For a sufficiently small \bar{v} (or sufficiently large v_c) a fluid element will not move into the regions of different \vec{E} and ∇p in a collision time (the convective derivative $\frac{d\bar{v}}{dt}$ will also vanish). The *convective derivative* is defined in [16] as

$$\frac{d\bar{v}}{dt} = \frac{\partial\bar{v}}{\partial t} + (\bar{v} \cdot \nabla)\bar{v} \quad (3.2.5)$$

where ∇ is the gradient operator, \bar{v} is velocity and $\frac{\partial}{\partial t}$ is the partial derivative with respect to time. Setting the left-hand side of equation 3.2.3 equal to zero we have for an isothermal plasma (also discussed as the *particle flow vector* $\Gamma = n\bar{v}$ in [11] and [59]):

$$\bar{v} = \mu\vec{E} - D\frac{\nabla n}{n} \quad (3.2.6)$$

with mobility

$$\mu \equiv \frac{|q|}{mv_c} \quad (3.2.7)$$

and diffusion constant

$$D \equiv \frac{KT}{mv_c} \quad (3.2.8)$$

The transport coefficients μ and D are connected by the *Einstein relation* in equation 3.2.9

$$\mu = |q|\frac{D}{KT} \quad (3.2.9)$$

with q the charge and K and T being *Boltzmann's constant* and *absolute temperature* respectively.

The *electron fluid* is therefore described by the *continuity equation*

$$\frac{\partial n_e}{\partial t} + \nabla \cdot (n_e \vec{v}_e) = G_e - L_e \quad (3.2.10)$$

where n_e is the number density, \vec{v}_e is the fluid velocity, G_e represents the electron sources and L_e the electron sinks. G_e in this continuity equation results from processes such as electron impact ionization, photoionization and also detachment of electrons from negative ions. Similarly, L_e result from processes such as recombination with positive ions and attachment to neutral particles. The *positive ion fluid* is described by the *continuity equation*

$$\frac{\partial n_p}{\partial t} + \nabla \cdot (n_p \vec{v}_p) = G_p - L_p \quad (3.2.11)$$

where G_p represents the positive ion source that results from processes such as electron impact ionization and photoionization. The positive ion sinks that result from processes such as recombination with electrons and negative ions are given by L_p . The *negative ion fluid* is described by the *continuity equation*

$$\frac{\partial n_n}{\partial t} + \nabla \cdot (n_n \vec{v}_n) = G_n - L_n \quad (3.2.12)$$

where negative ion sources G_n are as a result of attachments and sinks, while L_n are as a result of recombination with positive ions.

3.2.2 Fluid Momentum Conservation

From equation 3.2.6 the *momentum conservation* for *positive ion fluid* is modelled by

$$\vec{v}_p = \mu_p \vec{E} - D_p \frac{\nabla n_p}{n_p} \quad (3.2.13)$$

with μ_p and D_p the positive ion mobility and positive ion diffusion coefficients respectively. *Momentum conservation* for *negative ion fluid* (which also applies to electrons) is modelled by

$$\vec{v}_n = \mu_n \vec{E} - D_n \frac{\nabla n_n}{n_n} \quad (3.2.14)$$

It should be noted that μ_n has a negative sign so that the negative ions drift in the $-\vec{E}$ direction. The electric field in the momentum equations is given by Gauss's Law such that

$$\nabla \cdot \vec{E} = \frac{1}{\epsilon_0}(n_p q_p + n_e q_e + n_n q_n) \quad (3.2.15)$$

where $q_e = -|e|$ is electron charge, $q_p = +|e|$ is positive ion charge and $q_n = -|e|$ is negative ion charge. Seeing that the focus of the research in this dissertation is that of HVDC, the electric field is electrostatic such that

$$\vec{E} = -\nabla\phi \quad (3.2.16)$$

This PIC model will follow *simulation particles*, of which one represents many actual particles, and calculate the associated electric field that determines their motion.

3.3 PIC Simulation Model

The rule for the dynamics of particles is given by the *equation of motion* in 3.3.1.

$$\frac{d\vec{x}_i}{dt} = \vec{v}_i \quad (3.3.1)$$

In equation 3.3.1, \vec{x}_i is the position and \vec{v}_i is the velocity of simulation particle i respectively. These simulation particles can be elements of electron, positive ion and negative ion fluid. Similar to equations 3.2.13 and 3.2.14, the velocity \vec{v}_i at the particle location is related to the field quantity at the location, and the momentum conservation derived from the *Boltzmann* equation for ions provide that

$$\vec{v}_i = \mu_i \vec{E} - D_i \frac{\nabla n_i}{n_i} \quad (3.3.2)$$

It was found in [25] that when the charge and position of all the simulation particles are known, the number density can be determined without directly solving the continuity equations. The governing equations for the PIC simulation model is completed by the field equation. This is

discussed in section 3.4.

3.4 Field Equations

Given the potentials on the boundaries and the space charge within this region of simulation, the potential distributions are completely specified by Poisson's equation such that

$$\nabla^2\phi = -\frac{|e|}{\epsilon_0}(n_p - n_e - n_n) \quad (3.4.1)$$

where $|e|$ is the charge magnitude, n_p , n_e and n_n are the positive ion, electron and negative ion number densities, ϵ_0 is the permittivity of free space. The total potential ϕ is taken as the superposition of the *space charge free* potential (ϕ_{sf}) and the *space charge* potential (ϕ_{sc}) as per equation 3.4.2.

$$\phi = \phi_{sf} + \phi_{sc} \quad (3.4.2)$$

The space charge free solution is due to the applied voltage and geometry, while the space charge solution is due to the space charge only. Due to the fast rate of change of ϕ close to the conductor, the first order finite element method may result in large numerical errors. It is for this reason that the *Laplacian* space charge free problem is solved using the *charge simulation method* (CSM), while the *Poissonian* space charge problem is solved using the *finite element method* (FEM). The CSM and FEM are discussed in sections 3.6 and 3.8 respectively.

Space Charge Free Solution	Space Charge Solution
$\nabla^2\phi_{sf} = 0$	$\nabla^2\phi_{sc} = \frac{- e (n_p - n_e - n_n)}{\epsilon_0}$
$\phi_{sf} _{conductor} = \pm V$	$\phi_{sc} _{conductor} = 0$
$\phi_{sf} _{sheath} = 0$	$\phi_{sc} _{sheath} = 0$

Table 3.1: Set of equations defining computational field solution problem

In summary, the problem is defined by the set of equations in table 3.1. The calculation

of electric fields therefore depends on the solution of Laplace's and Poisson's equations with certain boundary conditions satisfied. This can be achieved by either analytical or numerical computation. The physical systems, however, are often complex and the analytical solutions are difficult or even impossible. It is for this reason that numerical methods are used in these types of engineering applications [66].

3.5 Conduction and Displacement Current

The total current flowing to and experienced on the surface area (S) of the electrodes per unit length is given by equation 3.5.1

$$i(t) = \int_S (\vec{J} + \epsilon_0 \frac{d\vec{E}}{dt}) \cdot d\vec{S} \quad (3.5.1)$$

where \vec{J} is the *conduction current density* component given by

$$\vec{J} = |e|(n_p \vec{v}_p - n_e \vec{v}_e - n_n \vec{v}_n) \quad (3.5.2)$$

and $\epsilon_0 \frac{d\vec{E}}{dt} = \frac{d\vec{D}}{dt}$ is the *displacement current density* component approximated by

$$\frac{d\vec{D}}{dt} = \frac{\epsilon_0}{\Delta t} (\vec{E}(t) - \vec{E}(t - \Delta t)) \quad (3.5.3)$$

The total current flowing to the electrode per unit length can therefore be determined by

$$i_{tot}(t) = \sum_{k=1}^{N_m} [\vec{J}(t) + \epsilon_0 \frac{d\vec{E}(t)}{dt}]_k \cdot \hat{n}_k L_k \quad (3.5.4)$$

where $m = a, c$ or s represents the anode, cathode or sheath respectively, N_a , N_c and N_s are the number of boundary node points on the anode, cathode and sheath respectively, \hat{n}_k is the unit vector normal to the electrode surface at node point k , L_k is the distance between the boundary node point (k) and ($k + 1$) [25].

3.6 Charge Simulation Method

The charge simulation method (CSM) is a numerical method used for the computation of electrostatic fields. This method is based on the use of fictitious line charges as particular solutions of Laplace's and Poisson's equations [66]. The CSM has been found to be a very competitive and often superior computational method to that of the finite element method (FEM) and finite difference method (FDM), particularly when accuracies within highly divergent fields are required [21]. The basic principle of operation is based on replacing the distributed charges on the surface of the conductor, with N fictitious line charges Q_j inside the conductor. Their image charges Q'_j with respect to a ground plane is set as in figure 3.1.

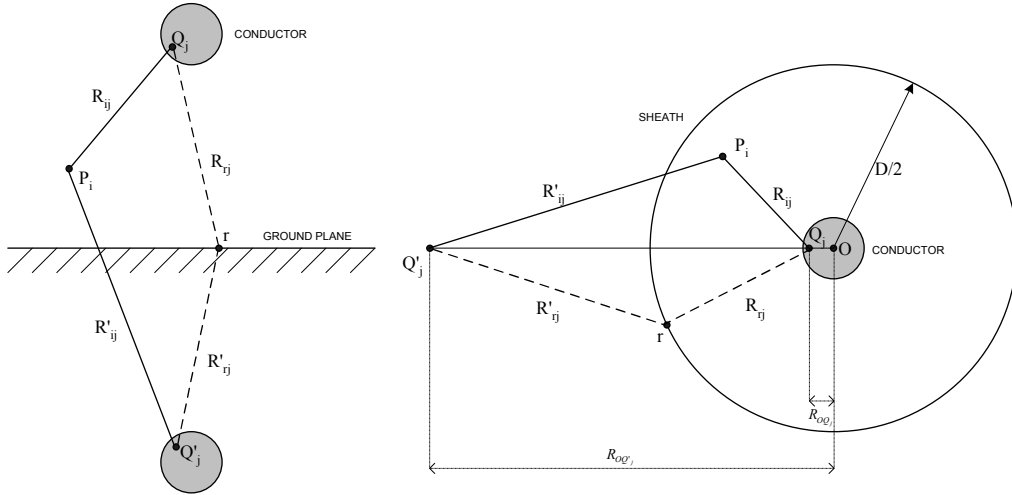


Figure 3.1: Conductor above ground plane and conductor in cylinder for CSM solution

In order to calculate the magnitude of these charges it is required that the electrostatic potential ϕ_i , at point P_i , be equal to the conductor potential ϕ_c resulting from superposition of all the individual line charges as per equation 3.6.1.

$$\phi_c = \phi_i = \sum_{j=1}^N P_{ij} Q_j \quad (3.6.1)$$

In equation 3.6.1 P_{ij} is given by

$$P_{ij} = \frac{1}{2\pi\epsilon_0} \ln\left(\frac{R_{rj}}{R_{ij}} \cdot \frac{R'_{ij}}{R'_{rj}}\right) \quad (3.6.2)$$

such that R_{ij} and R_{rj} are the distances from the charge Q_j to a point P_i and ground reference point r respectively, while R'_{ij} and R'_{rj} are the distances from the image charge Q'_j to a point P_i and ground reference point r respectively. The charges are calculated by choosing N contour points on the surface of the high voltage conductor. The application of equation 3.6.1 to the N contour points then leads to a system of N linear equations for the N charges such that

$$[P] \cdot [Q] = [V] \quad (3.6.3)$$

The electric field at a point P_i can therefore be calculated as

$$\vec{E}_i = -\nabla\phi_i = \left[-\sum_{j=1}^N \frac{\partial P_{ij}}{\partial x} Q_j\right]\hat{x} + \left[-\sum_{j=1}^N \frac{\partial P_{ij}}{\partial y} Q_j\right]\hat{y} \quad (3.6.4)$$

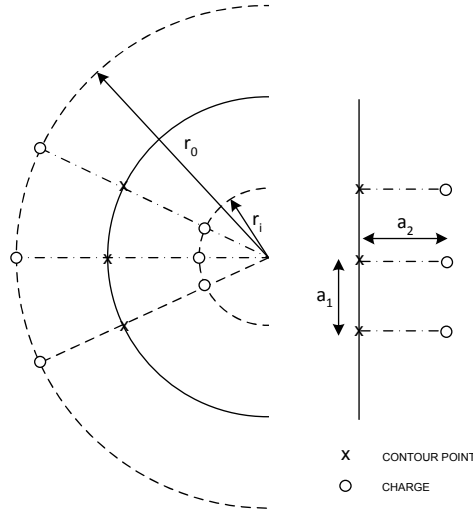


Figure 3.2: The assignment factor for charge and contour placement in convex and concave curvature

For the most effective application of this method, the question of a suitable arrangement of charges and contour points is of importance. A practical criterion is obtained in [66] by the definition of an assignment factor, such that $f_a = a_2/a_1$ with the distance a_1 between two successive contour points and the distance a_2 between a contour point and the corresponding charge, as in figure 3.2. In the case of curved contours the formulation of a curvature criterion (radius r) based on the geometric mean of a_1 and a_2 were derived such that

$$r_{o/i} = r \cdot \left[\sqrt{1 + \left(f_a \cdot \frac{a_1}{r} \right)^2} \pm f_a \cdot \frac{a_1}{r} \right] \quad (3.6.5)$$

where r_o is valid for *convex* curvature and r_i is valid for *concave* curvature.

3.7 Domain Discretization (Meshing)

The discretization of the simulation region is when the domain (Ω) is subdivided into a number of subdomains or elements (Ω^e), as in figure 3.3 [67].

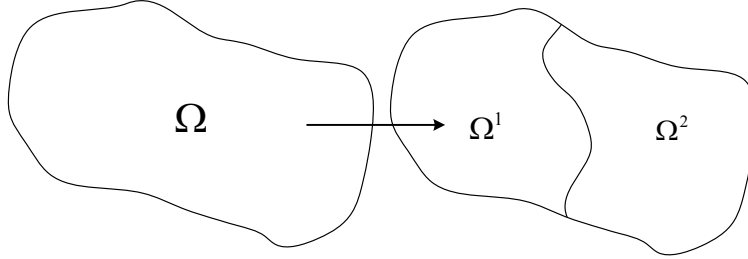


Figure 3.3: Discretization of domain Ω into smaller elements Ω^e where $e = 1, 2$

For the two dimensional simulation area, the domain is typically subdivided into triangular elements. Because the field is highly divergent close to the conductor, a higher resolution mesh is required in this area. It is for this reason that the potential contours and their intersections with electric flux lines of the space charge free result were used to generate the mesh of triangles. An example of the meshing of a cylindrical corona cage using this technique is shown in figure 3.4 for a conductor in the centre of the cage (monopolar tests) and figure 3.5 for a conductor offset to the side of the cage (bipolar tests).

3.8 Finite Element Method

The finite element method (FEM) is a numerical method used to solve *boundary-value problems* [67]. First order triangular finite elements first made their appearance in electrical engineering applications in 1968, where they were used to solve simple waveguide problems. They have since been used to solve two dimensional scalar potential and wave functions [59], [68]. Because

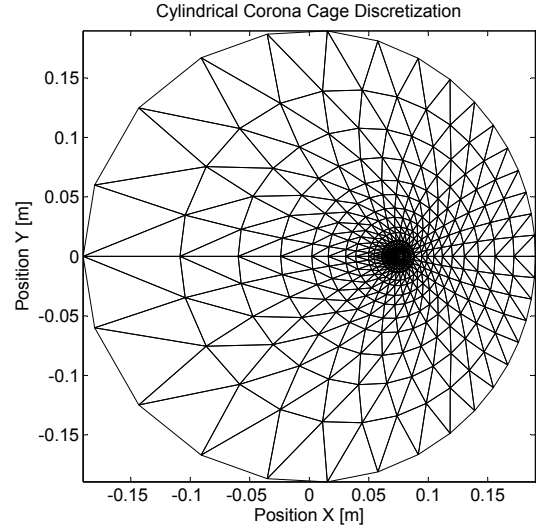
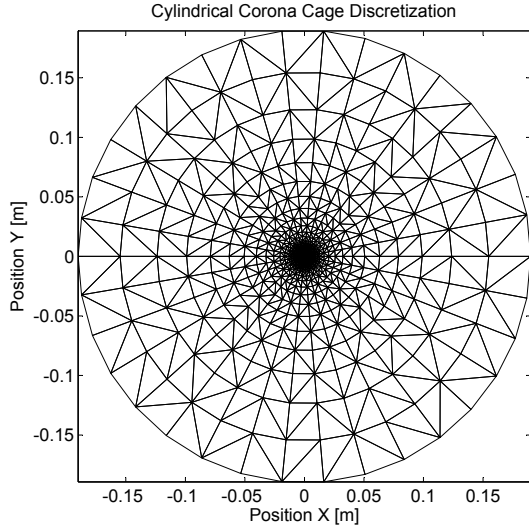


Figure 3.4: Meshing of conductor in centre of cage **Figure 3.5:** Meshing of conductor offset in cage

of the relatively low level of accuracy, the first order elements have been replaced in many applications by *higher order elements*.

The principle of this method is to subdivide a continuous domain into a number of subdomains in which an unknown function is represented by *interpolation functions* with unknown coefficients. A *system of algebraic equations* is obtained by applying either the Ritz variational or Galerkin weighted residual procedure [69], [70]. The solution to the boundary value problem is achieved by solving the system of equations while adhering to certain boundary conditions [67]. When a value ϕ is specified on a boundary, this is called the *Dirichlet* boundary condition, while when the value of a normal derivation is specified on a boundary, this is known as the *Neumann* boundary condition. The boundary value problem in this dissertation (equation 3.4.1) is solved using the variational approach, where the differential equations are represented as *functionals*. It is shown in [68] and [69] that the variational functional for the Poisson equation is given by

$$W(\phi_{sc}) = \frac{1}{2} \int_{\Omega} (\nabla \phi_{sc} \cdot \nabla \phi_{sc}) dS - \int_{\Omega} (g \phi_{sc}) dS \quad (3.8.1)$$

where $g(x, y) = \frac{\rho}{\epsilon} = \frac{|e|(n_p - n_e - n_n)}{\epsilon_0}$.

3.8.1 First Order Elements

First order elements are when the domain Ω is subdivided into a number of elements e that are usually linear three node triangular elements as in figure 3.6.

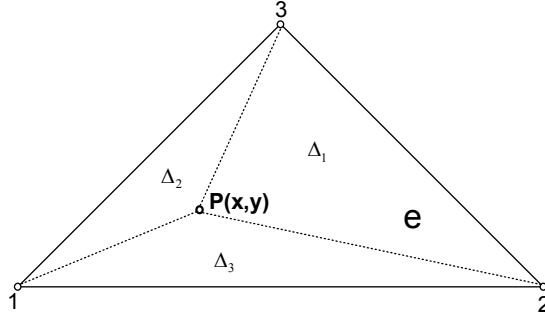


Figure 3.6: Linear three node triangular finite element e

The approximation function for these first order elements is given by

$$\phi_e = a_e + b_e x + c_e y \quad (3.8.2)$$

where a_e , b_e and c_e are the constants in the element e that the FEM is to compute. It is more convenient, however, to write the approximation function in terms of the unknown potentials at the three nodes [69] such that

$$\phi_{sc}^e = \alpha_1(x, y)\phi_1 + \alpha_2(x, y)\phi_2 + \alpha_3(x, y)\phi_3 = \sum_{i=1}^3 \alpha_i(x, y)\phi_i \quad (3.8.3)$$

where ϕ_{sc}^e potential solution due to the space charge in element e , ϕ_i is the scalar potential at node i and α_i is the *linear basis function*. The basis function α_i is defined such that it has the value 1 at node i and 0 everywhere else. The linear interpolation function in an element is given by

$$\alpha_i^e(x, y) = \frac{1}{2\Delta^e} (a_i^e + b_i^e x + c_i^e y) \quad (3.8.4)$$

while the area of the triangle, Δ^e , is given by equation 3.8.5.

$$\Delta^e = \frac{1}{2} \begin{vmatrix} 1 & x_1^e & y_1^e \\ 1 & x_2^e & y_2^e \\ 1 & x_3^e & y_3^e \end{vmatrix} = \frac{1}{2}(b_1^e c_2^e - b_2^e c_1^e) \quad (3.8.5)$$

The energy functional of an element e is given by equation 3.8.6.

$$W_e = \frac{1}{2} \int_e [(\nabla \phi_{sc} \cdot \nabla \phi_{sc}) - g \phi_{sc}] dS \quad (3.8.6)$$

The energy term is then manipulated by substituting 3.8.3 into 3.8.6, thereby giving:

$$W_e = \frac{1}{2} \sum_{i=1}^3 \sum_{j=1}^3 \phi_i \left[\int_e (\nabla \alpha_i \cdot \nabla \alpha_j) dS \right] \phi_j - \sum_{j=1}^3 \int_e g_0 (\alpha_j \phi_j) dS \quad (3.8.7)$$

From [69] it seen that this can be written compactly in matrix notation as

$$W_e = \frac{1}{2} \{\phi\}_e^T [S_e] \{\phi\}_e - \{\phi\}_e^T \{T_e\} \quad (3.8.8)$$

with

$$S_{ij}^e = \int_e (\nabla \alpha_i) \cdot (\nabla \alpha_j) dS \quad (3.8.9)$$

and

$$T_j^e = \int_e g_0 \alpha_j dS \quad (3.8.10)$$

In 3.8.10 $g = g_0$ is a constant within each element. The boundary conditions at the edge between two adjacent elements are continuous, and the functional for the whole domain Ω can therefore be written as

$$W = \sum_e W_e = \frac{1}{2} \{\phi\}^T [S] \{\phi\} - \{\phi\}^T \{T\} \quad (3.8.11)$$

where the entries in the $\{\phi\}$ vector are the approximate values of $\phi(x, y)$ at all the nodes, and the entries in the global matrices S and $\{T\}$ can be found by the summation of all individual

element matrices S_e and $\{T_e\}$ respectively. The solution to the partial differential equation (PDE) is the minimum of the energy functional such that

$$\frac{\partial W\{\phi\}}{\partial\{\phi\}^T} = \{0\} \quad (3.8.12)$$

which implies that the discretized algebraic equation is derived to be

$$[S]\{\phi\} = \{T\} \quad (3.8.13)$$

3.8.2 First Order Weighting

From the simulation particle position *weighting* is applied to the surrounding grid or mesh points in order to calculate the potential and field at these points. For scattered particles in the various elements *interpolation* functions can be used to calculate the force acting in on a particle, due to the field at the grid points, by again applying weighting [58]. Therefore, to complete the discrete model, prescriptions for obtaining mesh-defined quantities from particle positions and for obtaining quantities at particle positions from nearby mesh points are required.

The weighting assignment can be *zero*, *first* or *higher* order. Zero order assignment to one nearest grid point is simplest, but leads to noise in fields. Higher order weighting on the other hand is mathematically accurate and smooth, although it involves more computation. The work by [25] made use of first order assignment, while the work discussed in this dissertation makes use of higher (second) order assignment. In the case of charge assignment in a linear triangular element, weighted areas are assigned to the nearby mesh points, i.e. Δ_1 to mesh point 1, Δ_2 to mesh point 2 and Δ_3 to mesh point 3 as in figure 3.6. Assigning a particle Q_p , at a point $P(x, y)$ inside a triangular element e , to the mesh points $i(x_i, y_i)$, $j(x_j, y_j)$ and $k(x_k, y_k)$, it can be shown that

$$Q_i(x_i, y_i) = \lambda_i^e(x_p, y_p)Q_p$$

$$Q_j(x_j, y_j) = \lambda_j^e(x_p, y_p)Q_p \quad (3.8.14)$$

$$Q_k(x_k, y_k) = \lambda_k^e(x_p, y_p)Q_p$$

with

$$\begin{aligned}\lambda_i^e(x, y) &= \frac{a_i^e + b_i^e x + c_i^e y}{2\Delta} \\ \lambda_j^e(x, y) &= \frac{a_j^e + b_j^e x + c_j^e y}{2\Delta} \\ \lambda_k^e(x, y) &= \frac{a_k^e + b_k^e x + c_k^e y}{2\Delta}\end{aligned}\tag{3.8.15}$$

where Δ is the area of the element as defined previously in equation 3.8.5. In the case where the electric field at the mesh points are known as \vec{E}_i , \vec{E}_j and \vec{E}_k , the interpolation function to the point $P(x, y)$ can then be defined as

$$\vec{E}_p = \vec{E}_i \lambda_i(x_p, y_p) + \vec{E}_j \lambda_j(x_p, y_p) + \vec{E}_k \lambda_k(x_p, y_p)\tag{3.8.16}$$

3.8.3 Higher Order Elements

In order to improve the accuracy of the finite element solution, one can either refine the subdivision and work with smaller elements, or one can use higher order interpolation functions. For the computational work discussed in this dissertation, *quadratic* triangular elements or second order interpolation functions were implemented. Quadratic triangular elements have six nodes, one at each of its three vertices and one in each of the middles of its three sides, as shown in figure 3.7.

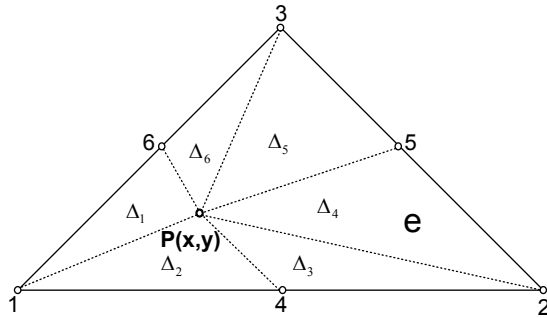


Figure 3.7: Quadratic six node triangular finite element e

Within each element, the unknown function ϕ is now approximated by

$$\phi_e(x, y) = a_e + b_e x + c_e y + d_e x^2 + e_e xy + f_e y^2 \quad (3.8.17)$$

where a_e, b_e, c_e, d_e, e_e and f_e are the constants in the element e that the FEM is to compute. Again this approximation function can rather be written in terms of unknown potentials at the various node points such that

$$\phi_{sc}^e = \sum_{i=1}^6 \alpha_i^e(x, y) \phi_i^e \quad (3.8.18)$$

The interpolation functions for the quadratic elements, provided that they are numbered as in figure 3.7, are given in [67] as

$$\alpha_i^e(x, y) = (2L_i^e - 1)L_i^e \quad i=1,2,3 \quad (3.8.19)$$

$$\alpha_4^e(x, y) = 4L_1^e L_2^e, \quad \alpha_5^e(x, y) = 4L_2^e L_3^e, \quad \alpha_6^e(x, y) = 4L_3^e L_1^e$$

In the above equation L_i^e is given by

$$L_i^e(x, y) = \frac{1}{2\Delta^e} (a_i^e + b_i^e x + c_i^e y) \quad i=1,2,3 \quad (3.8.20)$$

with a_i^e, b_i^e, c_i^e and Δ^e being the same as in equation 3.8.4. The quadratic basis functions, as in the case of the linear basis functions, again have the property

$$\alpha_i^e(x_k^e, y_k^e) = \delta_{ik} = \begin{cases} 1 & i = k \\ 0 & i \neq k \end{cases} \quad (3.8.21)$$

3.9 Time Integration: Linear Multistep Method

The equation of motion for the simulation particles can be written as

$$\frac{d\vec{x}}{dt} = \vec{v}(x, t) \quad (3.9.1)$$

where $\vec{v}(x, t)$ is the velocity given by equation 3.9.2.

$$\vec{v}(x, t) = \mu \vec{E}(x, t) - D \frac{\nabla n(x, t)}{n(x, t)} \quad (3.9.2)$$

In the above equation, \vec{x} is the position vector of which the length is equal to the total number of simulation particles. The continuous functions of \vec{x} and \vec{v} are replaced by values at discrete time intervals $\{\vec{X}_n\}$ and $\{\vec{V}_n\}$. The discrete approximation is done by the *linear multistep method* (LMM) discussed in [59], [71] and [72]. For the computational code in this dissertation, the simplest form of LMM that involves the least computation, and refers to only one time level, is selected. This is known as the *Euler* scheme [25] and is given by

$$\vec{X}_{n+1} - \vec{X}_n = DT \cdot \vec{V}(X_n, t_n) \quad (3.9.3)$$

The various *numerical stability* criteria and restrictions were investigated in [25], and it was found that the numerical error became large when the simulation particle moves a distance more than one element length in a timestep DT . On the other hand, nothing is gained by allowing a simulation particle to move less than $1/10^{th}$ of an element length.

3.10 Mathematical Model

3.10.1 Positive Streamer Development

During the positive corona processes, avalanches are created by electrons accelerated towards the conductor in the region where $\alpha \geq \eta$. The α and η coefficients are the ionization and attachment coefficients respectively. The positive ions created during the avalanche then moves into the electrode gap, while the electrons neutralise on the conductor surface. If one simulates the charge of the initiatory electrons per unit length as linear line charges densities N_0 , the increase in charge with the progress of the electrons towards the high voltage conductor in a non-uniform field is given as per equation 2.4.11

$$N_1 = N_0 \exp \int_{r_i}^r (\alpha - \eta) dr$$

where r_i is the boundary of the ionization region and r is the conductor radius. The head at the tip of the avalanche is assumed to be spherical and has a radius r_h , given by equation 3.10.1, that increases as the avalanche progresses [39].

$$r_h = \sqrt{6D\tau} \quad (3.10.1)$$

In equation 3.10.1, D is the diffusion coefficient and τ is the lifetime of the avalanche. During the primary electron avalanche, molecules that are excited release photons that will give rise to secondary avalanche processes [39]. For the process of avalanche ionization, the secondary electrons are significant [12], and the theoretical criteria for the onset of positive burst pulse corona was established in [34] by considering photoionization as secondary mechanism. The onset streamers consist of a number of successive generations of electron avalanches which take place in the ionization zone around the conductor [73]. Following the onset of steady positive corona, the conductor surface voltage gradient decreases. The number of electrons photo-emitted is given in [25] and [39] by

$$N_{photo} = \int_{r_i}^r N_1 F_1 p \frac{A_2}{R_d + F_2 \frac{A_2}{\sqrt{A_1}}} dr \quad (3.10.2)$$

where N_{photo} is the number of photoelectrons produced after the first avalanche that will give rise to secondary processes, N_1 is the number of ionizing collisions associated with the first generation, F_1 is the photoionization coefficient determined from experimental data as in section 2.4.3, F_2 is a dimensionless constant evaluated numerically in [23], A_1 is the area of the ionizing source, A_2 is the area where the photoionization is to be calculated, R_d is the distance to be traveled by the photons and p is the air pressure. A schematic depicting the spatial-temporal development of the corona pulse due to these primary and secondary processes was developed in [39] and is shown in figure 3.8.

In this schematic the lifetime of the second generation, τ_2 , is the time required for the second generation charge to reach the positive space charge left behind the first generation with head radius Δr_1 . The subsequent generations would then continue to develop until the ionization region is filled with space charge [39]. The corona current is furthermore proposed to consist of both the *displacement*, also called *convection*, as well as the *conduction* components as discussed in section 2.6.2. The instantaneous corona current component due to the electron avalanche at

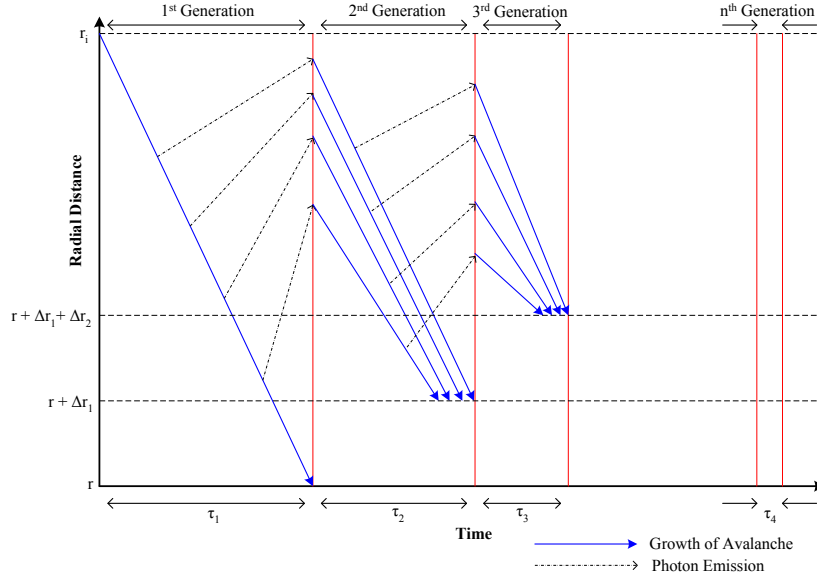


Figure 3.8: Spatial-temporal developments of successive avalanche generations forming the corona pulse [39]

a time t and position r_x , is calculated in [73] and [74] as per equation 3.10.3, where e is the electron charge, N_e is the electron number density, μ_e is the electron mobility and E is the resultant electric field due to the applied voltage and the positive ion space charge from preceding events.

$$i_+(t) = e \cdot N_e(r_x) \cdot \mu_e \cdot E^2(r_x)/V \quad (3.10.3)$$

The current components due to the positive and negative ions are treated similarly. This agrees with the work in [62] and [63].

3.10.2 Negative Streamer Development

Corona occurring on a negative conductor is initiated by electrons that are sufficiently accelerated away from the conductor with a drift velocity given by equation 2.4.15. The electrons created during the avalanche process then enters the low field region ($\alpha < \eta$) where they attach to neutral molecules to form negative ions. It is suggested in [74] that the electrons gradually get attached to these gas molecules to form negative ions, and the number of negative ions produced over a distance x outside the ionization region is given by

$$N_-(x) = \int_0^x \eta N_e(x) dx \quad (3.10.4)$$

where N_e is the electron number density after the whole distance of the electron avalanche and η is the attachment coefficient. Following the onset of steady negative corona, the conductor surface voltage gradient increases. The positive ions left behind as a result of the avalanche will then neutralise on the conductor. The ions travel at a velocity given by the ion mobility in equation 2.4.20, and electric field at the particle positions. Excited molecules will emit their excess energy in the form of photon radiation, and positive ions as well as these photons will create secondary emissions when arriving at the conductor [12]. In both [12] and [73] the number of photons created during the avalanche in a radial distance r is given by equation 3.10.5.

$$N_{photo} = \int_{r_0}^r \gamma_p \alpha(r) g(r) e^{-\mu(r-r_0)} dr \quad (3.10.5)$$

where γ_p is the coefficient of electron emission from the conductor surface per ionization event in the electron avalanche, g is the geometrical factor that gives rise to the fraction of photons produced at r reaching r_0 , α is the ionization coefficient, μ is the photo absorption coefficient in air and r_0 is the conductor radius. It was however discussed in [12] that only a small variation in the value of γ would be found in practical situations, and the corona onset gradients were calculated by keeping γ constant. Values of $\gamma_p = 10^{-3}$ for positive corona and $\gamma_p = 3 \times 10^{-3}$ and $\gamma_i = 5 \times 10^{-5}$ for negative corona were used where γ_i is the coefficient for positive ion impact. The negative corona current at a time t and position r_x is calculated in [74] and [73] as per equation 3.10.6.

$$i_-(t) = [N_e(r_x) \cdot \mu_e + N_-(r_x) \cdot \mu_-] e \cdot E^2(r_x) / V \quad (3.10.6)$$

In equation 3.10.6 N_e and μ_e are the electron number density and mobility respectively, N_- and μ_- are the negative ion number density and mobility, e is the electron charge and E is the resultant electric field due to the applied voltage and the generated space charge. This once more is similar to the work in [62] and [63].

3.10.3 PIC Streamer Development Flowchart

The flowchart for the PIC spatial-temporal streamer development model is shown in figure 3.9.

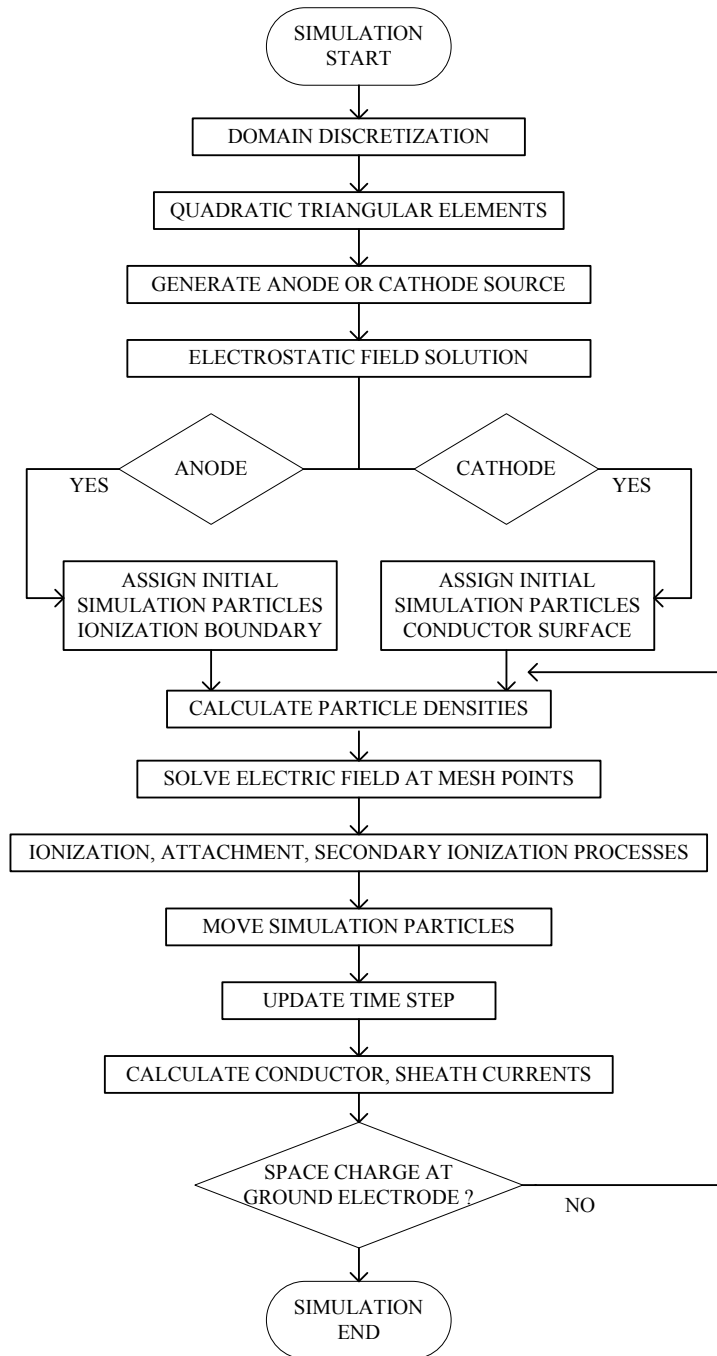


Figure 3.9: PIC streamer development flowchart

Chapter 4

Space Charge Particle Dynamics

The particle-in-cell (PIC) computational code, discussed in chapter 3, is used to model the various physical processes contributing to corona discharges (chapter 2). The numerical solution provides snapshots, as well as time histories, of the various electric field, ion space charge density and current components during these processes. A designed and developed electrometer-type circuit, with a sensing electrode based on the *Wilson plate*, is used to measure the ion space charge. This is done for a conductor above a ground plane, as well as a cylindrical corona cage environment, to obtain a temporal view of the ion space charge formation and build-up during corona events. The PIC computational code, together with the electrometer-type circuit, are used to gain a better understanding of the particle dynamics of the space charge created during corona discharges.

4.1 Numerical Code Validation

The PIC numerical solutions to the various field and charge density components are firstly compared to analytical solutions, and then to commercial codes where possible. This is done for a parallel plate and co-axial cylindrical electrode arrangement.

4.1.1 Parallel Plate Electrode Solution

The first exercise to validate the numerical code is to solve for a uniform electrostatic, *space charge free* solution of 1V applied to the top of a parallel plate electrode arrangement. The meshing for the first and second order basis functions is shown in figure 4.1, while the uniform potential and electric field solutions are shown in figures 4.2 and 4.3 respectively.

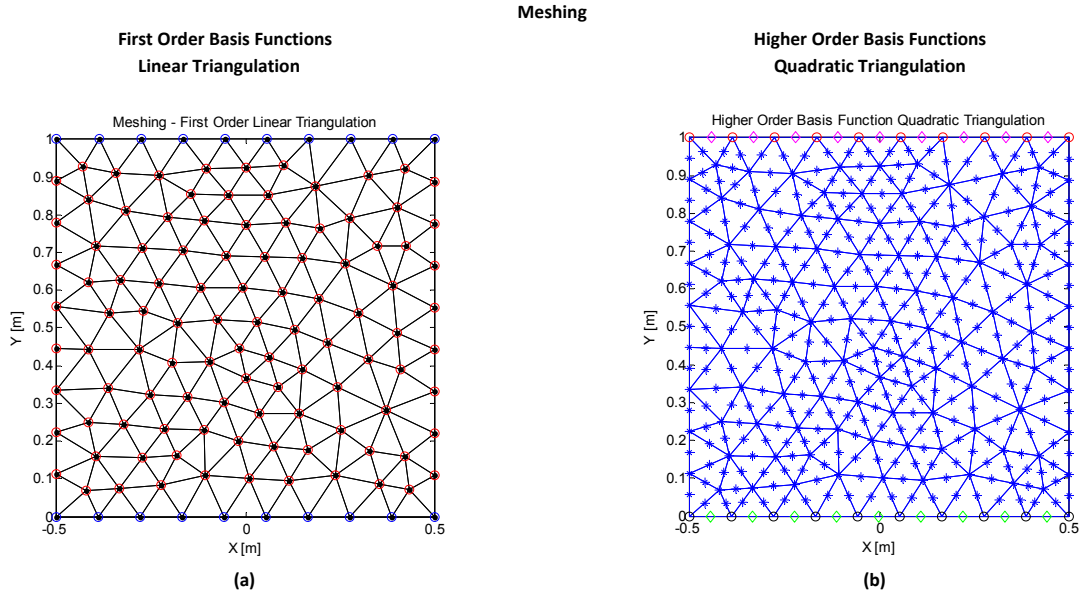


Figure 4.1: (a) First order domain discretization (b) Second order domain discretization

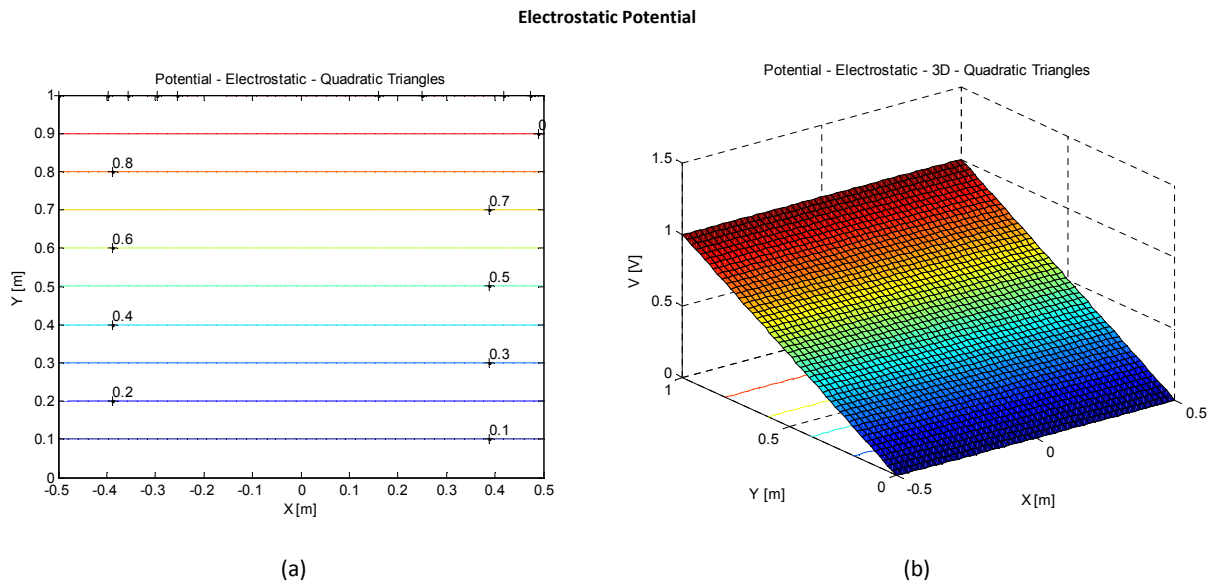


Figure 4.2: (a) 2D Electrostatic potential solution (b) 3D Electrostatic potential solution

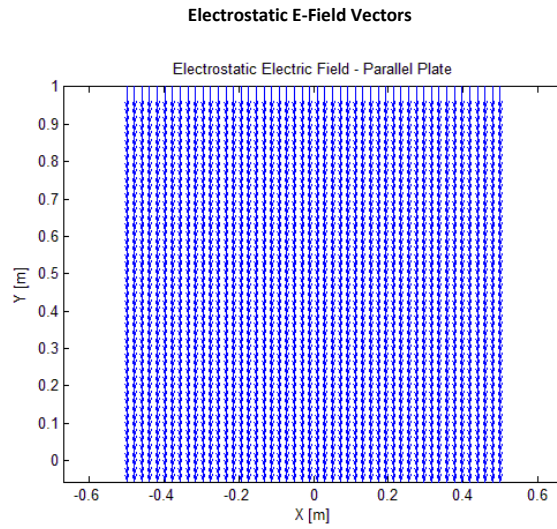


Figure 4.3: The parallel plate electrostatic E-field vector solution

The *space charge* potential solution for a single simulation particle, containing 6.25×10^7 positive ions, is shown in figure 4.4. The simulation particle of $10pC$ charge is situated in the centre between the two parallel plates of zero potential. The space charge electric field vectors are shown in figure 4.5.

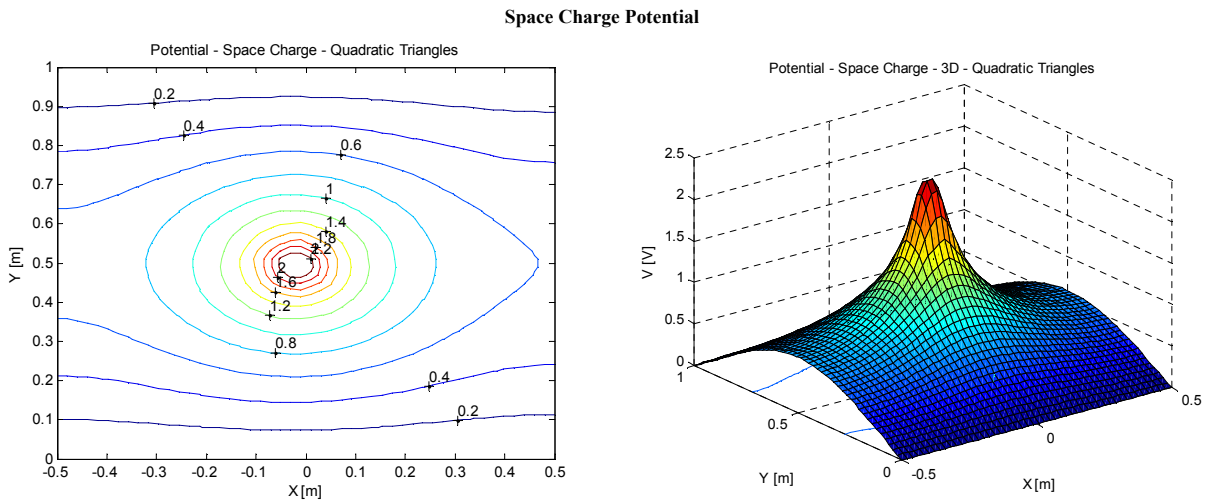


Figure 4.4: The parallel plate space charge potential solution

The analytical solution for the electric field of an isolated infinite uniform linear line charge of density λ_l is given in [75] by equation 4.1.1.

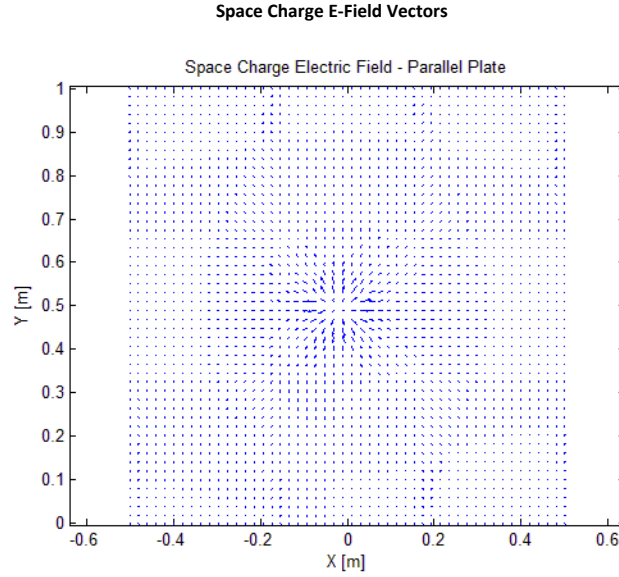


Figure 4.5: The parallel plate space charge E-field vector solution

$$\vec{E} = \frac{\lambda_l}{2\pi\epsilon_0 r} \quad (4.1.1)$$

When integrating this solution from some reference radius of zero potential, r_0 , to a radius r , the potential for the linear line charge is given in [76] as

$$\phi = - \int_{r_0}^r \vec{E} dr = - \frac{\lambda_l}{2\pi\epsilon_0} \ln\left(\frac{r}{r_0}\right) \quad (4.1.2)$$

4.1.2 Cylindrical Electrode Solution

The commercial software used to generate comparative results is the *Computer Simulation TechnologyTM* (CST) electromagnetic simulation package developed in Germany. The electrostatic solver in the *CST Particle StudioTM* suite was utilised, and the field results compared to the PIC solution. CST uses the finite difference time domain (FDTD) numerical method. The meshing of the 2D PIC cylindrical corona cage as well as the 3D CST model is shown in figure 4.6.

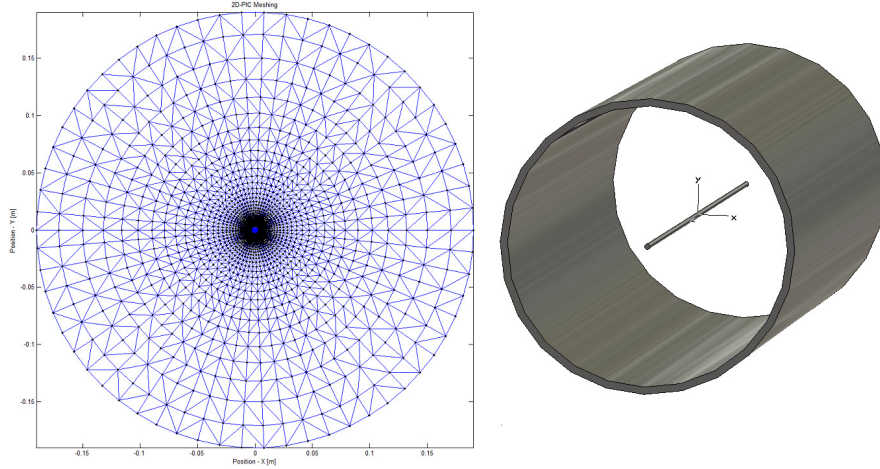


Figure 4.6: (a) 2D PIC meshing and (b) 3D CST cylindrical geometry

4.1.3 Space Charge Free Solution

The next step in validating the numerical code is to solve for the *space charge free* electrostatic \vec{E} -field solution in a co-axial cylindrical electrode arrangement. It was discussed in section 3.4 that the PIC computational code uses the charge simulation method (CSM) to solve for the Laplace equation. The radial solution to the electrostatic \vec{E} -field at a radius r inside a co-axial arrangement, with conductor radius r_c and sheath radius R_s , is evaluated analytically using

$$\vec{E}_{sf} = \frac{V}{r \ln(R_s/r_c)} \quad (4.1.3)$$

where V is the applied conductor voltage [77]. The analytical, PIC numerical and CST numerical solutions agree and are shown in figure 4.7.

4.1.4 Space Charge Solution

The *space charge* solutions to Poisson's equation in a co-axial electrode arrangement using the finite element method (FEM) and the CST electromagnetic simulation package are compared next. A scenario similar to the individual primitive streamer in [25] is considered where it is assumed that the electrons are instantly collected by the anode before negative ions are formed. The 360 simulation particles each represents 3.75×10^7 singly charged positive ions providing a total charge of $6 \times 10^{-12}C$. The 1m long simulation region thus has a linear charge density of $2.16 \times 10^{-9}C/m$. The location of the simulation particles at time $t = 0$ is shown in figure 4.9. The space charge density, potential, electric field and electric flux density are calculated

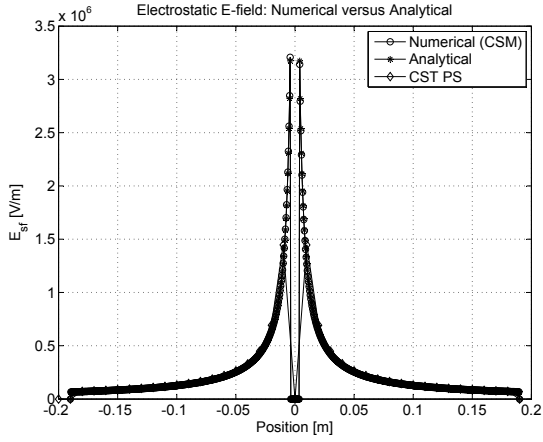


Figure 4.7: Electrostatic E-field in [V/m]

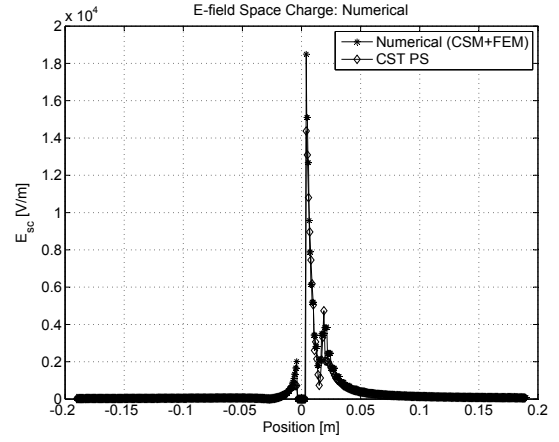


Figure 4.8: Space charge E-field in [V/m]

for the given simulation particle location. The space charge electric field (\vec{E}_{sc}) calculated with the PIC numerical code and commercial CST computational software is shown in figure 4.8. The high levels of electric field close to the conductor are due to the inaccuracies of the finite element solution in a highly divergent field close to boundaries. The space charge potential calculated with the PIC computational code is shown in figure 4.10. The space charge electric flux density is shown in figure 4.11, while the space charge density is shown in figure 4.12. The results obtained with the developed PIC computational code for the various space charge free and space charge components are consistent with that of the commercial CST electromagnetic simulation software. The CST space charge potential and electric flux density results are shown in figures 4.13 and 4.14 respectively.

The effect of using quadratic triangular elements instead of linear triangular elements is especially noticeable in the electric field solution shown in figure 4.15. It is clear from section 3.8.1 that the linear triangular elements use linear interpolation functions to solve for the potentials at the grid points. This implies that the electric field, which is the negative gradient of the scalar potential ($\vec{E} = -\nabla\phi$), is constant anywhere in an element. By using quadratic interpolation functions to solve for the potential at the grid points, a linear electric field interpolation is obtained anywhere in an element. Although more computationally intensive, this results in a higher level of accuracy for the space charge solution and is the motivation behind applying it in the numerical work in this dissertation.

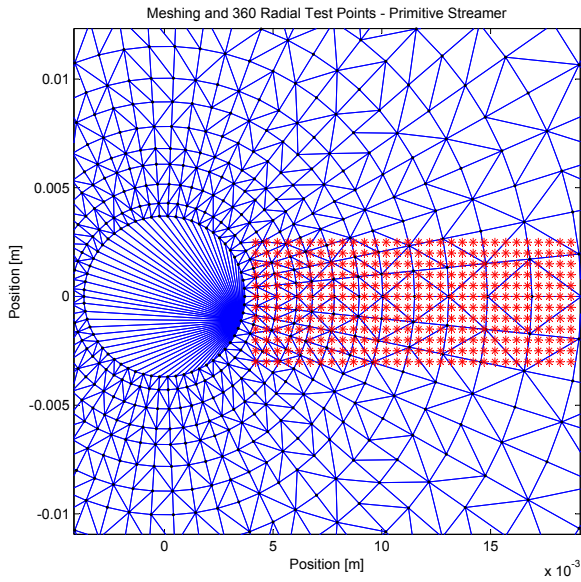


Figure 4.9: Location of simulation particles next to highly stressed conductor at time $t = 0$

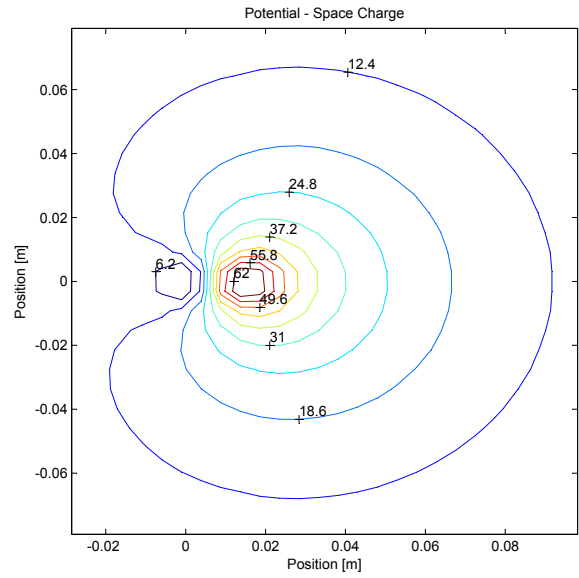


Figure 4.10: PIC (FEM) potential at time $t = 0$: Range 0 to 62V

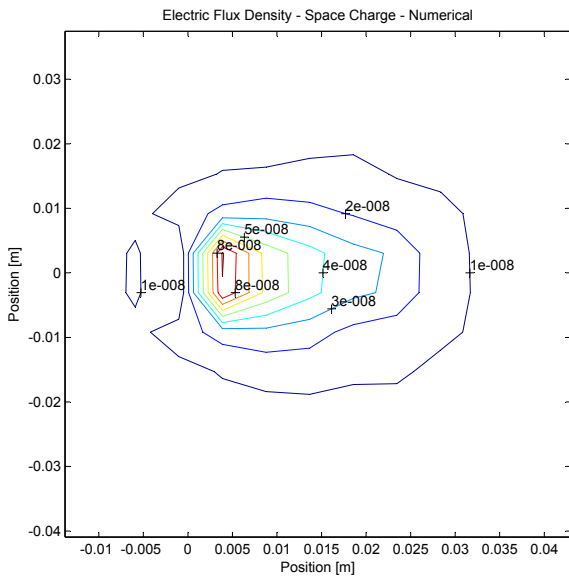


Figure 4.11: PIC (FEM) electric flux density at time $t = 0$: Range 1×10^{-8} to $10 \times 10^{-8} C/m^2$

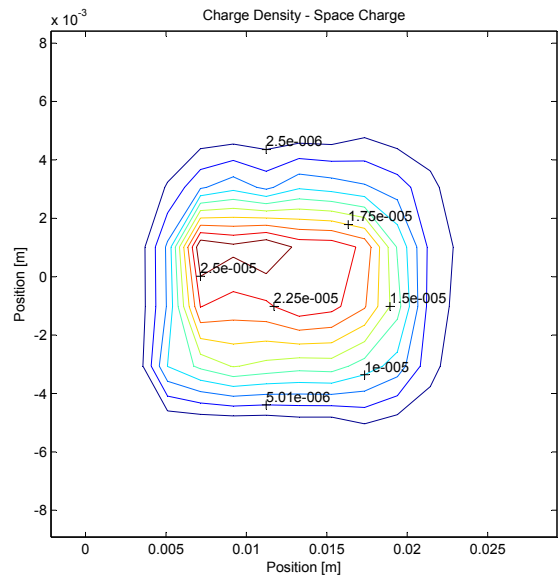


Figure 4.12: PIC (FEM) space charge density at time $t = 0$: Range 2.5×10^{-6} to $22.5 \times 10^{-6} C/m^3$

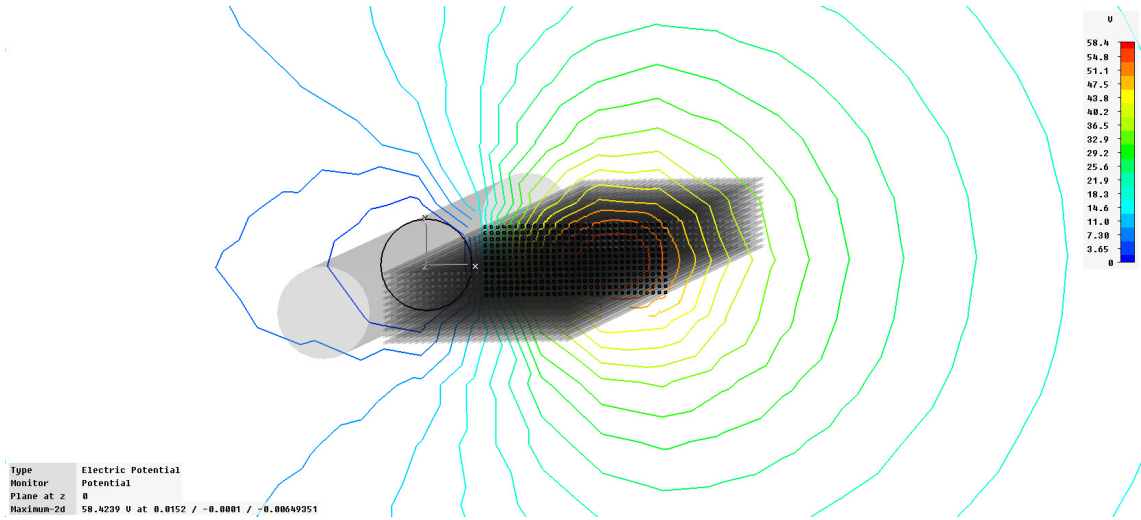


Figure 4.13: CST space charge potential at time $t = 0$: Range 0 to 58.4V

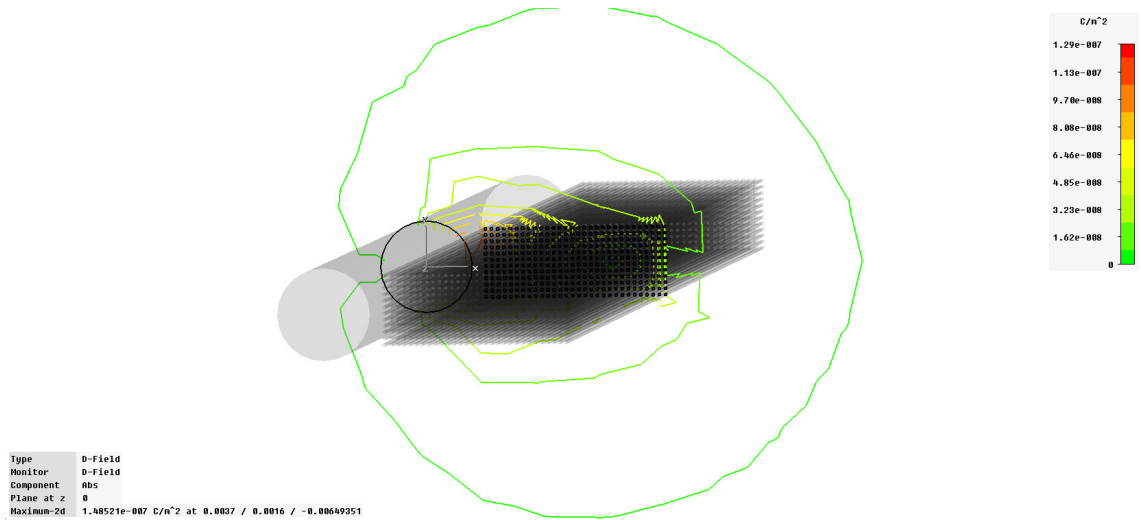


Figure 4.14: CST space charge electric flux density at time $t = 0$: Range 1.6×10^{-8} to $12.9 \times 10^{-8} C/m^2$

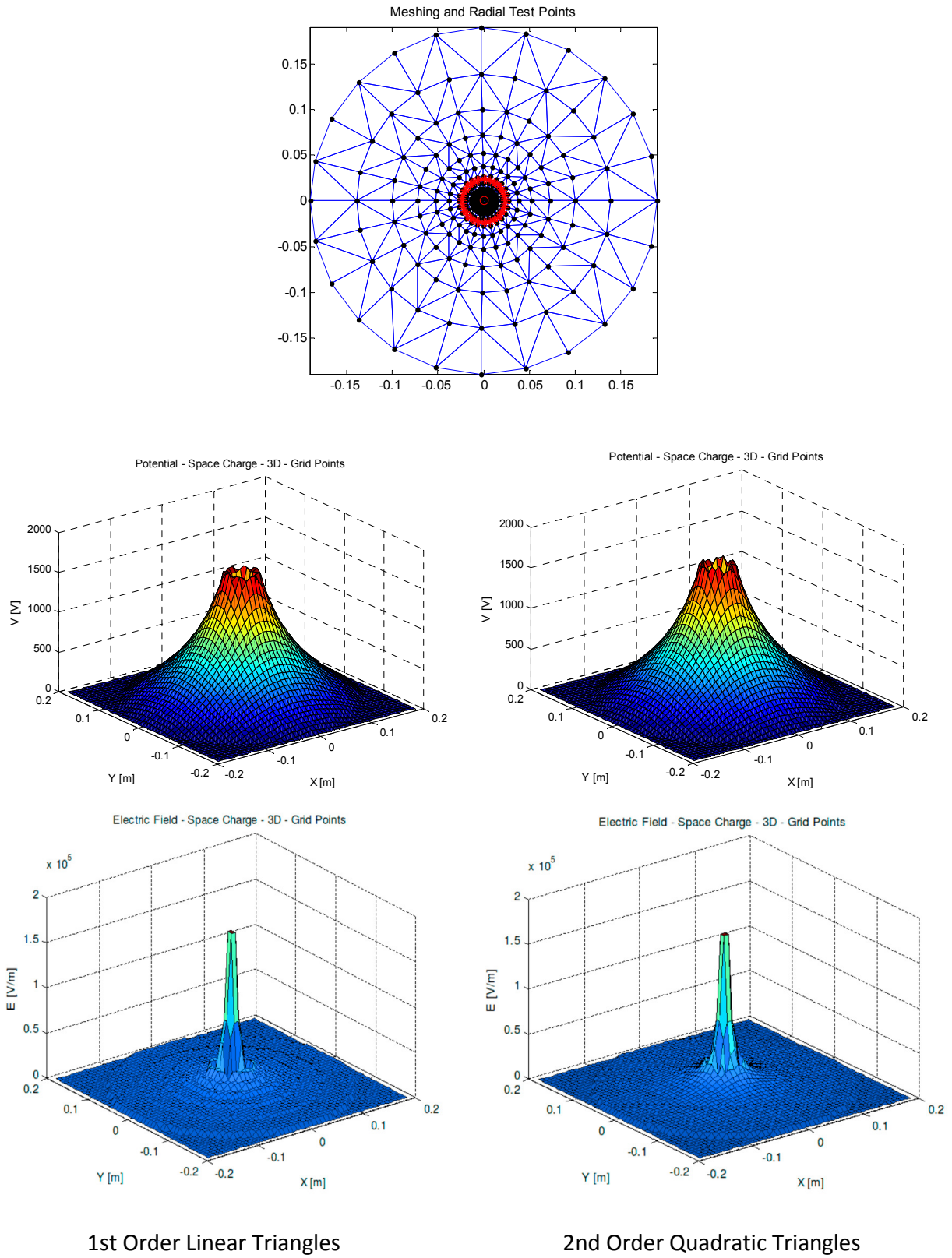


Figure 4.15: Quadratic and linear triangular elements used in the finite element method

4.1.5 Flow Vector and Time Integration Solution

The final stage in validating the computational code is the comparison of the numerical and analytical solutions to the particle flow vector given by equation 3.9.2 and the time integration given by equation 3.9.3. The PIC numerical solution is compared to an analytical solution for a co-axial cylindrical configuration example in [11]. A full analytical solution for the charge motion between cylindrical electrodes is provided in appendix D. Consider the specific case in figure 4.16 where the conductor radius is $r_c = 1cm$, the outer corona cage radius is $R = 100cm$, and the applied voltage to the centre conductor is $V = -140kV$. The numerical solution of the various particle parameters concerned when an electron drifts from the conductor surface to the ionization boundary is compared to the analytical solution in [11]. The results are shown in table 4.1

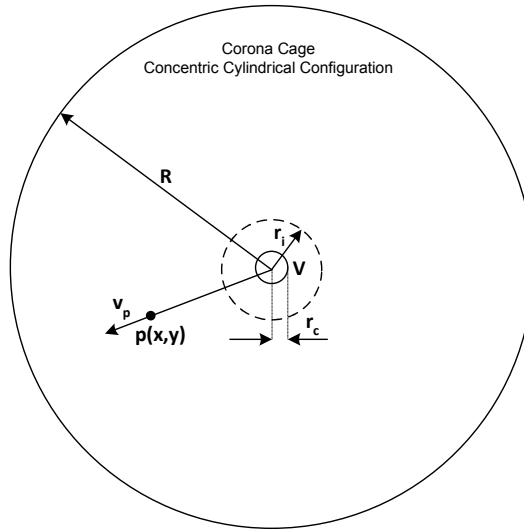


Figure 4.16: Specific example for charge motion in cylindrical configuration

The ionization zone or region is defined by the condition $\alpha = \eta$. An electron moving in the ionization zone close to the highly stressed conductor will travel with a drift velocity as defined in section 2.4.4. When electrons move outside this region attachment to neutral atoms result in the formation of negative ions. The velocity will then be determined by the mobility of the negative ion, assumed to be $\mu_e = 1.5cm^2/V.s$ in this example. The analytical equation for the time (t_i) it would take for an electron to travel from the conductor radius r_c to the ionization radius r_i is given by equation 4.1.4.

$$t_i = \frac{r_i - r_c}{v_e} \quad (4.1.4)$$

where v_e is the average electron drift velocity in cm/s.

Parameter Description	Variable	PIC Solution	Analytical Solution
Conductor Surface Gradient	E_c	30.46kV/cm	30.4kV/cm
Surface Gradient per Pressure	E_c/p	40.1V/cm.torr	40V/cm.torr
Ionization Zone Radius	r_i	1.258cm	1.25cm
Inception Voltage Gradient	E_i	24.16kV/cm	24.32kV/cm
Inception Gradient per Pressure	E_i/p	31.79V/cm.torr	32V/cm.torr
Average Electron Velocity	v_e	1.298×10^7 cm/s	1.296×10^7 cm/s
Electron Travel Time	t_i	19.2ns	19.3ns
Negative Ion Travel Time	t_n	6.18 μ s	6.17 μ s

Table 4.1: Results for electron motion in cylindrical configuration

The numerical solution of the electrostatic field is shown in figure 4.17, while the analytical and numerical solution of the electron position as a function of time is shown in figure 4.18.

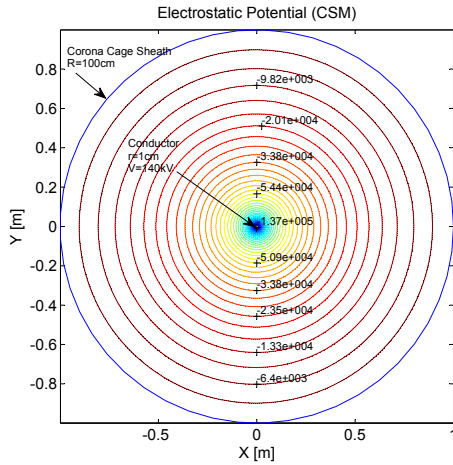


Figure 4.17: Electrostatic potential distribution calculated with the CSM

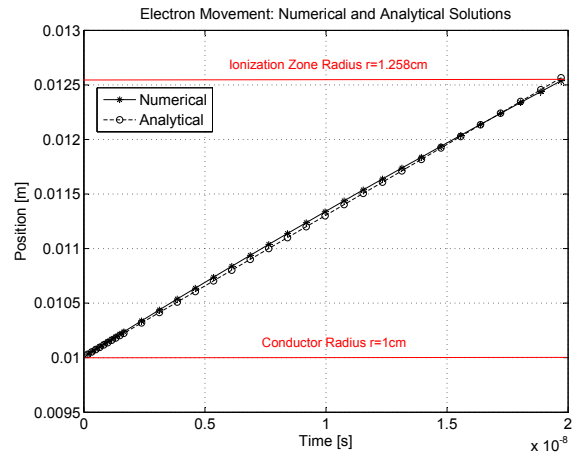


Figure 4.18: Electron movement calculated analytically and with PIC numerical code

The analytical solution for the time (t_n) it would take negative ions to travel from the conductor radius r_c to the ionization radius r_i is given by equation 4.1.5.

$$t_n = \frac{r_i^2 - r_c^2}{2\mu E_c r_c} \quad (4.1.5)$$

The numerical and analytical solution of the negative ion position between the conductor and ionization zone radius is shown in figure 4.19. The position as a function of time of an initial electron and subsequent negative ion in the lower field region is shown in figure 4.20.

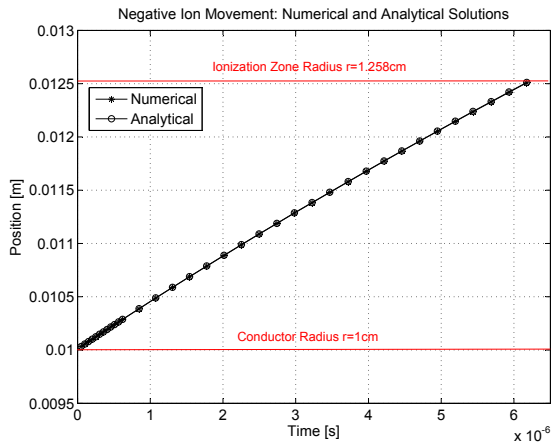


Figure 4.19: Time for negative ion movement from r_c to r_i calculated analytically and with PIC numerical code

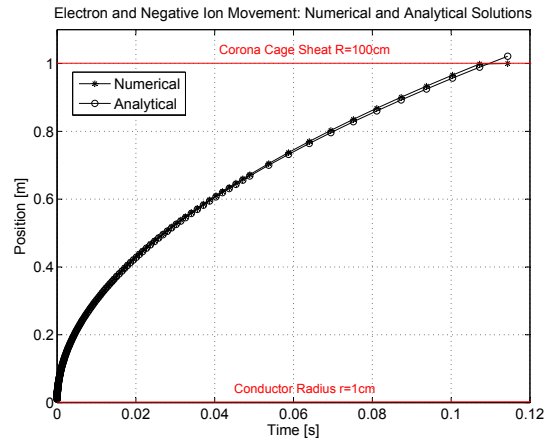


Figure 4.20: Total time for electron movement from r_c to r_i and negative ion movement from r_i to r_b

4.2 Ion Space Charge Travel-Time Predictions

The time it would take ion space charge created during a single corona event to travel from the conductor to the ground electrode is calculated for the various conductor corona test configurations discussed in chapters 5 and 6. The two types of measurement arrangements explored include a conductor above a ground plane and a co-axial cylindrical configuration as shown in figure 4.21. The RI performance of a single *Zebra* conductor of 28.68mm diameter, and a single *Kingbird* conductor of 23.88mm diameter was evaluated using three conductor corona test methods at high altitude. The timing results are calculated for surface voltage gradients between 30 and 34kV/cm and are shown in figure 4.22.

From these results it can be seen that the space charge created during a single corona event will have between 5 and 20 times less travel-time before reaching the ground electrode in the small

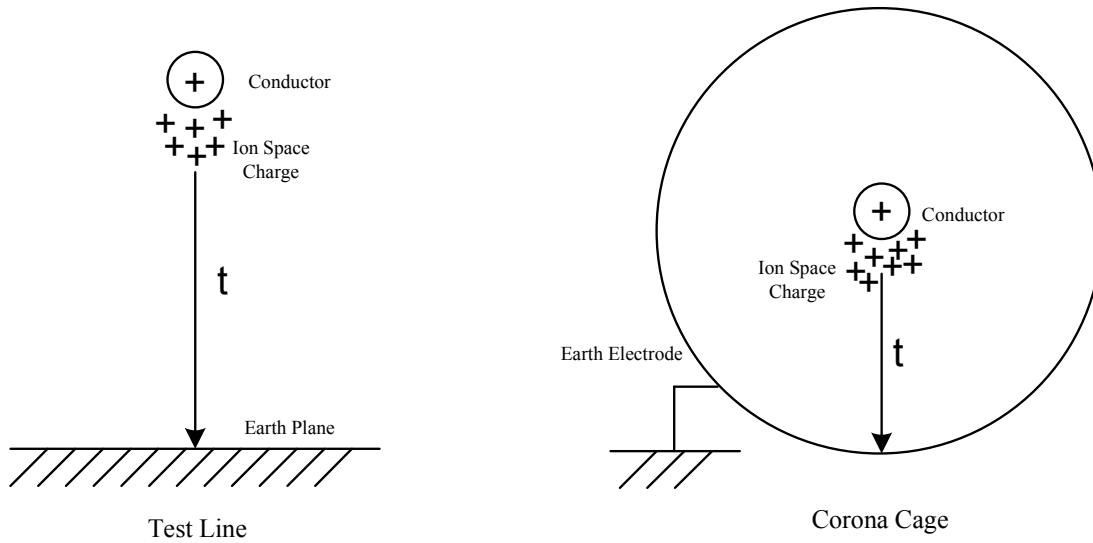


Figure 4.21: Test line and corona cage arrangements for ion space charge travel times

Gradient	Conductor Type	Large Corona Cage Ion Travel Time		Short Test Line Ion Travel Time		Small Corona Cage Ion Travel Time	
		p ⁺	n ⁻	p ⁺	n ⁻	p ⁺	n ⁻
E=30kV/cm	Zebra	1.03s	825.6ms	256.1ms	206.4ms	47.8ms	38.5ms
	Kingbird	1.24s	998.3ms	309.7ms	249.6ms	56.6ms	45.6ms
E=32kV/cm	Zebra	983.5ms	792.6ms	245.8ms	198.1ms	45.1ms	36.4ms
	Kingbird	1.15s	930.3ms	288.6ms	232.6ms	53.1ms	42.8ms
E=34kV/cm	Zebra	910.6ms	733.9ms	227.6ms	183.4ms	41.7ms	33.6ms
	Kingbird	1.10s	889.8ms	276.0ms	222.4ms	50.0ms	40.3ms

p⁺ positive ions; n⁻ negative ions

Figure 4.22: Ion space charge travels times for single corona events in various test methods

corona cage, than on the short test line and large corona cage respectively. The space charge reaching the ground electrode will take a certain time to be cleared out of the measurement system due to the time constants determined by the capacitance, resistance and inductance of the test method. If the space charge is not cleared fast enough between corona events, the accumulated space charge from a preceding event will repel approaching ions from a following event. This will then cause space charge to build up inside the electrode gap, resulting in a distortion of the electric field. It will also influence the conductor surface voltage gradient and corona inception levels. The smaller the electrode gap, the faster the space charge build-up in close proximity to the conductor, which will affect the conductor surface gradient and high field region.

4.3 Avalanches and Space Charge Dynamics

In the development of the streamer discharge, as in the case of the initial Townsend-type breakdown, it is assumed that an electron accelerated in a sufficiently high electric field will cause electron avalanches [78] as given by equation 2.4.11. In [79] it is observed that the minimum number of electrons required for a streamer discharge appears to be in the order of 7.6×10^8 , and this corresponds to a charge release of 122pC. It was furthermore noted in [80] that a single electron avalanche becomes a self-sustaining streamer discharge when the number of electrons approach 10^8 . The avalanche processes and positive and negative corona streamer developments are discussed next by example.

4.3.1 Anode Corona Streamers

Consider an anode conductor of radius $r = 1.41\text{cm}$ at a potential of $V = +400\text{kV}$ and height of $h = 640\text{cm}$ above a ground plane. This is a similar configuration to the computational work in [74]. The ionization region of radius $r_i = 2.44\text{cm}$ corresponds to the field strength such that $\alpha \geq \eta$ as shown in figure 4.23(a).

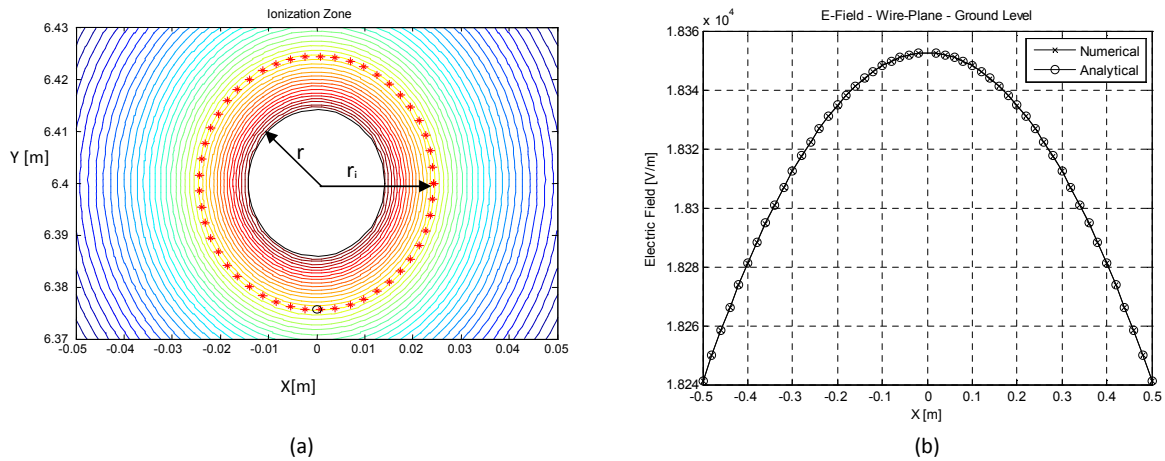


Figure 4.23: (a) Ionization region of $r_i = 2.44\text{cm}$ around anode conductor $r = 1.41\text{cm}$ (b) Electric field at ground level due to anode conductor-plane configuration

The electric field strength due to the electrostatic charge on the conductor calculated at ground level is shown in figure 4.23(b). During positive corona, electrons move in an increasing field and the numbers increase exponentially. The majority of the electrons and photons are produced

almost at the moment the avalanche terminates its growth [74]. This is shown in figure 4.24(a). The growth of the avalanche head radius, that is a function of the avalanche lifetime and electron diffusion coefficient, is shown in figure 4.24(b). The displacement current on the anode due to the electron avalanche development is shown in figure 4.25.

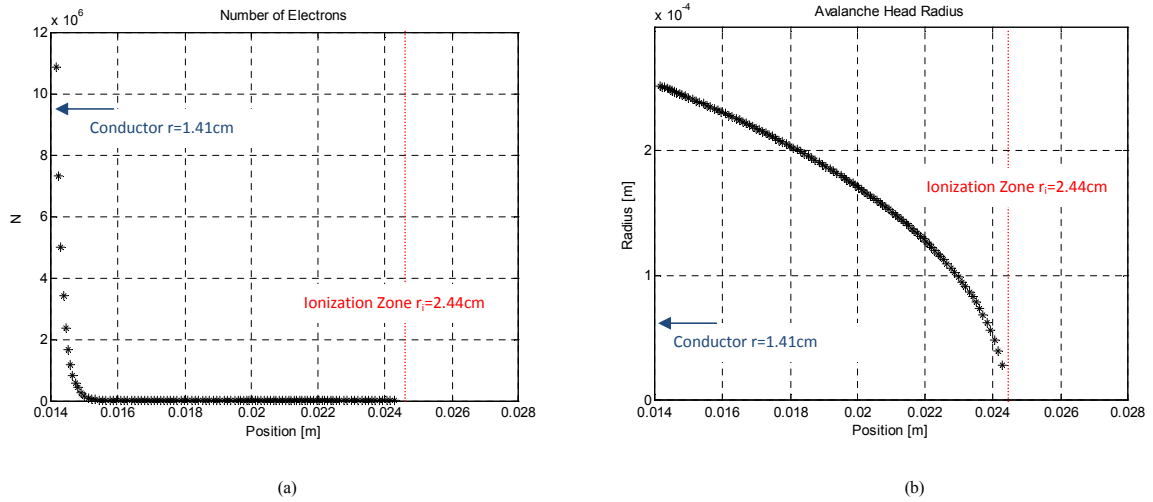


Figure 4.24: (a) The number of electrons created by electron avalanche (b) Head radius of electron avalanche

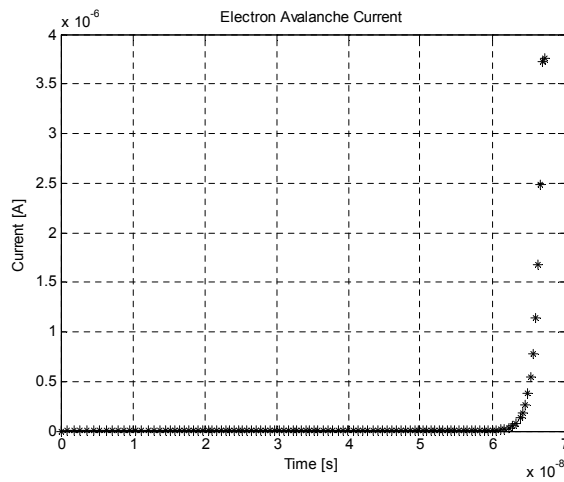


Figure 4.25: Current on conductor due to electron avalanche

4.3.2 Cathode Corona Streamers

Consider a cathode conductor of radius $r = 3.1\text{mm}$ at a potential of $V = -68\text{kV}$ in a corona cage of radius $R = 200\text{mm}$. This arrangement is similar to the computational work in [74]. The boundary of the ionization zone is calculated to be a radius of $r_i = 6.8\text{mm}$. The number of electrons created in a decreasing electric field by a single electron starting at the conductor surface is shown in figure 4.26, while the radius of the avalanche head is shown in figure 4.27. The calculated cathode conductor corona current is shown in figure 4.28, while the spatial-temporal development of the space charge giving rise to the current is shown in figures 4.29 and 4.30.

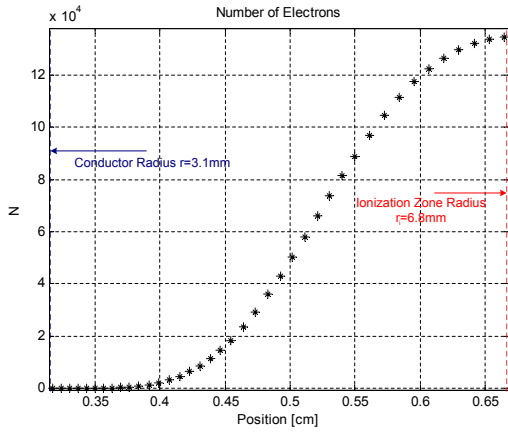


Figure 4.26: Number of electrons created by electron avalanche

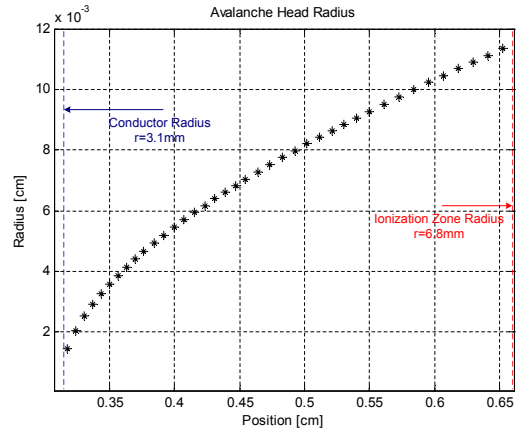


Figure 4.27: Head radius of electron avalanche as a function of lifetime

In the example of the cathode corona spatial-temporal development, the blue circular markers are the initial electrons starting from rest at 10 positions around the conductor surface. The position and number of initial sites were chosen for demonstration purposes. At time $t = 10\text{ns}$, the start of the electron avalanches and positive ion formation (red star markers) are observed as the electrons are accelerated away from the conductor surface. The electrons in the avalanche outside of the ionization region start attaching to neutral molecules to form negative ions. These are the purple triangular markers as seen at time $t = 120\text{ns}$. Between $t = 1\mu\text{s}$ and $t = 1\text{ms}$ the positive ions, now in a higher field region than the negative ions, will be collected by the conductor. The negative ions can then be tracked until they neutralise on the earth electrode at a time of $t = 6.9\text{ms}$.

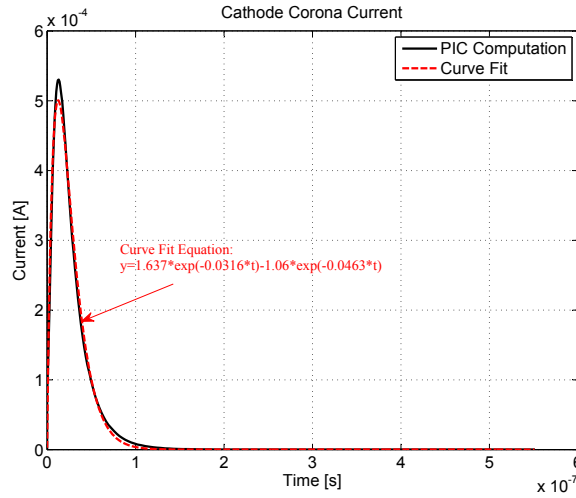


Figure 4.28: Cathode corona current pulse computed with Particle-In-Cell code

4.4 Altitude Effects

It is important to be able to predict environmental altitude effects like air pressure and temperature on the conductor corona RI levels. Measurements to investigate this phenomena were made with a mobile small corona cage at various heights above sea level. The altitude effects on the RI performance of a single *Zebra* and *Kingbird* conductor were investigated for both positive and negative DC polarities. The results of these measurements are discussed in detail in appendix E.

The reason for earlier corona inception and higher RI levels at higher altitudes (lower air pressure) are explored by simulating the various altitude and temperature effects on the ionization region using the PIC numerical code. The actual height above sea level, and air temperature recorded on the various days of testing in appendix E, were used as input for the PIC code. The calculated ionization regions for these inputs are shown in figures 4.31 and 4.32 for the *Zebra* and *Kingbird* conductors respectively. It is clear that for a higher altitude and lower air pressure the ionization zone radius increases. This implies that the effective ionization area increases, and free electrons are therefore accelerated earlier into this drift region. The distance covered by the electron avalanche before neutralising on the conductor is larger, and the number of electrons created during this avalanche is greater than at a lower height above sea level (higher air pressure). Higher conductor corona current levels are measured at lower inception levels at high altitude.

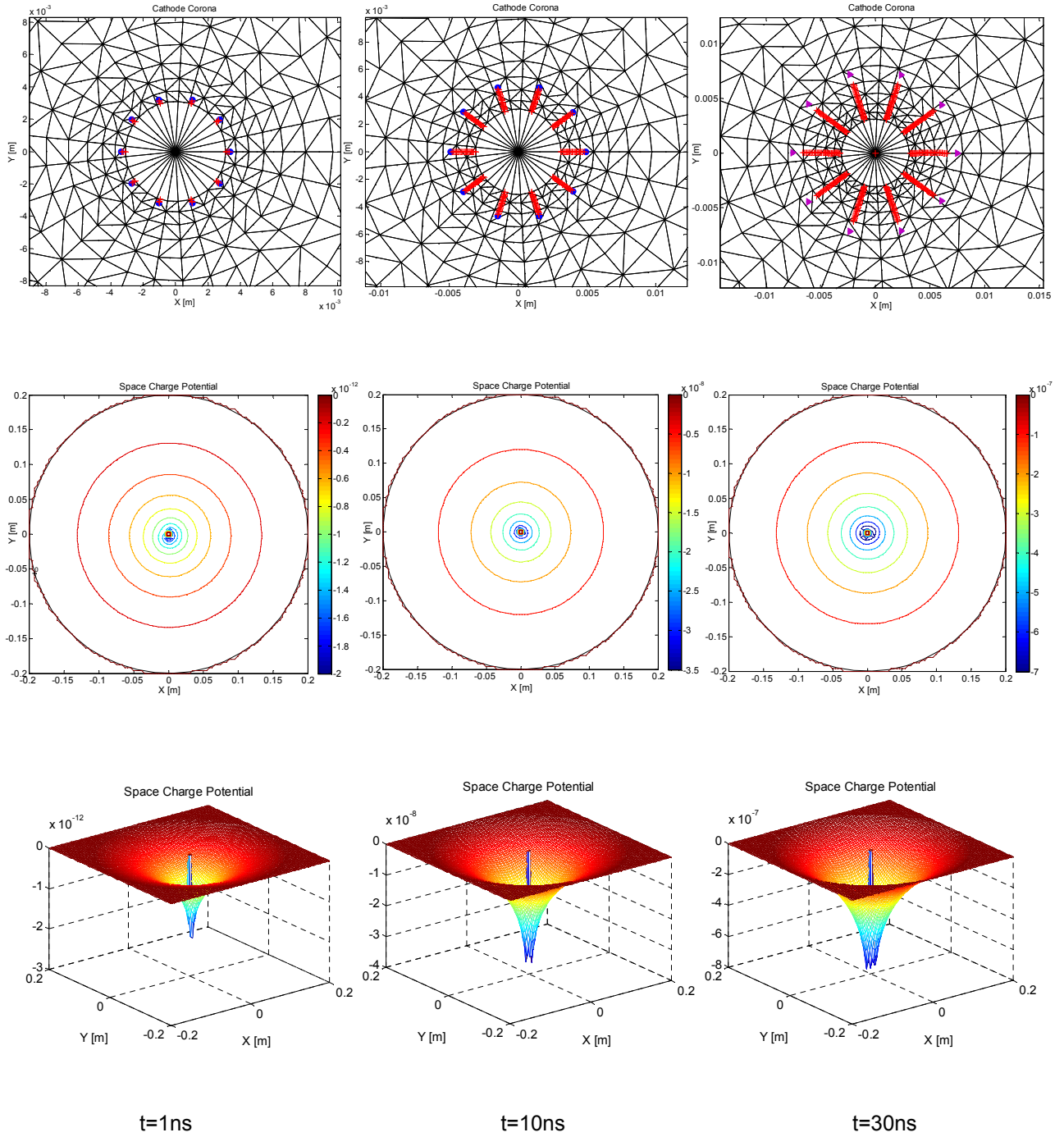


Figure 4.29: Cathode corona space charge spatial development 1ns to 30ns

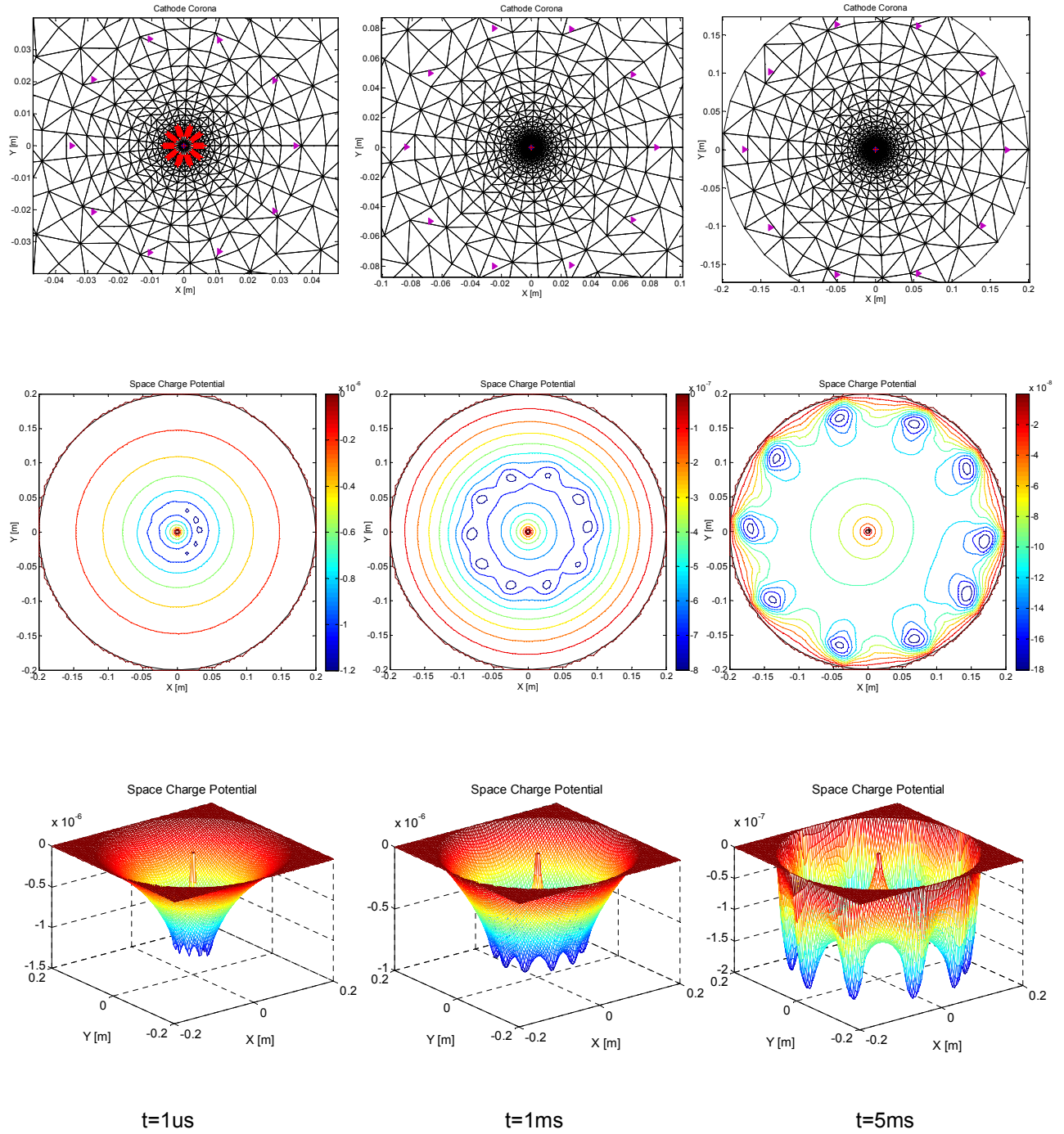


Figure 4.30: Cathode corona space charge spatial development 1us to 5ms

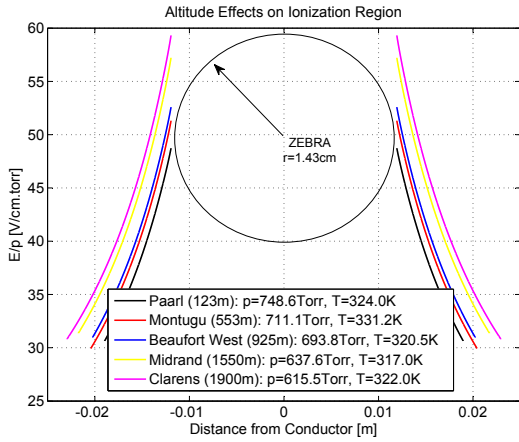


Figure 4.31: PIC computation of ionization region around Zebra conductor for various altitudes and temperatures

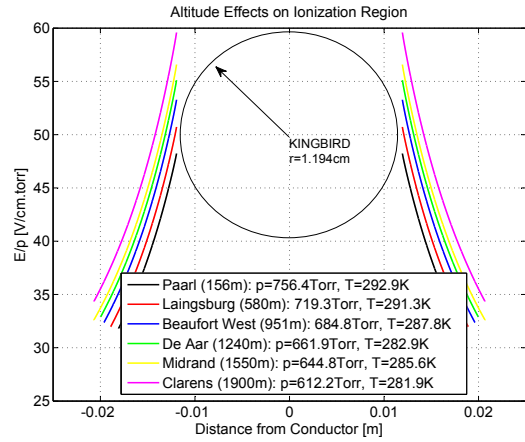


Figure 4.32: PIC computation of ionization region around Kingbird conductor for various altitudes and temperatures

4.5 Electrometer-type Circuit

During the initial attempt to study the space charge effects of conductor corona, the outer electrode of a laboratory corona cage was used as a “sensing electrode”. A 50Ω shunt resistor and high-speed sampling card were used to make a wideband measurement of the space charge created during a corona event. It was quickly evident that the sensitivity to detect the small amount of space charge neutralising on the outer cathode successfully was lacking. It was this initial finding that led to the investigation of an electrometer-type circuit to increase the measurement sensitivity [20], [81].

4.5.1 Circuit Design

The electrometer-type circuit that was designed is a battery powered, high-input unity-gain impedance translator consisting of a series of operational amplifiers as shown in figure 4.33. The amplifier has an input impedance in the tera-ohm range and an input bias current in the femto-ampere range. The input impedance is so high that the effective current in the circuit is zero. This makes the device sensitive enough to measure small amounts of charge in the vicinity of the sensing plate. The design is a differential circuit that will measure the potential difference between the sensing plate and the ground reference, hence measuring the change in electric field. The circuit was housed in a metal casing in order to shield against interference signals, while only the sensing plate was exposed.

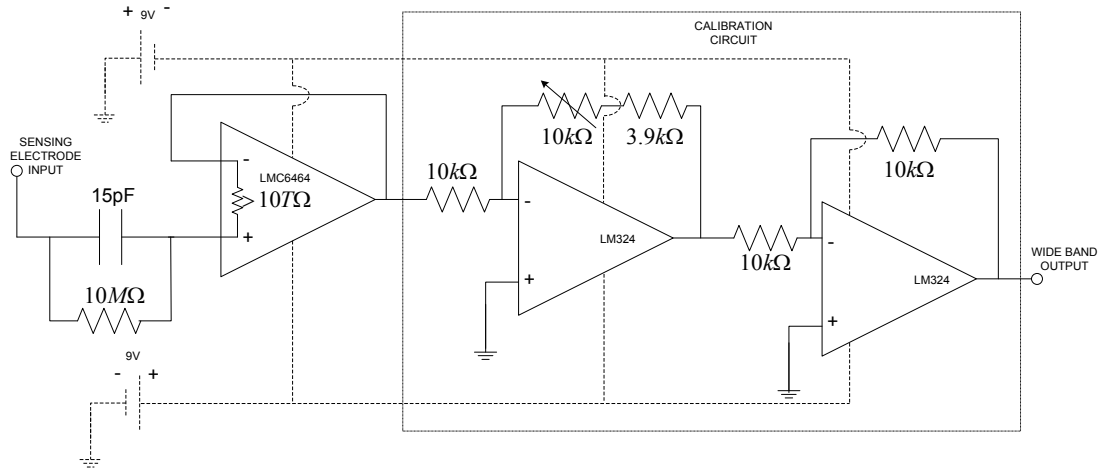


Figure 4.33: Electrometer circuit design schematic

4.5.2 Sensing Plate Design

The sensing plate design is based on the Wilson plate discussed in [42] and shown in figure 4.34. The sensing plate is connected to ground through the electrometer circuit while the guard ring in the initial experiment was left floating. The guard ring reduces fringing field effects and will have a potential close to that of the sensing plate. The leakage resistance between the sensing plate and guard ring is smaller than the input impedance of the electrometer circuit, and a substantial potential difference between the sensing plate and a grounded guard ring will cause the space charge to leak away to ground, rather than stay on the sensing plate. The sensing plate, shown in figure 4.35, was placed flush with an aluminium ground plane to prevent field distortion.

4.5.3 Operating Principle

The current density experienced by the sensing plate due to the ion space charge will have both a displacement current density and a conduction current density component. The displacement current density is due to the space charge approaching the sensing plate and the conduction current density is due to the space charge neutralising on the sensor.

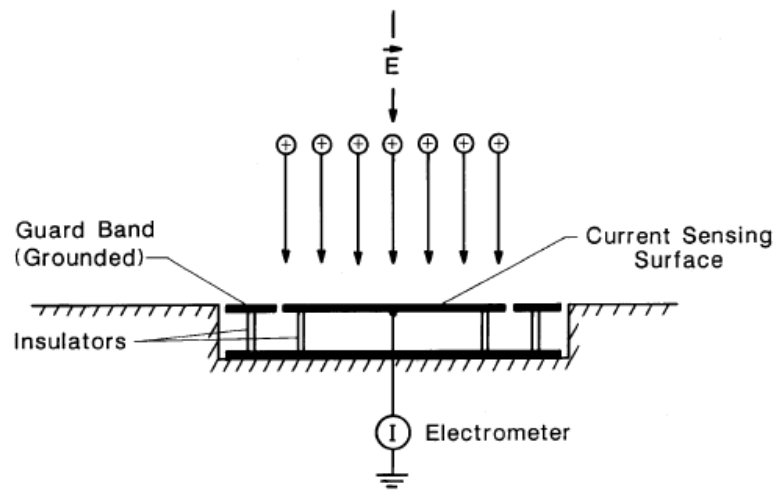


Figure 4.34: Schematic view of Wilson plate mounted flush with ground plane [42]

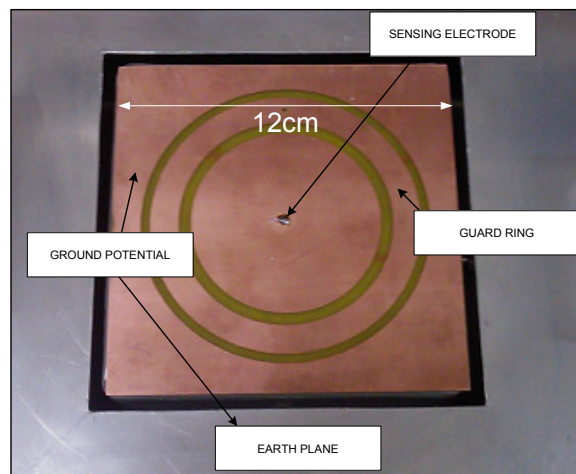


Figure 4.35: Sensing electrode design placed flush with aluminium ground plane

4.5.4 Calibration

The circuit was calibrated using a parallel plate arrangement which has a simple analytical solution for the expected electric field and charge densities. A square aperture slightly bigger than the sensor was cut into the bottom plate to place the sensor flush with the ground plane. This ensured that the measurement device did not cause an enhancement of the electric field. The calibration was done in a screened room environment to eliminate background interference. The capacitance between the parallel plates is a function of the plate area:

$$C = \epsilon_0 \frac{A}{d} \quad (4.5.1)$$

In equation 4.5.1 ϵ_0 is the permittivity of free space given in F/m, A is the area of the plates given in m^2 and d is the distance between the plates in m. The charge voltage (QV) relationship to the capacitance is given by

$$C = \frac{Q}{V} \quad (4.5.2)$$

In equation 4.5.2 Q is the charge in C and V is the applied voltage in V. The calibrating procedure was to measure the output of the circuit for various applied voltages (and hence voltage gradients or electric field strengths) as well as frequencies (changes in electric field). The total charge created on the plates was calculated using the QV relationship in equation 4.5.2. The ratio of the areas of the plate and sensor was used to calculate the amount of charge that will be expected on the sensing plate for a given applied voltage. There was a satisfactory correlation between the measured and predicted values, except for a slight deviation for the higher applied voltages and frequencies. This may be due to the slew rate of the operational amplifiers as well as the sensing plate to ground capacitance acting as a filter at these higher frequencies. The measured voltage values are shown in figure 4.36 and table 4.2. The successful calibration of the system in terms of measured and predicted charge values was achieved and the charge prediction results are shown in figure 4.37 and table 4.3.

Electrometer Calibration Data				
Frequency	$V_1 = 0.5V$	$V_2 = 1V$	$V_3 = 2V$	$V_4 = 5V$
$f = 20Hz$	15.81mV	29.39mV	57.61mV	141.69mV
$f = 50Hz$	15.61mV	29.87mV	58.09mV	142.77mV
$f = 100Hz$	15.81mV	29.13mV	58.09mV	142.87mV
$f = 500Hz$	15.23mV	28.12mV	55.17mV	135.74mV
$f = 1000Hz$	13.73mV	25.29mV	51.16mV	125.68mV

Table 4.2: Measured voltage data from electrometer parallel plate calibration

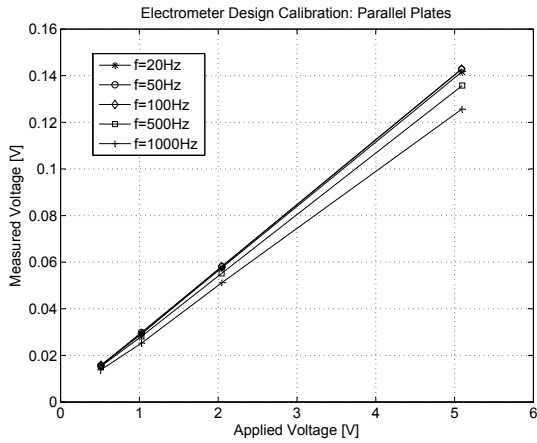


Figure 4.36: Measured voltage on electrometer sensing plate for given applied voltage and frequency

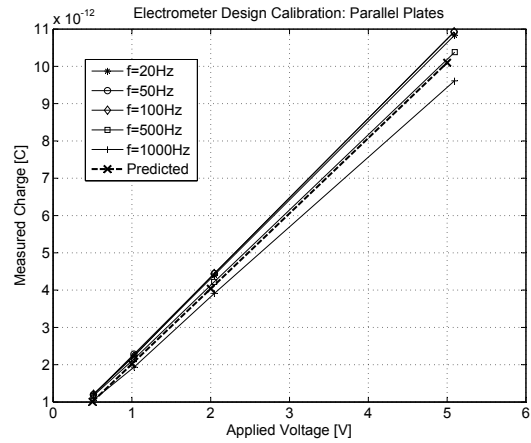


Figure 4.37: Measured and predicted charge values on electrometer sensing plate for given applied voltage and frequency

Electrometer Calibration Data				
Frequency	$V_1 = 0.5V$	$V_2 = 1V$	$V_3 = 2V$	$V_4 = 5V$
$f = 20Hz$	1.21pC	2.25pC	4.41pC	10.84pC
$f = 50Hz$	1.19pC	2.28pC	4.44pC	10.91pC
$f = 100Hz$	1.21pC	2.23pC	4.44pC	10.93pC
$f = 500Hz$	1.16pC	2.15pC	4.22pC	10.38pC
$f = 1000Hz$	1.05pC	1.93pC	3.91pC	9.61pC

Table 4.3: Measured charge data from electrometer parallel plate calibration

4.6 Space Charge Measurements

4.6.1 Experimental Arrangement

The electrometer circuit was placed in the experimental arrangement shown in figure 4.38. A smooth copper conductor with a radius $r_1 = 6mm$ was suspended on insulators above an aluminium ground plane. A small steel sphere with a radius of $r_2 = 1.15mm$ was placed into a pre-drilled hole in the centre of the smooth conductor such that half of its surface protruded. This was done to create an irregularity on the otherwise smooth copper conductor. The artificial corona source is used to simulate semi-realistic conductor surface imperfections.

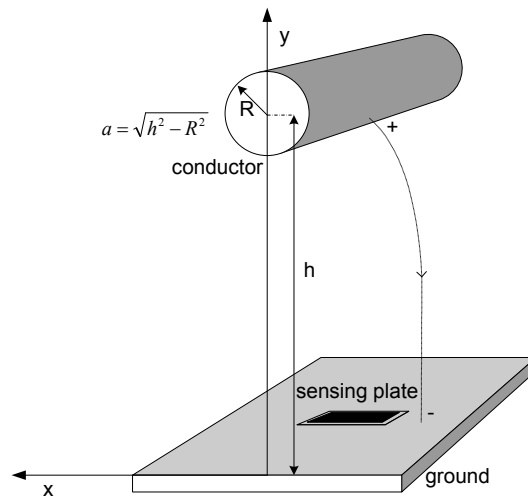


Figure 4.38: Experimental arrangement for conductor above ground plane

The artificial corona source shown in figure 4.39 will increase the electric field in its vicinity and hence the ionization and avalanche processes for onset streamer discharges. This will occur at a lower gradient than needed for the conductor to be in corona, hence ensuring space charge formation at this point only. The sensing electrode was placed directly underneath the source which pointed down towards the sensing plate and ground plane. A square aperture in the ground plane slightly bigger than the sensor ensured that the measurement device did not cause any field enhancements.



Figure 4.39: Artificial corona source used in experimental arrangement

4.6.2 Test Circuit

A high-voltage direct-current power source was connected to the conductor with the aluminium ground plane and electrometer shield plate earthed. A coupling capacitor and current transducer were connected across the test object to measure and trigger the corona current pulse propagating on the conductor. The electrometer and the current transducer output terminals were connected to a digitizing oscilloscope housed in an EMC (electromagnetic compatibility) shielding cabinet. The height of the conductor above the ground plane as well as the applied voltages were varied.

4.6.3 UV Intensifying Corona Camera

Images of the onset streamer discharges for various applied voltages and heights were captured using a special UV intensifying corona camera. The visual lengths of the streamers for the different voltages and heights were recorded. An example of a set of onset streamer discharges at a conductor height of $h=64.5\text{cm}$ above ground is shown in figure 4.40. The parallel lines at the top of the image is the side view reference position of the conductor, while a scale of increments of 1cm is shown on the left of each streamer discharge image. The increase in streamer length, as well as the brightness and intensity of the glow can clearly be noted as the applied voltage is increased. More UV intensifying corona images are shown in Appendix B.

4.6.4 Wire-Plane Numerical Solution

The analytical solution of the potential at a point (x, y) in the two dimensional *Cartesian* coordinate system for a space charge free wire-plane geometry shown in figure 4.38 is given in [75]

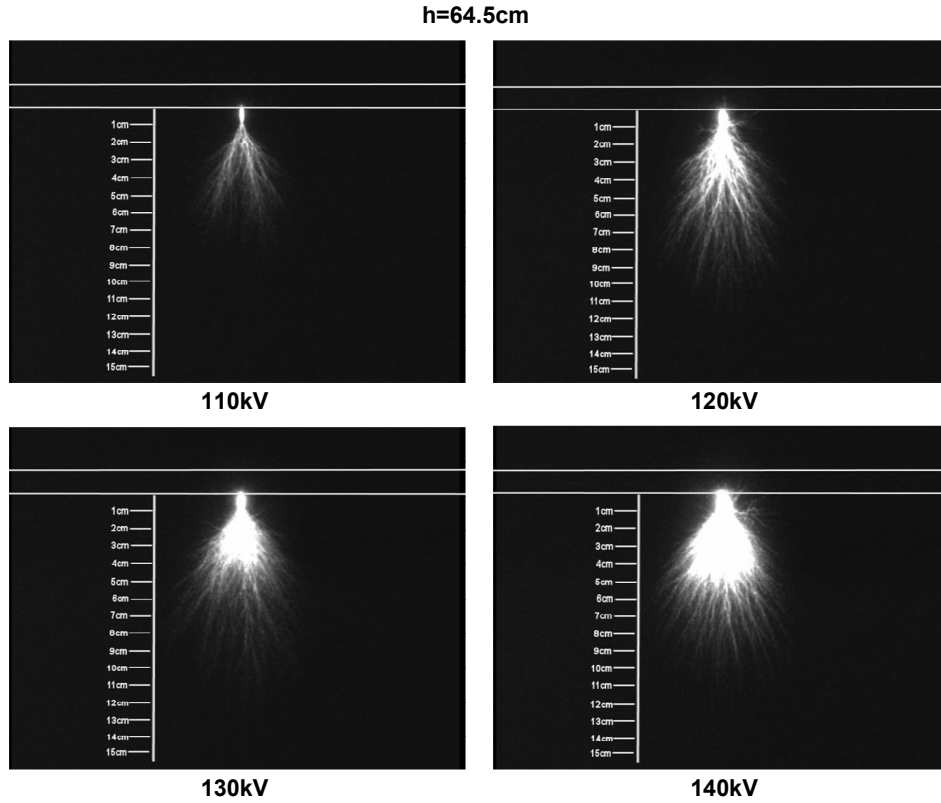


Figure 4.40: A set of onset streamer discharges captured with a UV intensifying corona camera for a conductor height $h = 64.5\text{cm}$ (vertical scale in 1cm increments)

and [76] as

$$\phi(x, y) = -\frac{\lambda}{2\pi\epsilon_0} \ln \frac{\sqrt{(a-y)^2 + x^2}}{\sqrt{(a+y)^2 + x^2}} \quad (4.6.1)$$

In equation 4.6.1, $\lambda = CV$ is the charge per unit length, V is the applied voltage, $a = \sqrt{h^2 - R^2}$ is a constant and C is the capacitance of the line given by

$$C = \frac{2\pi\epsilon_0}{\ln\left(\frac{h}{R} + \sqrt{\left(\frac{h}{R}\right)^2 + 1}\right)} \quad (4.6.2)$$

In equation 4.6.2, h is the height of the conductor centre above ground and R is the conductor radius. The field between the conductor and the ground plane can be described by a line charge in the centre of the conductor and its image below the ground plane. In the physical situation, however, the charge per unit length of the conductor is induced on the surface of the ground

plane. The electric field vector in a two dimensional space is given by the negative gradient of the scalar potential as in equation 4.6.3.

$$\vec{E} = -\vec{\nabla}\phi = -\left(\frac{\partial\phi}{\partial x}\hat{x} + \frac{\partial\phi}{\partial y}\hat{y}\right) \quad (4.6.3)$$

The wire-plane geometry potential and electric field distribution are shown in figures 4.41 and 4.42 respectively.

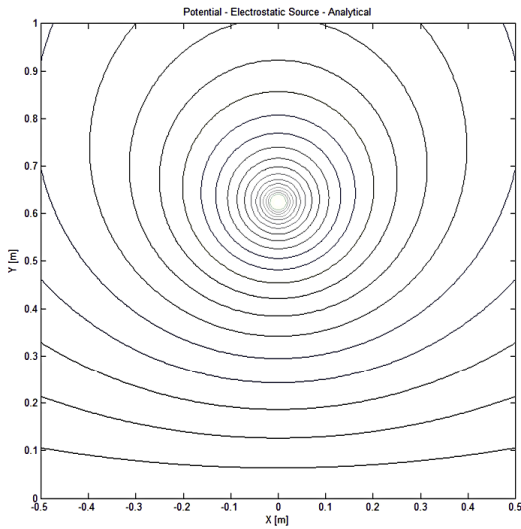


Figure 4.41: Analytical solution to the scalar potential for a wire-plane geometry

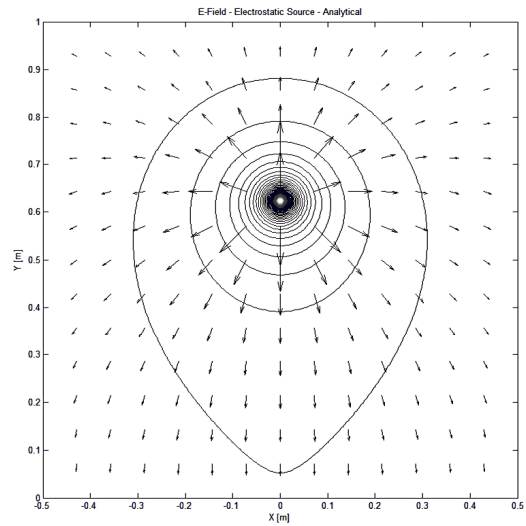


Figure 4.42: Analytical solution to the vector electric field for a wire-plane geometry

4.6.5 Measurement Results

The output of the electrometer circuit for positive ion space charge formed during anode corona processes is shown in figure 4.43. The top image shows the corona current pulse measured on the conductor using the test circuit discussed in section 4.6.2. The total current on the electrometer sensing plate due to the formation, displacement and conduction of the ion space charge is shown in the bottom image. Distinct timings, t_1 to t_4 in figure 4.43, are noted on the output of the electrometer. An example of the electrometer output to an anode and cathode corona pulse on a conductor at similar heights above ground and surface voltage gradients is shown in figure 4.44. The interpretation of these timings was confirmed by the PIC simulation in section 4.6.6, and is discussed in section 4.6.7.

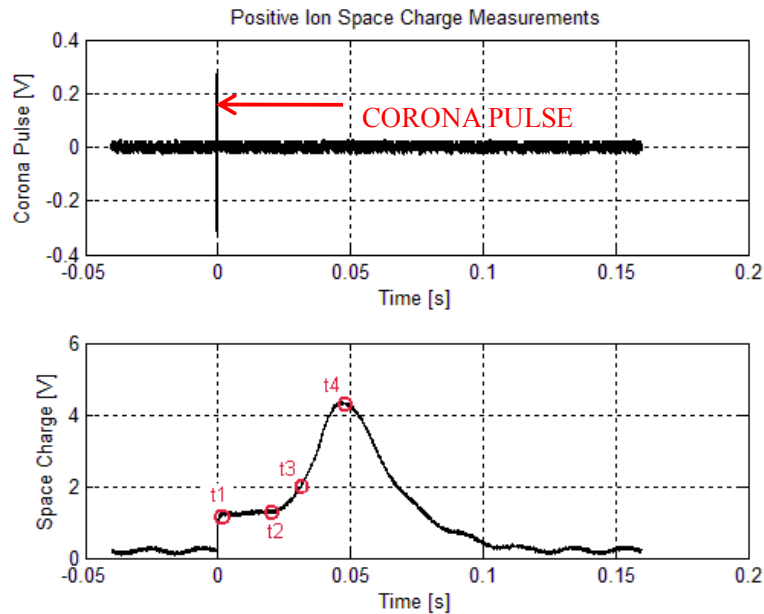


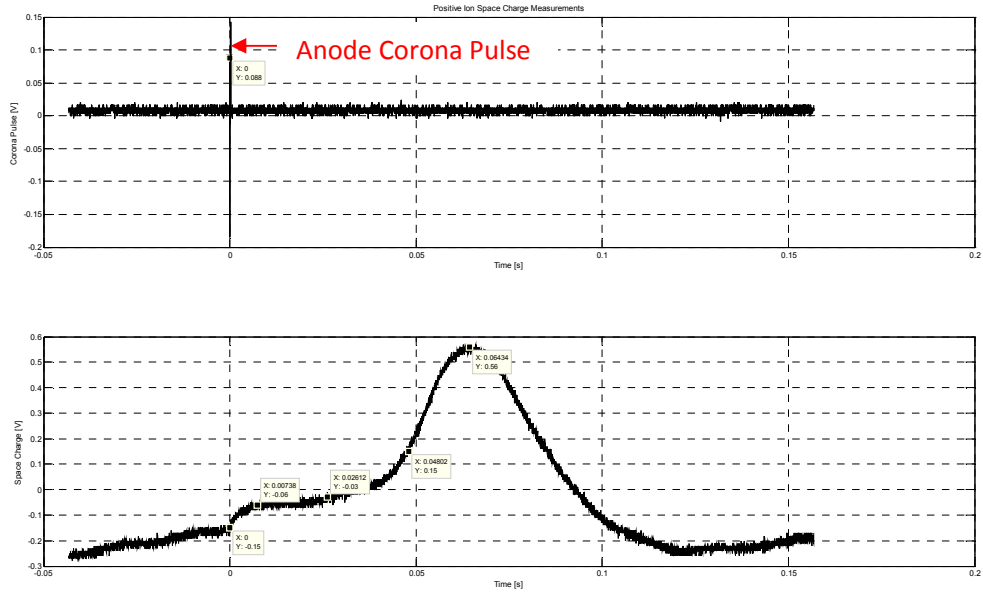
Figure 4.43: Corona pulse (top image) and electrometer output (bottom image)

4.6.6 PIC Computational Results

The particle-in-cell (PIC) computational code discussed in this chapter was used to simulate the space charge effects on a sensing electrode with high input impedance situated flush with the ground plane under a conductor. The simulation was done for similar heights above ground and conductor voltage levels as during the measurements. An example of a measured and PIC simulated output of the electrometer sensing electrodes for a positive conductor height of $h = 0.624m$ above ground is shown in figure 4.45.

An example of the space charge timings measured and predicted by the PIC code for negative ions created during cathode corona is shown in figure 4.46. By considering time snapshots of the system, the computational code provides visual confirmation of the interpretation of the timing events mentioned in section 4.6.5. These timings are discussed in detail in section 4.6.7.

Anode Corona



Cathode Corona

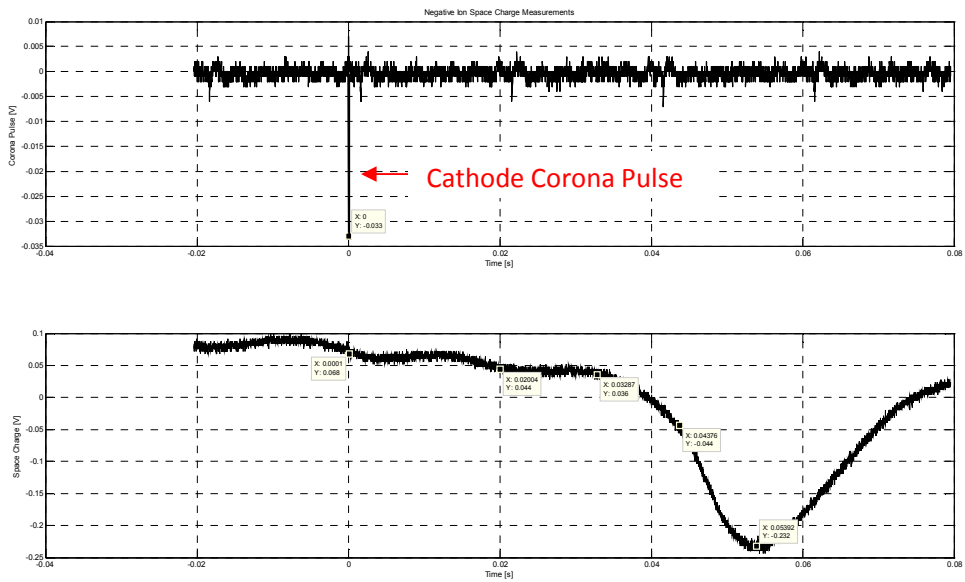


Figure 4.44: Electrometer output for anode and cathode corona at similar voltage and height

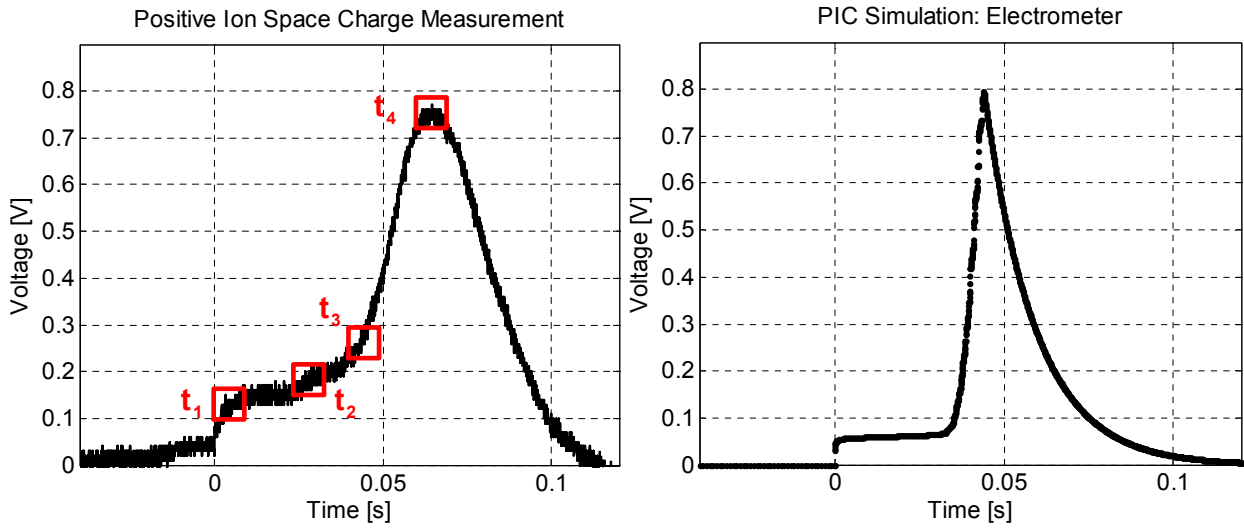


Figure 4.45: Measured and PIC simulated electrometer output

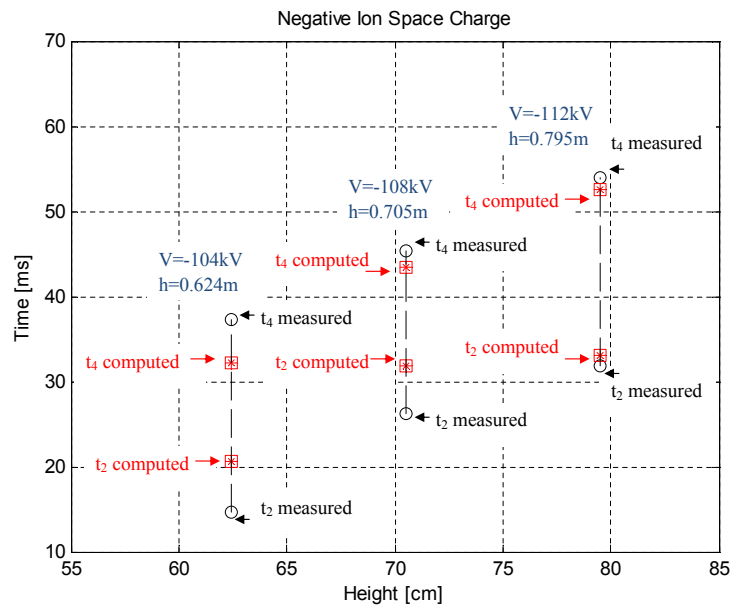


Figure 4.46: Measured and PIC simulated example for cathode corona space charge timings

4.6.7 Space Charge Timing Interpretation

4.6.7.1 Time 0 to t_1 : Space Charge Formation

The moment the corona pulse is captured on the conductor using the coupling capacitor and current transducer circuit, the electrometer sensor detects the increase in the electric field due to the formation of the ion space charge cloud. The rapid movement of the space charge in the highly divergent field close to the conductor results in a noticeable displacement current.

4.6.7.2 Time t_1 to t_2 : Space Charge Movement

The ions are moved away from the conductor by the electric field force vectors towards the ground plane and sensing plate. The displacement current that results due to the change in electric field, in this lower field region, is much less noticeable. The electrometer only experiences a slight change in electric field as the space charge moves through the gap towards the sensing electrodes.

4.6.7.3 Time t_2 to t_3 : Charge Approach and Neutralisation

The displacement current due the space charge cloud in the close vicinity of the sensing electrode now again becomes evident. The increase in the gradient of the output curve relates to the conduction current due to the space charge neutralising on the sensing electrodes.

4.6.7.4 Time $> t_4$: Circuit Discharge

At time t_4 the gradient of the output curve is zero and there is no change in the electric field at this point. It is assumed that the majority of the ions in the cloud have now either been collected by the sensing electrode and the ground plane, or have diffused and drifted away. The tail of the output curve returning to its original value is due to the $\tau = RC$ time constant of the circuit. This is an indication of how long it takes for the charge that built up on the sensing plate to leak through the capacitive resistance to ground.

Chapter 5

DC Conductor Corona Measurement Methods

In general, conductor corona test methods are used to generate experimental data to predict corona performance on transmission lines [11]. Various conductor corona test methods are used for evaluating the corona performance of conductors used on high voltage alternating current (HVAC) transmission schemes. Corona test cages, for instance, have been shown in [82], [83] and [84] to be convenient and inexpensive means of studying the AC corona performance of conductor bundles [85]. The main difference, however, between high voltage direct current (HVDC) and HVAC transmission schemes is the continuous formation and build-up of space charge due to the electrostatic field of the former. The space charge plays a critical role in the formation and suppression processes of DC corona, and it is unclear if the same conductor test methods can be used to evaluate the corona performance of HVDC conductors [2]. Utilising computational and relatively simple metrological techniques discussed in chapter 4, a better understanding of the particle dynamics of space charge created during direct current (DC) corona events was achieved. This understanding now needs to be applied to characterising the various DC conductor corona test methods considered in this dissertation. The methods that are currently available to Eskom are of particular interest. This chapter not only characterises these corona test methods, but furthermore investigates the effect of correct impedance matching on radio interference levels during wideband measurements on systems as in figure 5.7.



Figure 5.1: Corona discharges on a twin conductor bundle in the Eskom Megawatt Park large outdoor corona cage [Photo by: *C. Esterhuizen*]

5.1 Corona Test Methods

Various electrode geometries like point-to-plane, sphere-to-plane and concentric spheres have been used to study corona discharges [21]. In this dissertation, three test methods to study HVDC conductor corona beyond inception are investigated at an altitude of 1550m above sea level. These include a small corona cage, a large outdoor corona cage and a short outdoor test line. In order to assess these testing methods, the corona performance of two types of conductor was evaluated using all three systems. The results presented are for a single *Zebra* conductor with a diameter of 2.86cm, as well as a single *Kingbird* conductor with a diameter of 2.38cm.

5.1.1 Small Corona Cage

The main criterion for a laboratory cage test arrangement is to have an adequate margin between the corona inception level and breakdown. Smooth and stranded conductors can be tested in a laboratory corona cage and artificial corona source can be used to simulate surface imperfections or water drops [11]. The dimensions for the small portable corona cage at the Eskom Megawatt Park test facility are given in table 5.1 and the schematic is shown in figure 5.2. A photo of the actual corona cage is shown in figure 5.3.

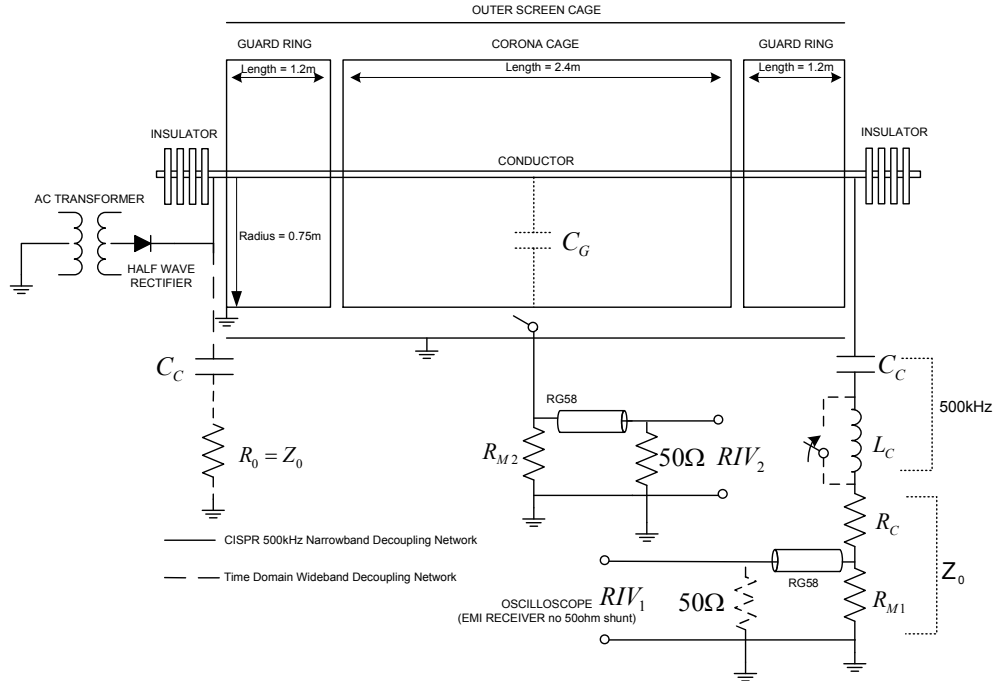


Figure 5.2: Schematic for Eskom Megawatt Park small corona cage measurement system



Figure 5.3: Eskom Megawatt Park small corona cage

Small Corona Cage			
Cage Length	Cage Diameter	# Conductors	Conductor Length
3.6m	1.5m	1	3.6m

Table 5.1: Eskom Megawatt Park small corona cage parameters

5.1.2 Short Test Line

Outdoor test lines are usually short sections of full-scale transmission lines. Since space charge fills the inter-electrode region of a DC transmission line and influences the corona performance, a single conductor can be used to study monopolar corona [11]. The line length should be sufficiently long to study fair weather corona. Cost and availability of land resulted in a short outdoor test line erected at the Eskom Megawatt Park test facility. The test line, shown in figure 5.5, has a length of 19m and a height above ground of 1.8m. The height was chosen to achieve similar surface voltage gradients as in the large cage using the single diode half wave rectified DC source that was available for testing. The required surface voltage gradients would not have been achieved with the DC voltage source if the conductor was strung any higher. The main purpose of this test arrangement is to investigate corona discharges without completely enclosing the conductor with an electrode as in a corona cage. This will be a slightly more realistic case as the space charge created during the corona events will drift or diffuse away from the conductor due to the electric field. It was found in [86] that although investigations on short samples of line conductor cannot duplicate all the actual operating conditions of a long line, they are still invaluable when studying fundamentals of corona discharges.

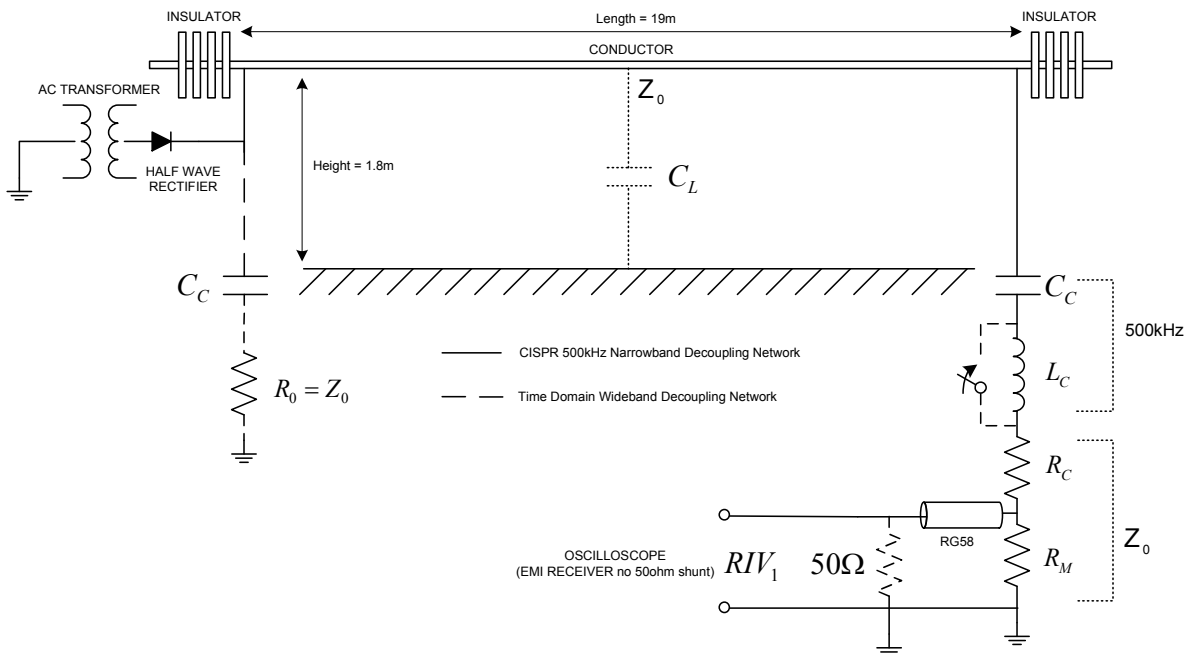


Figure 5.4: Schematic for Eskom Megawatt Park short test line measurement system

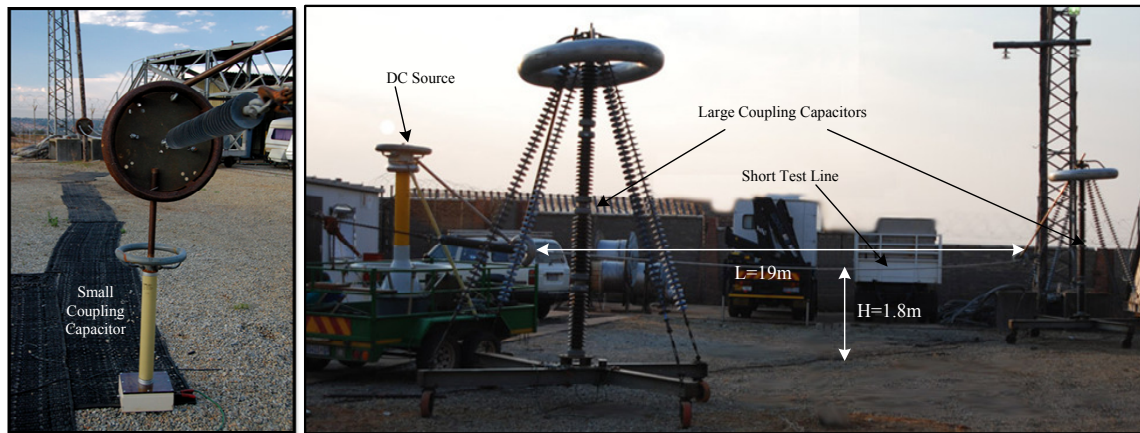


Figure 5.5: Eskom Megawatt Park short test line

Short Test Line			
Line Length	Line Height	# Conductors	Conductor Length
19m	1.8m	1 to 4	19m

Table 5.2: Eskom Megawatt Park short test line parameters

5.1.3 Large Corona Cage

To evaluate the corona performance for conductor configurations used on transmission lines, an outdoor cage with a much larger diameter and length than that of a laboratory cage can be used. Due to the sparse distribution of corona sources on transmission lines in fair weather, it is recommended in [11] and [50] that an outdoor cage of a length of at least 100m or more be used. Eskom's large outdoor corona cage at the Megawatt Park test facility, shown in figure 5.6, can take up to six conductors in a bundle and has a length and diameter of 40m and 7m respectively. A photo of the large outdoor corona cage is shown in figure 5.7.

Large Corona Cage			
Cage Length	Cage Diameter	# Conductors	Conductor Length
40m	7m	1 to 6	48m

Table 5.3: Eskom Megawatt Park large outdoor corona cage parameters

To date, radio interference (RI) performance of conductors has been evaluated on this cage using an EMI receiver and considering only the 500kHz frequency component as prescribed by [87]. This is a narrowband measurement and the coupling capacitor has a series inductor that

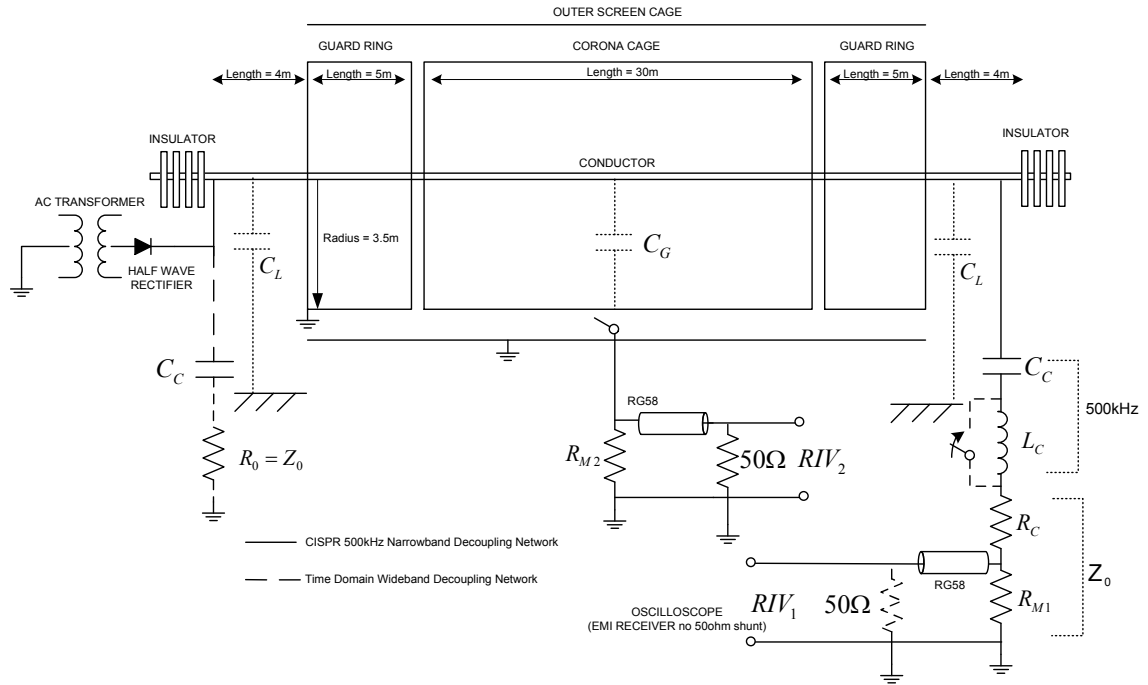


Figure 5.6: Schematic for Eskom Megawatt Park large outdoor corona cage measurement system



Figure 5.7: Eskom Megawatt Park large outdoor corona cage

forms a 500kHz bandpass filter terminating into 300Ω . The other end of the cage is left as an open circuit. A blocking filter, also tuned to 500kHz, is placed between the high voltage source and corona cage. All of this is done in accordance to the CISPR standard discussed in section 5.3.2. Wideband techniques have never been applied for excitation function derivation.

5.2 Background Radio Noise Characterisation

It is important to ensure that the measurement systems are adequately shielded against background radio noise (RN). The background RI levels were measured on the earth structures of the various test systems using a handheld *Rohde & Schwarz FSH3 Spectrum Analyser* (100kHz to 3GHz) and an *EMCO* current probe as shown in figure 5.8. The large as well as the small corona cages have an outer cage structure, slightly larger than the corona cage, that will provide some form of shielding. The *main earth* referred to in this section is the earth of the outer shielding structures, while the *inner earth* refers to the earth of the corona cages.



Figure 5.8: EMCO current probe around small corona cage main earth

5.2.1 Small Corona Cage RN Coupling

With the spectrum analyser pre-amp switched on and with an attenuation setting of 0dB, the resolution bandwidth (RBW) was dropped to 3kHz in order to lower the noise floor level. A passive frequency sweep from 0 to 30MHz was done and the RN results are shown in figure 5.9. It is evident that the corona cage might be acting as a monopole antenna with the earth

connections forming a pickup loop. The RN measurement on the inner earth is shown in figure 5.10. From these results it can be seen that the outer structure of the corona cage provides reasonable shielding to especially the lower frequency components of the various background RN sources.

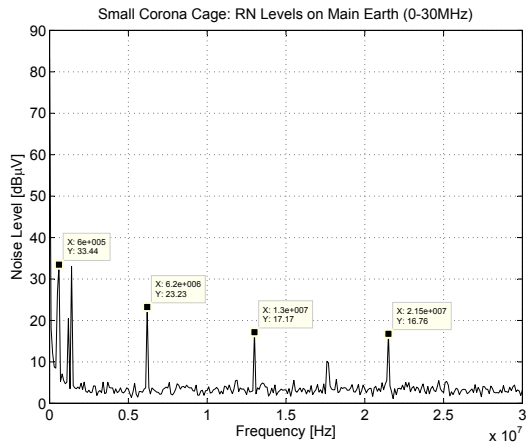


Figure 5.9: Radio noise levels measured on small corona cage main earth

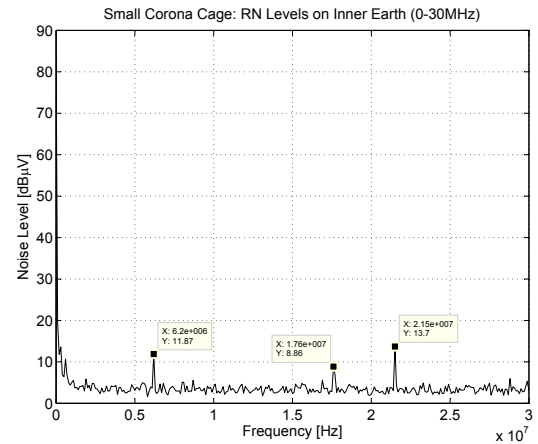


Figure 5.10: Radio noise levels measured on small corona cage inner earth

5.2.2 Large Corona Cage RN Coupling

The background RN levels on the main and inner earths of the large corona cage are shown in figures 5.11 and 5.12. The outer structure of the large corona cage provides excellent shielding against background RN coupling. It is important to note that when applying time domain reflectometry (TDR) techniques as in figure 5.13, a large percentage of a known fast rising pulse injected at the one end of the conductor was found to be reflected back as soon as it reaches the opening of the cage. This is due to the change in effective characteristic impedance experienced by the pulse at the 4m length of conductor above ground going into the 3.5m radius coaxial structure. When considering wideband measurements on this system, it is therefore important to ensure correct impedance matching at both ends to minimise reflected pulses at this point getting back onto the measurement section of the cage.

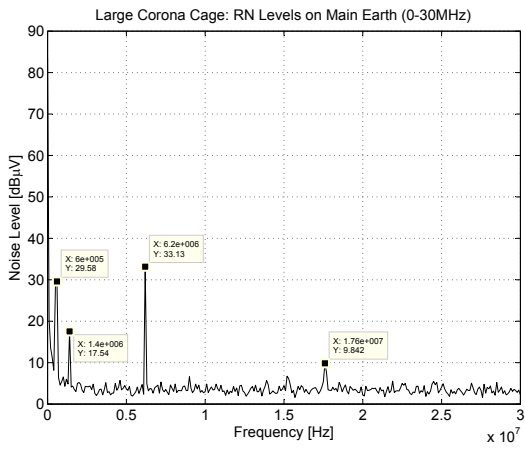


Figure 5.11: Radio noise levels in the spectrum 0 to 30MHz measured on large corona cage main earth

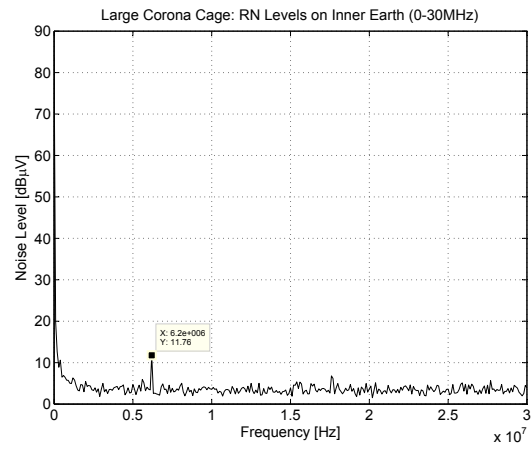


Figure 5.12: Radio noise levels in the spectrum 0 to 30MHz measured on large corona cage inner earth

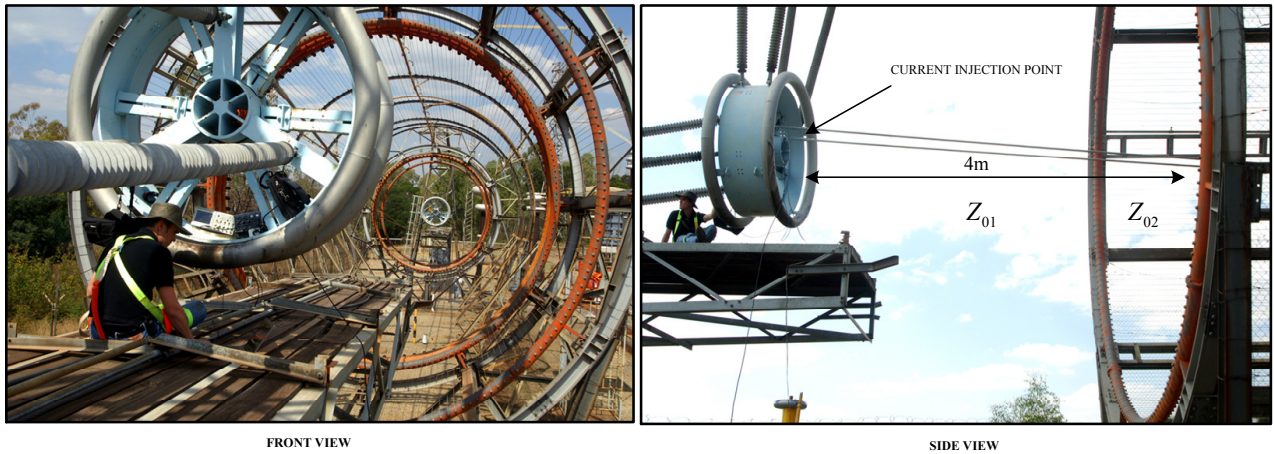


Figure 5.13: Time domain reflectometry measurements on large corona cage

5.2.3 Short Test Line RN Coupling

The background RN levels on the short test line are shown in figure 5.14. The short test line has no outer structure that can provide shielding as in the case of the corona cages. The RN measurements were done without any impedance matching terminations, and both ends of the test line were open circuit.

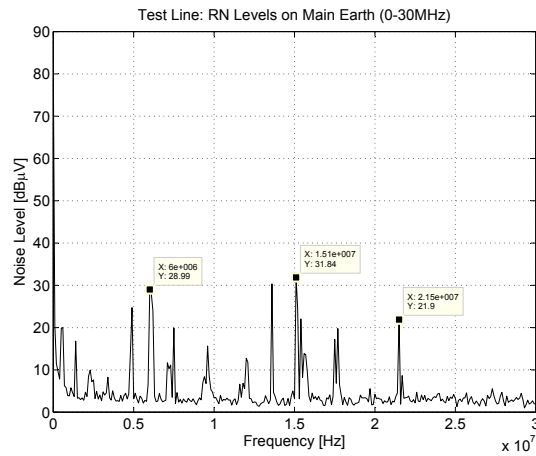


Figure 5.14: Radio noise levels in the spectrum 0 to 30MHz measured on short test line main earth

5.3 Conducted Radio Noise Measurement Circuits

Wideband time domain measurements were made on all three corona test methods discussed in section 5.1 using a *Tektronix TDS2014B* scope with 100MHz and 1GS/s bandwidth and sampling rate respectively, as well as a *National Instruments PCI-5124* data acquisition card with 150MHz bandwidth and 200MS/s sampling rate. The CISPR narrowband frequency domain measurements were made on all three corona test methods using a *Rohde & Schwarz ESCI EMI Receiver* with frequency range between 9kHz and 3GHz. The measurement circuits used to capture the corona events on the conductors are discussed in sections 5.3.1 and 5.3.2.

5.3.1 Wideband Measurement Circuit

The wideband measurements were made using two coupling capacitors in two different measurement circuits. The first measurement circuit, used on the small corona cage measurements, made use of a 500pF coupling capacitor terminated in a resistive chain equal to the characteristic impedance of the measurement system, Z_0 . The transfer function for the coupling capacitor is shown in figure 5.16, while the transfer function for the total measurement circuit terminated in Z_0 is shown in figure 5.17.

The second measurement circuit, used on the large corona cage and short test line measurements, made use of 368pF coupling capacitor and resistive chain again equal to the characteristic impedance of the measurement system, Z_0 . The transfer function for the coupling capacitor is shown in figure 5.18, while the transfer function for the total measurement circuit terminated in Z_0 is shown in figure 5.19. The schematics for the two measurement circuits coupled to a

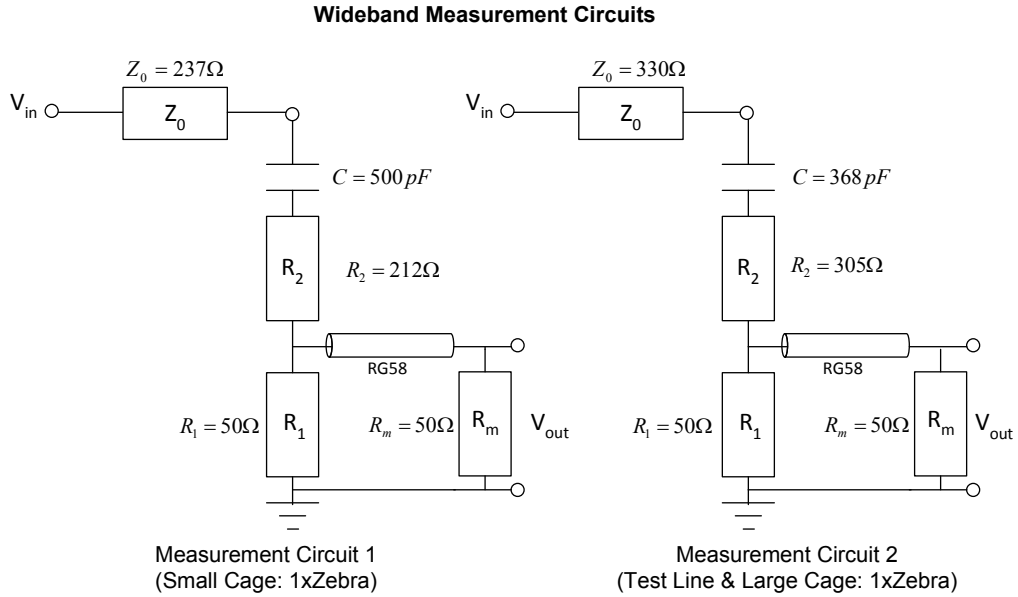


Figure 5.15: Schematics for wideband measurement circuits connected to systems with characteristic impedance Z_0

system with characteristic impedance Z_0 are shown in figure 5.15. The transfer function, $H(s)$, of the wideband measurement circuit is given by equation 5.3.1, where $s = j\omega$, $j = \sqrt{-1}$, and $\omega = 2\pi f$.

$$H(s) = \frac{sCR_m}{1 + sCR_1 + sCR_m} \tag{5.3.1}$$

5.3.2 CISPR Narrowband Measurement Circuit

The narrowband measurements were made in accordance to the *International Special Committee on Radio Interference* (CISPR) standard for corona radio interference tests of overhead powerlines and high voltage equipment [87]. The measurement circuit consists of a tuned series inductor and capacitor circuit with resonant frequency $f_0 = 500kHz$ as in figure 5.20. The transfer function, $H(s)$, of the narrowband measurement circuit is given by equation 5.3.2, where $s = j\omega$, $j = \sqrt{-1}$, and $\omega = 2\pi f$.

$$H(s) = \frac{sCR_m}{1 + s^2CL + sCR_1 + sCR_m} \tag{5.3.2}$$

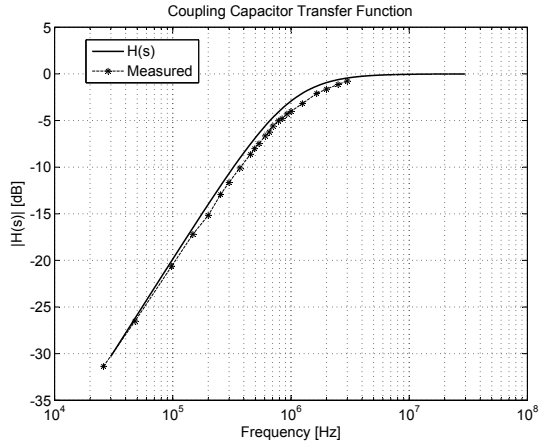


Figure 5.16: Transfer function for coupling capacitor used in small corona cage measurement circuit

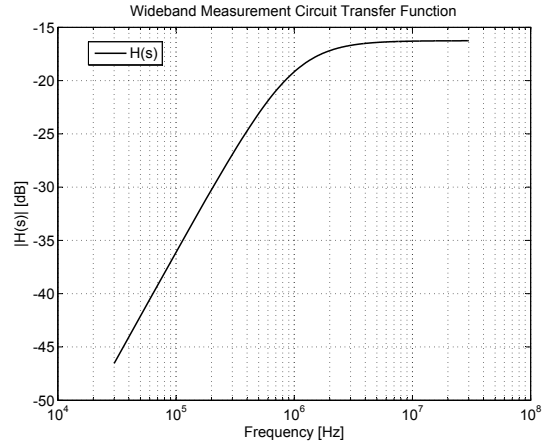


Figure 5.17: Transfer function for wideband measurement circuit used in small corona cage measurements

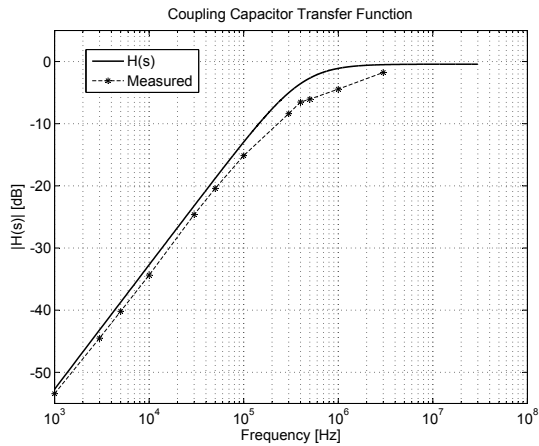


Figure 5.18: Transfer function for coupling capacitor used in large corona cage and test line measurement circuits

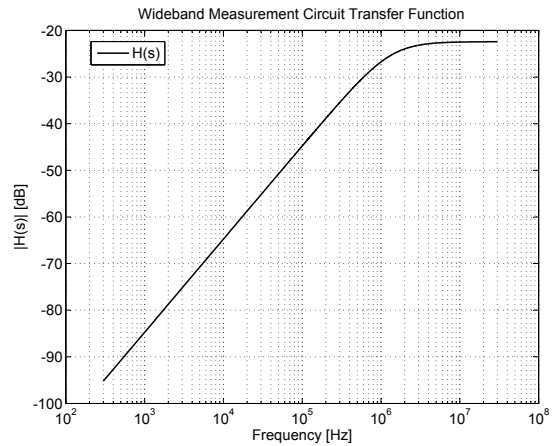


Figure 5.19: Transfer function for wideband measurement circuit used in large corona cage and test line measurements